

**Design and Numerical Simulation of an Evaporator for a Compact
Vapor Compression Refrigeration System**

by

Benjamin Culp Kendall

A thesis submitted to the Graduate Faculty of
Auburn University
in partial fulfillment of the
requirements for the Degree of
Master of Science

Auburn, Alabama
December 14, 2019

Keywords: lanced offset fins, heat transfer, refrigeration,
heat exchanger, compact, evaporator

Copyright 2019 by Benjamin Culp Kendall

Approved by

Dr. Roy W. Knight, Associate Professor of Mechanical Engineering
Dr. Sushil Bhavnani, Professor of Mechanical Engineering
Dr. Lorenzo Cremaschi, Associate Professor of Mechanical Engineering
Dr. W. Joel D. Johnson, Senior RF Systems Engineer, L3Harris Technologies

Abstract

A miniature plate-fin heat exchanger was designed for use in a compact Vapor Compression Refrigeration (VCR) system used for cooling electronic components in an Air Transportable Rack (ATR) chassis. The evaporator was designed to have a cooling capacity of 350 W and to use R236ea as the primary refrigerant and PAO as the secondary refrigerant. The final dimensions of the heat exchanger were 2.75 x 0.75 x 2.00 inches. A model of the evaporator was developed and incorporated into a full cycle analysis of the refrigeration system. Comparisons between existing experimental correlations and a numerical simulation of PAO flow through lanced offset strip fins was also completed. Thermal performance of lanced offset strip fins showed agreement between the two methods to within eight percent while the pressure drop behavior only had 50 percent agreement when comparing existing experimental correlations and numerical simulations. Local fin heat transfer analysis revealed that thermally fully developed conditions prevailed on the last half of each fin resulting in constant Nusselt numbers for the designed fin geometry and flow conditions.

Acknowledgements

Thanks to the members of my advisory committee, Dr. Roy W. Knight, Dr. Sushil H. Bhavnani, and Dr. Lorenzo Z. Cremaschi, with special thanks to Dr. Knight for his patience, oversight, and guidance throughout the study.

Thanks to Dr. Joel Johnson and Don George for sharing their extensive knowledge of industry and constant support.

Table of Contents

Acknowledgements.....	iii
List of Figures.....	vi
List of Tables.....	xii
Nomenclature.....	xiii
Chapter 1: Introduction.....	1
1.1 Electronics Thermal Management.....	1
1.2 Literature Review.....	2
1.3 Vapor Compression Refrigeration Systems.....	4
1.4 Heat Exchangers.....	7
1.5 Objective of Current Study.....	7
Chapter 2: Evaporator Design.....	10
2.1 Heat Exchanger and Fin Comparison.....	10
2.2 Pressure Drop Analysis.....	14
2.2.1 Single-phase Pressure Drop in Lanced Offset Strip Fins.....	14
2.2.2 Two-phase Pressure Drop in Lanced Offset Strip Fins.....	18
2.3 Heat Transfer Analysis.....	21

2.3.1	Single-phase Heat Transfer for Lanced Offset Strip Fins.....	21
2.3.2	Two-phase Heat Transfer for Lanced Offset Strip Fins.....	23
2.4	Final Fin selection for Evaporator.....	26
2.5	Header Flow Distribution.....	27
Chapter 3: Full Cycle Analysis for the Vapor Compression Refrigeration System		32
Chapter 4: Numerical Simulation Setup.....		37
4.1	Geometry	37
4.2	Mesh.....	38
4.3	Fluent.....	39
4.4	Grid Independence	41
Chapter 5: Results.....		43
5.1	Fin Height.....	43
5.2	Fin Thickness	47
5.3	Local Heat Transfer Coefficients	52
5.4	Velocity Fields and Flow Behavior.....	61
Chapter 6: Conclusions.....		63
Chapter 7: References.....		65
Appendix A: Experimental setup and instrumentation for testing VCR system with custom evaporator.		68
Appendix B: Simulation setup procedure using ANSYS Fluent.....		72

List of Figures

Figure 1.1: Schematic refrigeration system within an ATR chassis with Polyalphaolefin flowing through the ATR chassis walls.	3
Figure 1.2: Schematic of a vapor compression refrigeration system.....	5
Figure 1.3: T-s diagram for a vapor compression refrigeration cycle.	6
Figure 1.4: Air cooled condenser used in HVAC system (left), air cooled condenser from Kewley Refrigeration (middle), air cooled car radiator (right).	7
Figure 1.5: CAD model of plate-fin heat exchanger core (left), brazed plate heat exchanger (middle), and cold plate heat exchanger (right).	8
Figure 1.6: Refrigeration system component layout within the ATR chassis (tan enclosure).	9
Figure 2.1: Plate-fin surfaces compared by Dewatwal [6]: (a) plain rectangular, (b) plain trapezoidal, (c) wavy, (d) lanced offset strip fin, (e) louvered, and (f) perforated.	11
Figure 2.2: Three common geometric variations of plate-fin channel cross section as discussed by Huzayyin et al. [7]. Rectangular (left), trapezoidal (middle), and triangular (right). ..	12
Figure 2.3: Two thermal boundary conditions within the plate-fin heat exchanger core for both uniform wall temperature (T) and uniform heat flux (H1) as studied by Huzayyin et al. [7].	12
Figure 2.4: Huzayyin et al.'s [7] Nusselt numbers for fully developed laminar flow through trapezoidal channel cross section in a plate-fin core with uniform wall temperature, T (right), and uniform heat flux, H1 (left).	13

Figure 2.5: Manglik and Bergles [10] geometric parameters for lanced offset strip fins.	14
Figure 2.6: Pressure drop as a function of fin height, b , and thickness, t , for PAO flowing through offset strip fins.	17
Figure 2.7: Pressure drop as a function of fin length, l , and fin spacing, c , for PAO flowing through offset strip fins.	17
Figure 2.8: Two-phase pressure drop for R236ea flowing through offset strip fins as a function of (a) fin height, (b) fin length, (c) fin thickness, and (d) fin pitch.	20
Figure 2.9: Heat transfer coefficient as a function of fin height and thickness for PAO flowing through offset strip fins.	22
Figure 2.10: Heat transfer coefficient as a function of fin length and fin spacing for PAO flowing through offset strip fins.	22
Figure 2.11: Two-phase heat transfer coefficient for R236ea flowing through offset strip fins as a function of (a) fin height, (b) fin length, (c) fin thickness, and (d) fin pitch.	25
Figure 2.12: I-type header design (left) and C-type header design (right).	27
Figure 2.13: Six evaporator header configurations analyzed using Flotherm.	28
Figure 2.14: Velocity range across fin channels vs. element count for I-type rectangular header.	29
Figure 2.15: Individual channel velocities for I-type header with first baffle design (left), second baffle iteration (middle), and final baffle design (right).	29
Figure 2.16: Velocity profiles for PAO flowing through an I-type trapezoidal header with baffle (top) and C-type trapezoidal header with baffle (bottom) modelled using Flotherm.	30
Figure 3.1: Temperature vs. entropy plot for vapor compression refrigeration cycle operating at various ambient temperatures.	33

Figure 3.2: Pressure vs. enthalpy plot for vapor compression refrigeration cycle operating at various ambient temperatures.	33
Figure 4.1: 3D model of lanced offset strip fin section analyzed in Fluent.....	37
Figure 4.2: 3D model of fluid region within lanced offset strip fin core.....	38
Figure 4.3: Meshed model of the 14-row lanced offset strip fins section.....	39
Figure 4.4: Temperature and pressure results for grid independence study on lanced offset strip fins.....	42
Figure 5.1: Lanced offset strip fin geometry and dimensionless temperature and pressure parameters for the fin height study.	44
Figure 5.2: PAO temperature drop across evaporator for three fin heights as predicted by experimental correlations from Manglik and Bergles [10] and Ansys Fluent.....	44
Figure 5.3: Percent difference between Manglik and Bergles [10] and Fluent’s predicted temperature drop within evaporator for various lanced offset strip fin heights.....	45
Figure 5.4: PAO pressure drop across evaporator for three fin heights as predicted by experimental correlations from Manglik and Bergles [10] and Ansys Fluent.....	46
Figure 5.5: Percent difference between Manglik and Bergles [10] and Fluent’s predicted pressure drop within evaporator for various lanced offset strip fin heights.....	46
Figure 5.6: Lanced offset strip fin geometry and dimensionless temperature and pressure parameters for the fin thickness study.	47
Figure 5.7: PAO temperature drop across evaporator for three fin thicknesses as predicted by experimental correlations from Manglik and Bergles[10] and Ansys Fluent.....	48
Figure 5.8: Percent difference between Manglik and Bergles [10] and Fluent’s predicted temperature drop within evaporator for various lanced offset strip fin thicknesses.	49

Figure 5.9: PAO pressure drop across evaporator for three fin thicknesses as predicted by experimental correlations from Manglik and Bergles [10] and Ansys Fluent..... 50

Figure 5.10: Percent difference between Manglik and Bergles [10] and Fluent’s predicted pressure drop within evaporator for various lanced offset strip fin thicknesses..... 50

Figure 5.11: Locations where local heat transfer coefficients were calculated. 52

Figure 5.12: Nusselt numbers as a function of inverse Graetz number for three PAO inlet velocities compared to Nusselt number for isothermal rectangular tube with same aspect ratio presented by Incropera [22]. 53

Figure 5.13: Nusselt numbers as a function of inverse Graetz number for three fin heights and a Reynolds number of 14.67 compared to Nusselt number for isothermal rectangular tube with aspect ratio of 2.5 presented by Incropera [22]. 54

Figure 5.14: Nusselt numbers as a function of inverse Graetz number for three fin thicknesses and an inlet velocity of 0.1691 m/s compared to Nusselt number for isothermal rectangular tube with aspect ratio of 2.5 presented by Incropera [22]..... 55

Figure 5.15: Fin wall locations evaluated with position a at the leading edge and position e at the trailing edge for fin 1 wall heat flux (top) and fin 1 wall temperature (bottom). 56

Figure 5.0.16: Fin 1 Nusselt numbers as a function of inverse Graetz number for three different PAO inlet velocities compared to Nusselt number for isothermal rectangular tube with aspect ratio of 2.5 presented by Incropera [22]..... 57

Figure 5.17: Comparison between Nusselt numbers found using Fluent for the lanced offset strip fins and solution for constant wall temperature circular duct discussed by Incropera [21]. 58

Figure 5.18: Nusselt numbers as a function of inverse Graetz number for the first and thirteenth fin rows for the baseline fin geometry and flow conditions.	59
Figure 5.19: Fin 1 Nusselt numbers as a function of inverse Graetz number for three different fin heights and an inlet velocity of 0.1691 m/s compared to Nusselt number for isothermal rectangular tube with aspect ratio of 2.5 presented by Incropera [22]......	60
Figure 5.20: Fin 1 Nusselt numbers as a function of inverse Graetz number for three different fin thicknesses and an inlet velocity of 0.1691 m/s compared to Nusselt number for isothermal rectangular tube with aspect ratio of 2.5 presented by Incropera [22]......	60
Figure 5.21: Vector velocity plots of the PAO flowing through baseline geometry lanced offset strip fins at $Re = 14.67$	62
Figure A.1: Liquid Chiller Module produced by Aspen Systems.	68
Figure A.2: Aspen LCM with new evaporator, flow meter, and wooden test fixtures.	69
Figure A.3: Experimental schematic for the VCR system including instrumentation.	70
Figure A.4: RTD probe inserted into refrigeration line via T-junction.	71
Figure B.1: Lanced offset strip fin model in Design Modeler with named surfaces.	72
Figure B.2: Face Sizing mesh feature used on lanced offset strip fin model.	73
Figure B.3: Inflation mesh feature used on lanced offset strip fin model.	73
Figure B.4: General mesh details used on lanced offset strip fin model.	74
Figure B.5: Final mesh rendering with applied Face Sizing and Inflation mesh refinements.	74
Figure B.6: Manually entering PAO fluid properties into Fluent.	75
Figure B.7: Manually creating periodic boundary conditions for the lanced offset strip fin model.	76

Figure B.8: Applying constant temperature boundary condition to top and bottom surfaces of the
lanced offset strip fin model. 76

List of Tables

Table 2.1: Heat exchanger geometry and operating conditions used for fin sensitivity analysis..	16
Table 2.2: Final fin geometry selection for evaporator.....	27
Table 2.3: Results from header simulation analysis.	31
Table 4.1: Polyalphaolefin properties.	40
Table 5.1: Fin geometries analyzed with Ansys Fluent.....	43
Table 5.2: Baseline fin geometry pressure drops for a range of Reynolds numbers.....	50

Nomenclature

Acronyms

ATR	Air Transportable Rack
CFD	Computational Fluid Dynamics
COP	Coefficient of Performance
LMTD	Log Mean Temperature Difference
PAO	Polyalphaolefin
TEC	Thermoelectric Cooler
VCR	Vapor Compression Refrigeration

English Letter Symbols

A	Surface area
A_c	Cross-sectional area
b	Fin height
Bl	Boiling number
Bo	Bond number
c	Fin spacing
d	Hydraulic diameter
c_p	Specific heat
f	Fanning friction factor

F	Reynolds number factor
g	Gravitational constant
\dot{G}	Mass flux
Gz	Graetz number
h	Heat transfer coefficient
k	Thermal conductivity
L	Length
l	Fin length
\dot{m}	Mass flow rate
M	Molecular weight
Nu	Nusselt number
P	Pressure
P*	Non-dimensional pressure drop
Pr	Prandtl number
Re	Reynolds number
S	Suppression factor
t	Fin thickness
T	Temperature
T*	Non-dimensional temperature change
x	Quality
X	Martinelli parameter
z	Axial coordinate for fin section

Greek symbols

α	Void fraction
$\bar{\alpha}$	Dimensionless fin parameter based on spacing and height
$\bar{\gamma}$	Dimensionless fin parameter based on thickness and spacing
$\bar{\delta}$	Dimensionless fin parameter based on thickness and length
μ	Dynamic viscosity
ν	Specific volume
ρ	Density
σ	Surface tension
ϕ	Fin angle
ϕ_f^2	Two-phase frictional multiplier

Subscripts

c	critical
f	fluid
l	liquid
nb	nucleate boiling
pb	pool boiling
v	vapor

Chapter 1: Introduction

1.1 Electronics Thermal Management

Increased transistor counts and compact packaging of electronics has led to the need for more robust thermal management techniques. Air cooling, which has long been the industry standard for most applications, is no longer capable of managing the increased thermal loads of many modern electronics. This is particularly true for electronics used in high-temperature environments such as Air Transportable Racks (ATRs) which house electronic cards that provide many military vehicles with a variety of services. These ATRs and the cards they contain, when used in hot environments, are no longer being effectively cooled by their standard fans. Currently no active cooling method which effectively manages the thermal loads of the electronics in an ATR has been found in literature. A variety of solutions to electronics thermal management have been explored as electronics continue to become denser, including passive cooling methods such as heat pipes, liquid immersion and active cooling methods such as jet impingement, thermoelectrics, and refrigeration. Each of these cooling methods has their own advantages but refrigeration lends itself particularly well to cooling ATRs when compared to other systems since refrigeration systems can operate in high temperature ambients and are very efficient [1].

Thermoelectric coolers, which are extremely compact and have very simple construction, have been found to have low efficiencies and low cooling capacities and therefore are not well suited to cooling ATRs. Jet impingement, which uses high velocity single-phase fluid to cool surfaces, does not lend itself to cooling ATRs either despite being capable of removing much higher heat loads than thermoelectric coolers. This is because jet impingement requires

manifolds and other components which are difficult to integrate into the ATR due to limited space and the existing design of the ATR frame.

While refrigeration systems are more complex, they have the benefit of highly efficient two-phase heat transfer and of being able to operate in high ambient temperatures. Heat exchangers used within Vapor Compression Refrigeration (VCR) systems can be designed to accommodate a variety of applications which allows VCR to be an attractive option for cooling cards in ATRs. Since ATRs are frequently stacked closely together, designing an external refrigeration system to cool them has limited applications. A more versatile solution is to develop a compact refrigeration system (patent pending) which can be inserted inside the ATR in a space created by removing a couple of cards. A coolant can then be routed through the walls of the ATR chassis and into an evaporator. The power dispersed by the electronic modules will conduct from the cards through the walls of the ATR chassis which hold them in place and into the coolant which is flowing through the rack. The warm coolant can then be routed out of the chassis walls and into the evaporator of a VCR system. The VCR system will cool the coolant before it travels back through the ATR chassis walls to absorb more heat from the cards. A simple schematic of a refrigeration system inside of an ATR chassis illustrating the process discussed above is shown below.

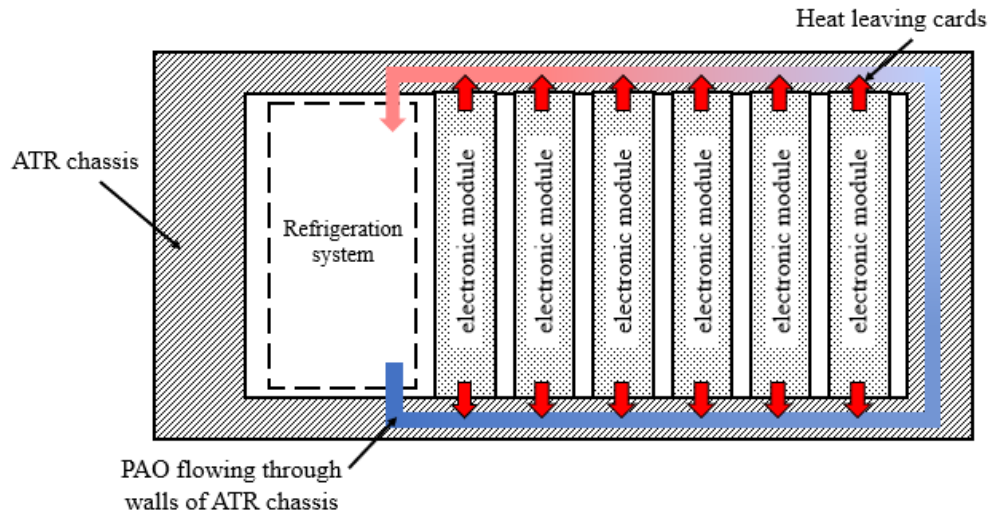


Figure 1.1: Schematic refrigeration system within an ATR chassis with Polyalphaolefin flowing through the ATR chassis walls.

Polyalphaolefin (PAO) is the dielectric oil most commonly used as a coolant for electronic components in the military and will be used for this project.

1.2 Literature Review

In the year 2000 Phelan [2] discussed current and future refrigeration technologies for cooling microelectronics, concluding that refrigeration may be the only means to cool high-performance electronic chips in the future because of the difficulty of maintaining high junction temperatures. Phelan stated the potential advantages of refrigeration as a) being able to dissipate heat while maintaining low junction temperatures, b) improve performance because of the reduced temperatures, c) increase device lifetime because of the lower operating temperatures, and d) increase device lifetime because of a constant operating temperature. The disadvantages Phelan identifies are the complexity and cost of refrigeration systems and the possible decrease in reliability. Despite these potential disadvantages, Phelan concluded that refrigeration systems were better than thermoelectric coolers (TEC), which were the only commercially available miniature cooling systems, because TECs were too limited in their cooling capacity and had low efficiencies.

Wu and Du [3] designed and tested a miniature VCR system specifically for electronics cooling with a capacity of 200 W and system dimensions of 300 x 230 x 70 mm³. They chose VCR due to its high efficiency and ability to maintain low temperatures for extended periods. Their requirements for electronics cooling VCR systems were a small capacity of 500 W or less and a compact size, ideally small enough to fit within a PC computer case. Wu and Du [3] chose to develop a refrigeration because they found passive cooling methods, which are widely used today, to be primarily designed for quickly dissipating or moving heat from a source to another location, and therefore had limited cooling capabilities.

Ashraf *et al.* [4] chose to develop a miniaturized refrigerator mainly because they claimed that miniaturization makes newer engineering systems, such as cooling methods which are integrated into electronic module substrates, possible, and because a more compact size was more widely usable. A VCR system smaller than commercial systems but larger than the most compact, miniature systems was designed and analyzed with the design specifications of a fixed evaporator fluid temperature of 12 °C, and ambient temperature of 45 °C, and a cooling load of 32 W. The refrigerant used in the project was R134a which was selected because of its prevalence and low environmental impact. Cooling was provided through channels formed in silicon wafers using microelectronics fabrication techniques.

Trutassanawin *et al.* 2006 [1] developed a miniature-scale refrigeration system suitable for electronics cooling which utilized microchannel heat exchangers and a commercially available compact rotary compressor. Their VCR system, which used R-134a as the primary refrigerant, provided a maximum cooling capacity of 268 W with a COP ranging from 2.8 to 4.7. While the system was able to dissipate enough heat to maintain chip temperatures below 85 °C, compressor reliability was an issue. Trutassanawin *et al.* concluded, after reviewing available

literature, that miniature-scale refrigeration systems for electronics cooling had not been widely studied and that more information on individual components as well as experimental analysis was needed.

A comprehensive review of VCR systems and their components was done in 2012 by Barbosa Jr. *et al* [5]. It was determined that mechanical vapor compression refrigeration seemed to be a viable technology for electronics cooling but that more reliable small-scale compressors were needed, as well as more experimental data on compact heat exchangers.

1.3 Vapor Compression Refrigeration Systems

VCR systems are comprised of four main components, the compressor, evaporator, condenser, and expansion valve. A schematic of a basic VCR loop is shown below in Figure 1.2.

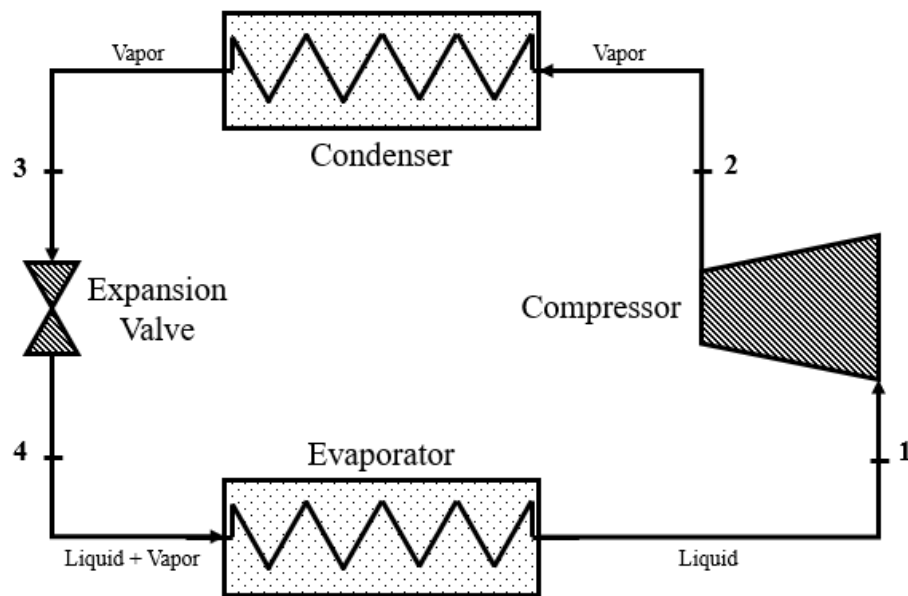


Figure 1.2: Schematic of a vapor compression refrigeration system.

The heart of a vapor compression refrigeration system is the compressor which takes cool vapor at state point 1 and compresses it to a high pressure, high temperature vapor at state point 2. This hot vapor then travels through a condenser heat exchanger where the hot vaporized refrigerant condenses into a warm liquid via heat transfer to the surrounding environment. Typically, this is

achieved by blowing cooler air over a series of pipes and fins through which the hot refrigerant flows. Once the fluid travels through the condenser it and exits at state point three and then passes through an expansion or throttle valve. Throttle valves isenthalpically drop the pressure of the refrigerant significantly which leads to a large temperature drop. Often the pressure drop that the refrigerant experiences after the throttling device results in a two-phase mixture where some of the refrigerant is vapor, and some is liquid. This cold, two-phase refrigerant is then passed through another heat exchanger, called the evaporator, where energy from a heat source is absorbed by the refrigerant, resulting in the vapor at state point one which enters the compressor. This cycle is shown in Figure 1.3 which plots temperature on the vertical axis and specific entropy on the horizontal axis.

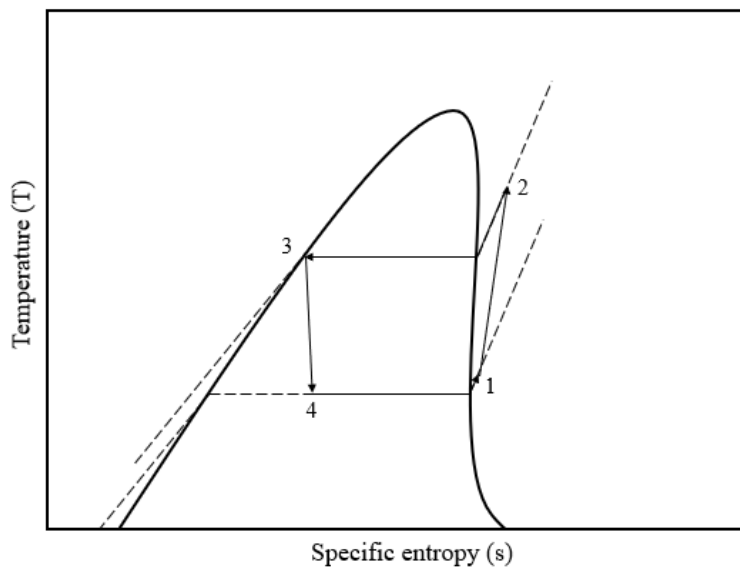


Figure 1.3: T-s diagram for a vapor compression refrigeration cycle.

The temperature increase during the compression process from point one to point two, and the temperature drop as the refrigerant passes through the throttling valve from point three to point four, are significantly larger than the temperature gradients across the condenser and evaporator.

Note that the highest temperature for the entire cycle occurs right after the compression process at state point two.

1.4 Heat Exchangers

A basic VCR system has two heat exchangers; an evaporator which facilitates energy transfer from a source to the refrigerant, and a condenser which facilitates energy transfer from the hot refrigerant to a cooler ambient environment. Many heat exchanger concepts exist such as a fin and tube heat exchanger, plate-fin heat exchangers, and brazed plate heat exchangers. Fin and tube heat exchangers are widely used in industry as condensers to reject heat from the refrigerant to surrounding air via forced convection. Figure 1.4 shows three examples of air-cooled condensers which use the fin and tube design. Each condenser below has refrigerant running through a series of horizontal pipes which are surrounded by thin fins that enhance heat transfer to the air by increasing total surface area.

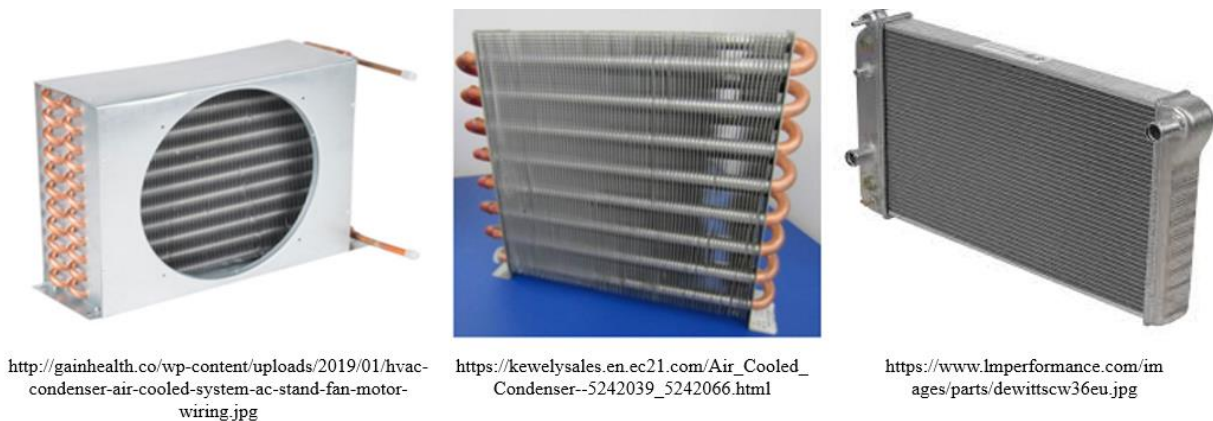


Figure 1.4: Air cooled condenser used in HVAC system (left), air cooled condenser from Kewley Refrigeration (middle), air cooled car radiator (right).

Plate-fin, brazed plate, and cold-plate heat exchangers are most commonly used as evaporators. Plate-fin heat exchangers are similar to the fin and tube heat exchangers previously discussed. Instead of one refrigerant flowing through tubes with air flowing across the finned surfaces, two different refrigerants flow between horizontal plates which have fins between

them. By having both refrigerants flowing through fins instead of one flowing through circular pipes and one flowing across fins, the surface area for heat transfer is increased significantly. The primary and secondary refrigerants can be designed to flow in the same direction, opposite directions, and in a crossflow configuration. The fins which are between the plates can also be varied to best fit a given application. Brazed plate heat exchangers are like plate-fin heat exchangers but use a series of stacked plates with baffles that are brazed together into a single unit instead of individual plates separated by fins. Cold-plate heat exchangers do not require two separate refrigerants. Instead, the primary refrigerant flows through channels created in a block of metal which contacts the heat source directly. Refrigerant flows through the pipes and absorbs heat from the block of metal which contacts a heat source. Figure 1.5 provides an example of a plate-fin, brazed plate, and cold-plate heat exchanger.



Figure 1.5: CAD model of plate-fin heat exchanger core (left), brazed plate heat exchanger (middle), and cold plate heat exchanger (right).

1.5 Objective of Current Study

The objective of this project is to design a compact evaporator heat exchanger to use in a miniature vapor compression refrigeration system to cool modules in a 3U ATR. The VCR system's compressor, evaporator, expansion device, accumulator, and control board must fit within a volume of 15.75 cm. (6.2 in.) x 5.08 cm. (2.0 in.) x 8.13 cm. (3.2 in.) created by

removing two 3U modules from the chassis. The condenser and fan will be located outside the ATR chassis and must fit within a volume of 983.2 cm³ (60 in³). A maximum of 360 W is available to power the electronics and the system must provide a cooling capacity of 350 W while operating in a 55 °C environment. To cool the electronic modules in the ATR, Polyalphaolefin (PAO) is to be routed throughout the rack and run through the evaporator as a secondary refrigerant. PAO is to be used since it is an approved military standard dielectric fluid which will not short-circuit electronics on contact. The VCR system must cool the PAO from 50 °C to 35 °C. Figure 1.6 shows a schematic of the refrigeration system components located within a section of the ATR chassis.

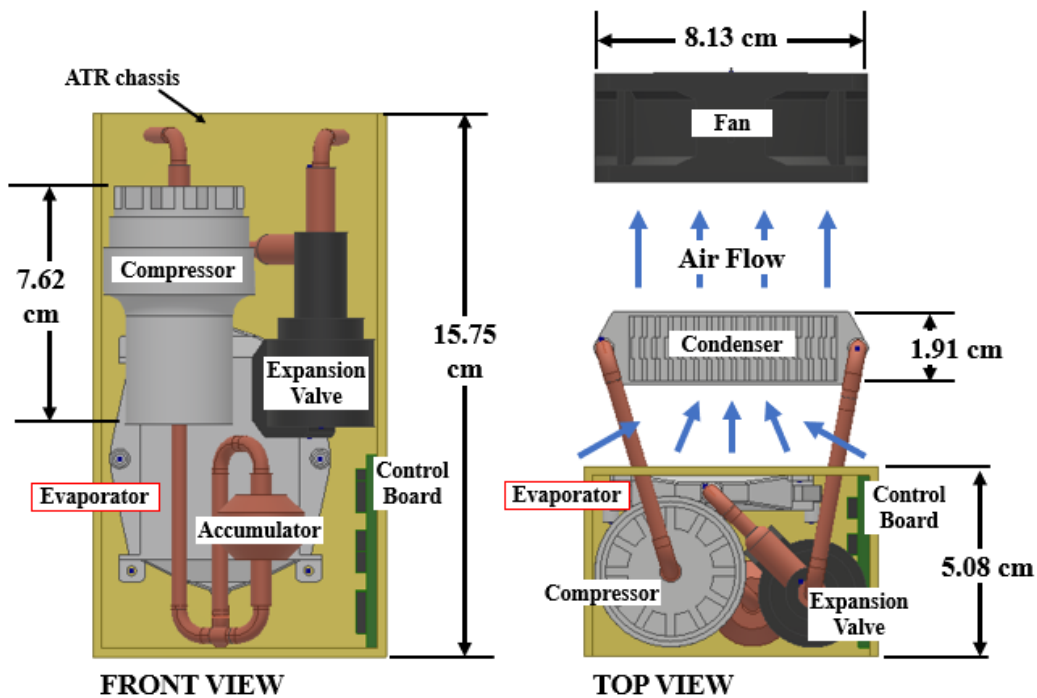


Figure 1.6: Refrigeration system component layout within the ATR chassis (tan enclosure).

Chapter 2: Evaporator Design

2.1 Heat Exchanger and Fin Comparison

Due to the requirement of using PAO as a secondary refrigerant, only liquid-to-liquid heat exchanger designs were considered. Concepts such as the shell and tube heat exchanger which are frequently used in large scale industrial applications were not pursued due low surface area for a given volume. Both the brazed plate and plate-fin designs can have large surface areas for low volumes and have been successfully used for compact applications. These two designs were considered for this project. Due to the flexibility and ease of integrating a variety of different fins into the design, the plate-fin concept was chosen over the brazed plate concept.

Fin selection was a critical step since achieving high surface area and heat transfer coefficients was essential to creating a compact heat exchanger. Dewatwal [6] discussed the performance advantages of several fin designs in his work on compact plate-fin heat exchangers including wavy, lanced offset, and louvered fins. Figure 2.1 shows the types of fin geometries Dewatwal [6] compared. Note that “lanced” simply refers to the manufacturing process used to produce the offset strip fins shown in image (d) below.

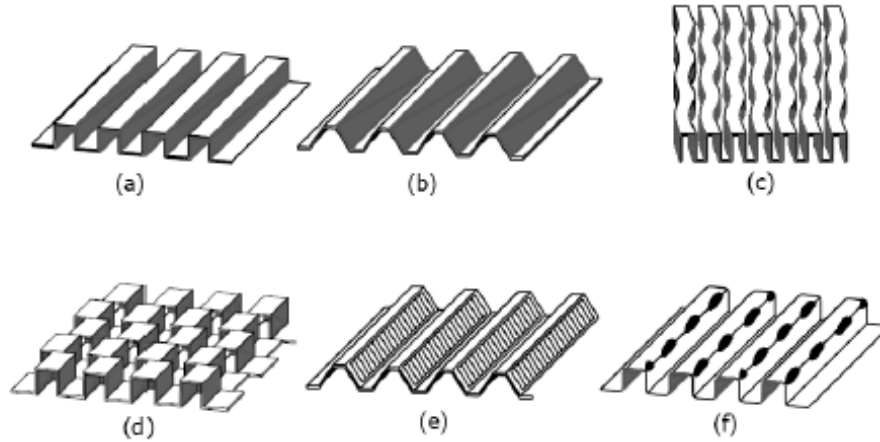


Figure 2.1: Plate-fin surfaces compared by Dewatwal [6]: (a) plain rectangular, (b) plain trapezoidal, (c) wavy, (d) lanced offset strip fin, (e) louvered, and (f) perforated.

Dewatwal [6] noted that rectangular and triangular fins have the lowest pressure drop of all the fins considered but they also have the lowest surface area and that wavy and louver fins enhance heat transfer by redirecting flow and creating a longer flow path which increases available surface area. Wavy and louver fins also result in noticeably smaller pressure drops compared to lanced offset strip fins which interrupt the fluid flow instead of redirecting it which is also discussed by Dewatwal [6].

Dewatwal [6] notes that lanced offset strip fins are extremely common in high performance plate-fin heat exchangers and achieve enhanced heat transfer by preventing continuous growth of the thermal boundary layer and by the oscillations in the flow due to vortices shed from the trailing edge of the fins. While lanced offset strip fins do enhance heat transfer, Dewatwal [6] notes that they also result in significantly increased pressure drop. While other fins such as louvered fins and wavy fins have less pressure drop than lanced offset strip fins, they also yield lower heat transfer performance. Because of the low Reynolds number flow expected for this project, more emphasis was put on having high heat transfer performance rather than lower pressure drops across the heat exchanger.

Huzayyin, Manglik, and Jog [7] analyzed fully developed laminar flow heat transfer in a plate-fin heat exchanger with trapezoidal cross section channels and the two limiting rectangular and triangular limits. Both constant wall temperature and constant heat flux boundary conditions were considered as well as variations in fin angle and spacing. Friction factors and Nusselt numbers for the different fin geometries were computed and compared. Figure 2.2 below shows the example of geometrical variations of plate-fin channel cross section analyzed by Huzayyin, Manglik, and Jog [7].



Figure 2.2: Three common geometric variations of plate-fin channel cross section as discussed by Huzayyin et al. [7]. Rectangular (left), trapezoidal (middle), and triangular (right).

Both an adiabatic fin sidewall condition as well as a heated/cooled fin sidewall condition were considered in the study. This was denoted with the parameter η , which was equal to one if the sidewalls were conducting heat, and which was equal to zero if the sidewalls were adiabatic as shown in Figure 2.3 below.

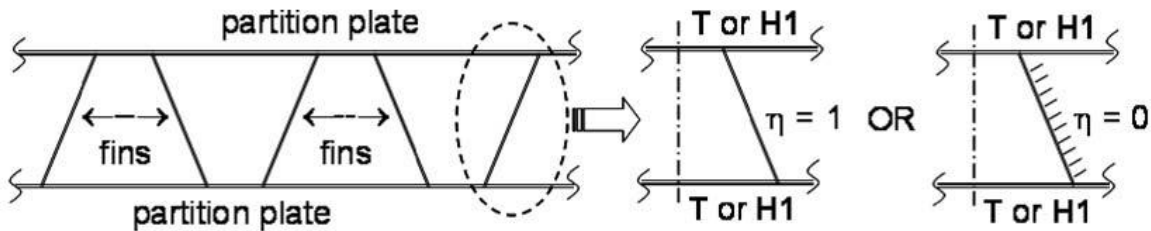


Figure 2.3: Two thermal boundary conditions within the plate-fin heat exchanger core for both uniform wall temperature (T) and uniform heat flux (H1) as studied by Huzayyin et al. [7].

Computational solutions done by Huzayyin et al. [7] were compared to studies done by Shah and London [8] and Sadasivam et al. [9] with a difference of less than plus or minus 0.5%. Huzayyin, Manglik, and Jog's Nusselt number calculations for various interfin channel geometries at uniform heat flux and at uniform wall temperature are shown in Figure 2.4 with Nusselt numbers plotted on the vertical axis and cross-sectional aspect ratio, γ , on the horizontal axis.

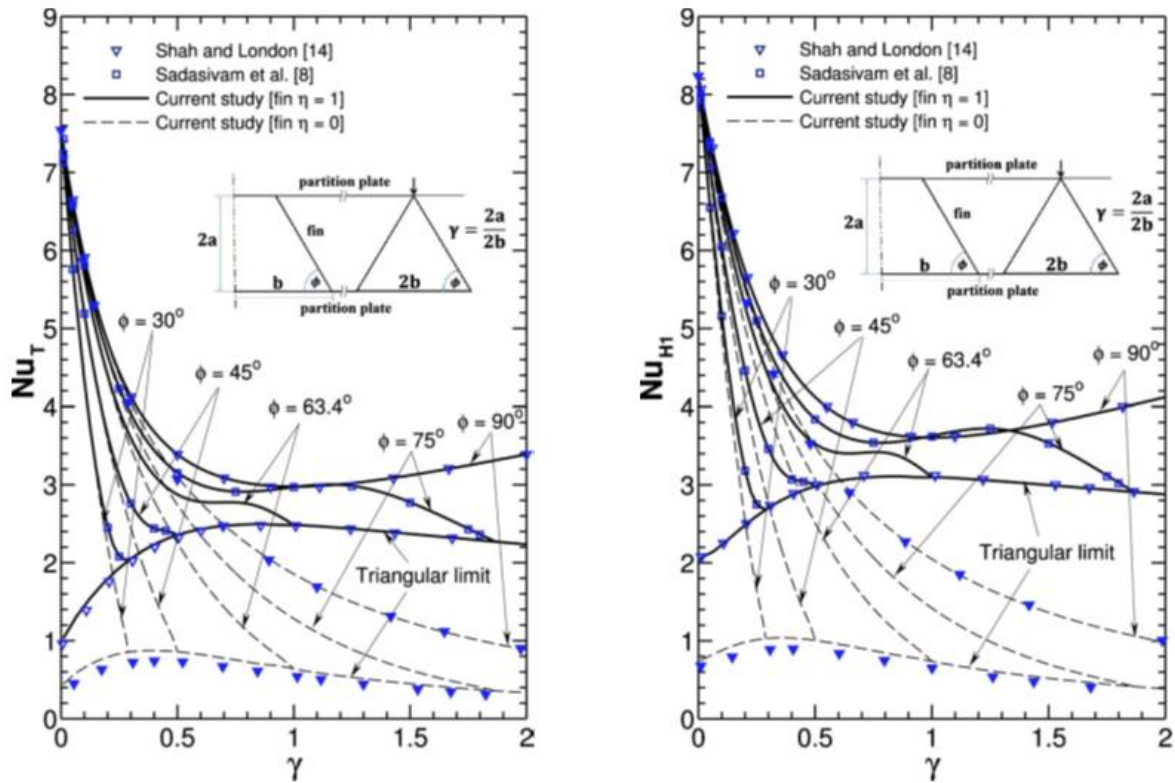


Figure 2.4: Huzayyin et al.'s [7] Nusselt numbers for fully developed laminar flow through trapezoidal channel cross section in a plate-fin core with uniform wall temperature, T (right), and uniform heat flux, $H1$ (left).

The rectangular channel cross section, denoted by $\phi = 90^\circ$ in Figure 2.4, results in the upper Nusselt number limit for both uniform wall temperature and uniform heat flux conditions when compared to trapezoidal and triangular fin channel geometries. Rectangular channels will result in higher Nusselt numbers and therefore higher heat transfer coefficients allowing for a

more compact plate-fin heat exchanger design. Because of this, rectangular channels were chosen for this project.

2.2 Pressure Drop Analysis

2.2.1 Single-phase Pressure Drop in Lanced Offset Strip Fins

Many studies have been done to collect and correlate experimental data on lanced offset strip fins. Manglik and Bergles [10] compare six heat transfer and friction factor correlations for flow through rectangular offset strip fins developed prior to 1995 and propose correlations of their own which apply for the laminar, transition, and turbulent flow regimes. Figure 2.5 below shows the geometrical description Manglik and Bergles [10] chose to use in their study for lanced offset strip fins.

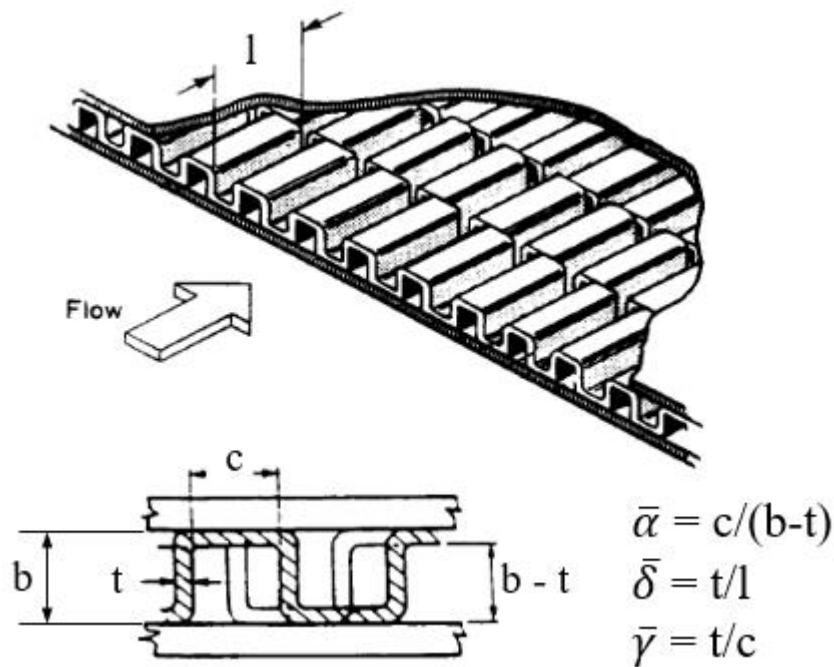


Figure 2.5: Manglik and Bergles [10] geometric parameters for lanced offset strip fins.

Data was collected for 18 offset strip fin surfaces and used to develop correlations for the heat transfer and friction factors in terms of the three parameters $\bar{\alpha}$, $\bar{\delta}$, and $\bar{\gamma}$. Reynolds number,

hydraulic diameter, and the friction factor correlation for offset strip fins are given below in equations 1-3.

$$Re = \frac{\dot{m} d_h}{\mu A_c} \quad (1)$$

$$d_h = \frac{4c(b-t)l}{2(cl + (b-t)l + t(b-t)) + tc} \quad (2)$$

Where A_c is total cross-sectional area, d_h is hydraulic diameter, and \dot{m} is mass flow rate.

$$f = 9.6243Re^{-0.7422}\bar{\alpha}^{-0.1856}\bar{\delta}^{0.3053}\bar{\gamma}^{-0.2659}\left(1 + 7.669 \times 10^{-8} Re^{4.429}\bar{\alpha}^{0.920}\bar{\delta}^{3.767}\bar{\gamma}^{0.236}\right)^{0.1} \quad (3)$$

The proposed friction factor correlation was derived using air as the working fluid for a Reynolds number range of $120 - 10^4$. Manglik and Bergles's [10] experimental data and their friction correlation agreed to within $\pm 20\%$ with some inherent scatter due to manufacturing variations of the lanced offset strip fin stock. Overall pressure drop can be calculated once the friction factor is known. Guo [11] outlines this process in his work on optimizing plate-fin heat exchangers. Single-phase pressure drop across the core of a heat exchanger can be found using equation 4 below.

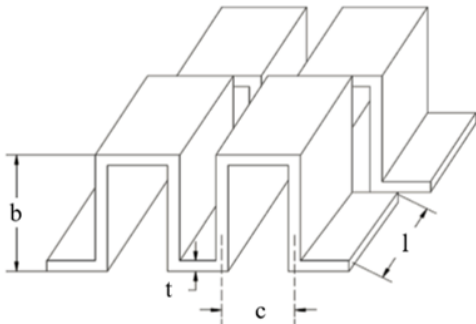
$$\Delta P = \frac{2 f L \dot{m}^2}{\rho d_h A_{c,total}^2} \quad (4)$$

A sensitivity study was done on fin geometry and its impact on overall pressure drop for single-phase flow through lanced offset-strip fins. The 350 W cooling capacity using PAO as the secondary refrigerant project requirements mentioned in chapter one were used during the analysis. The baseline heat exchanger dimensions and operating conditions used for the pressure and heat transfer coefficient analyses done later are shown in Table 2.1 below. Baseline fin height, b , and length, l , were selected as the smallest available in commercial industry in order to

minimize the evaporator size. The fin density, c , was also selected as the highest commercially available option of 11.02 fins-per-cm (28 fins-per-inch) for the same reasoning. Fin thickness, t , was chosen after conducting sensitivity analysis. Flow conditions for the PAO were fixed due to the project requirements. The R236ea flow conditions were calculated to provide the required 350 W of cooling for a fixed 10 °C of superheat and subcooling in the VCR cycle with a safety factor of 1.25.

Table 2.1: Heat exchanger geometry and operating conditions used for fin sensitivity analysis.

Baseline plate-fin heat exchanger parameters					
R236ea			PAO		
Parameter	Value	Units	Parameter	Value	Units
Layers	2		Layers	1	
Width of fin array	4.445	cm	Width of fin array	5.715	cm
Length of fin array	5.715	cm	Length of fin array	4.445	cm
Temperature inlet	20	°C	Temperature inlet	50	°C
Temperature outlet	25	°C	Temperature outlet	35	°C
Mass flow rate	0.004	kg/s	Mass flow rate	0.011	kg/s



Fin Geometry			
Fin height:	b	1.905	mm
Fin length:	l	3.175	mm
Fin thickness:	t	0.152	mm
Fin spacing:	c	0.755	mm
Cooling capacity		350	W
Local heat flux		200	W/m ²

For fin sensitivity analysis the values in Table 2.1 were maintained and only the specified parameters in each figure were varied one at a time. To analyze the PAO single-phase pressure drop, l , b , t , and c were all varied, and the predicted pressure drop plotted in Figures 2.6 and 2.7.

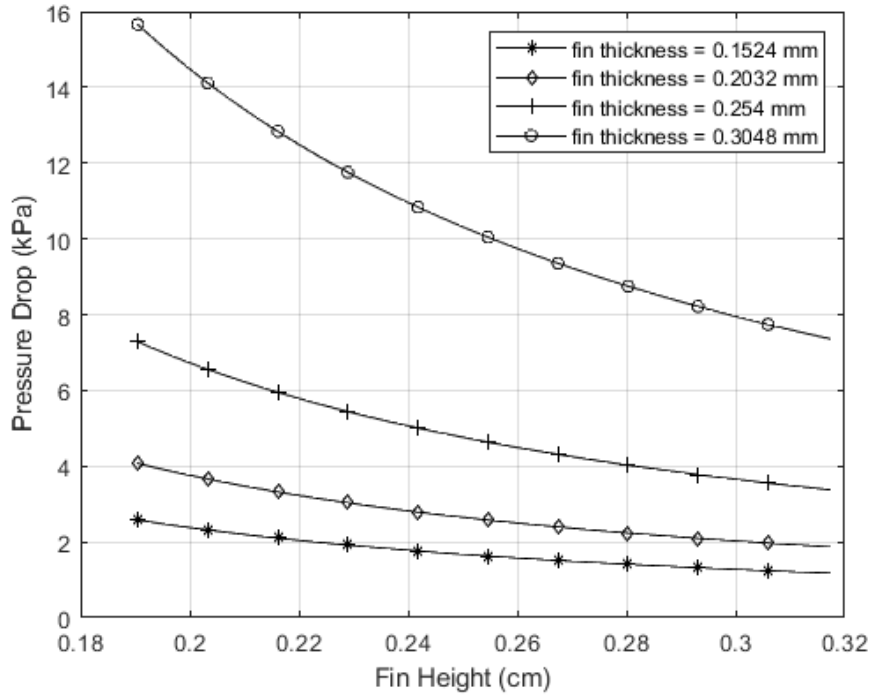


Figure 2.6: Pressure drop as a function of fin height, b , and thickness, t , for PAO flowing through offset strip fins.

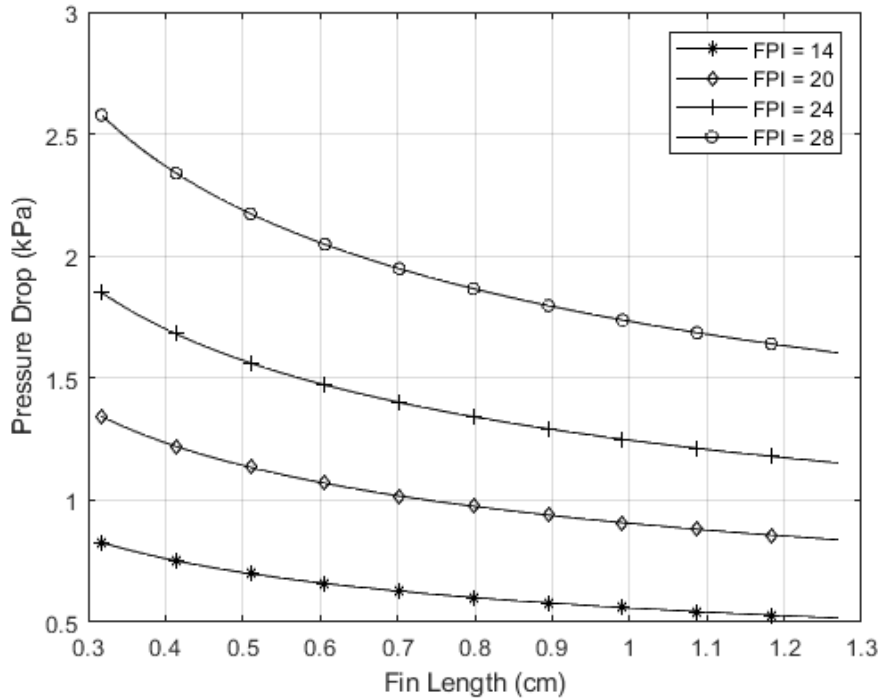


Figure 2.7: Pressure drop as a function of fin length, l , and fin spacing, c , for PAO flowing through offset strip fins.

The largest pressure drops are expected for short, closely spaced fins with thick walls and short heights. For the geometries analyzed, fin height appeared to have the most significant

impact on the pressure drop. Figure 2.6 shows that increasing the fin thickness from approximately 0.15 mm to 0.30 mm resulted in about an 800% increase in pressure drop. Fin pitch had an impact on pressure drop but to a lesser degree while fin length and fin height had a more gradual influence with pressure drop decreasing as both fin length and fin height increased.

2.2.2 Two-phase Pressure Drop in Lanced Offset Strip Fins

Two-phase pressure gradients are more complex than their single-phase counterparts for a multitude of reasons. Density differences between liquid and vapor result in flow acceleration pressure losses in addition to the normal frictional pressure losses. Raju *et al.* [12] experimentally analyzed flow boiling of R134a in lanced offset strip fins. A pressure loss due to the inlet header, friction, acceleration, gravity, and the outlet header were included in Raju *et al.*'s overall pressure drop model as shown below.

$$\Delta P_{tp} = \Delta P_{IH} + \Delta P_F + \Delta P_A + \Delta P_G + \Delta P_{OH} \quad (5)$$

Pressure losses within the headers were not considered when performing sensitivity analysis on fin geometry which simplified the overall pressure loss to the three middle terms.

The acceleration pressure gradient was calculated as

$$\Delta P_A = \dot{G}^2 \left[\frac{x^2 v_v}{\alpha} + \frac{(1-x)^2 v_l}{1-\alpha} \right] \quad (6)$$

where \dot{G} is the mass velocity, v_l is the liquid specific volume, f_f is the fluid friction factor, α is the local void fraction, x is local quality.

If the homogeneous equilibrium model is used for the flow, then the void fraction α can be expressed as

$$\alpha = \frac{1}{1 + \left(\frac{1-x}{x}\right) \left(\frac{\rho_v}{\rho_l}\right)} \quad (7)$$

Gravitational pressure gradient ΔP_G was expressed as

$$\Delta P_G = \left[\frac{\alpha}{v_v} + \frac{(1-\alpha)}{v_l} \right] g L \quad (8)$$

In the above equation, L is the length of heat exchanger containing vapor-liquid mixture, not the overall length of the plate-fin heat exchanger and ‘g’ denotes gravitational acceleration.

Frictional pressure losses for two-phase flow were expressed as

$$\Delta P_F = \frac{2 v_l \dot{G}^2 (1-x)^2 f_f \phi_f^2 L}{d_h} \quad (9)$$

Where the subscripts f, v, and l represent fluid, vapor, and liquid respectively. The two-phase frictional multiplier ϕ_f^2 for flow in round tubes was correlated by Lockhart and Martinelli [13] in terms of the Martinelli parameter X as shown.

$$\phi_f^2 = 1 + \frac{C}{X} + \frac{1}{X^2} \quad (10)$$

$$X = \frac{1-x}{x} \left(\frac{f_l \rho_v}{f_v \rho_l} \right)^{0.5} \quad (11)$$

Where the constant C depended on flow characteristics such as laminar and turbulent flow regimes. Kim and Sohn [14] improved upon Mandrusiak and Carey’s [15] experimental correlation for the two-phase frictional multiplier for offset strip fins. Kim and Sohn [14] collected data for R113 flowing in offset strip fins with a hydraulic diameter of 2.84 mm and came up with the following correlation for the two-phase frictional multiplier.

$$\phi_f^2 = 1 + \frac{23.4}{X} + \frac{4.17}{X^{2.66}} \quad (12)$$

This is very similar to Raju *et al.*’s [12] correlation for ϕ_f^2 which was based on data for R134a flowing through offset strip fins at a variety of mass fluxes, qualities, and applied heat fluxes.

Raju *et al.* proposed the following correlation as an approximate fit to their data.

$$\phi_f^2 = 1 + \frac{30}{X} + \frac{4}{X^2} \quad (13)$$

Kim and Sohn's [14] correlations were used to evaluate the impact fin geometry had on two-phase pressure drop of R236ea at 20 °C flowing through lanced offset strip fins. Exit quality was varied in addition to the fin geometry. Figure 2.8 shows the results of the fin geometry sensitivity analysis.

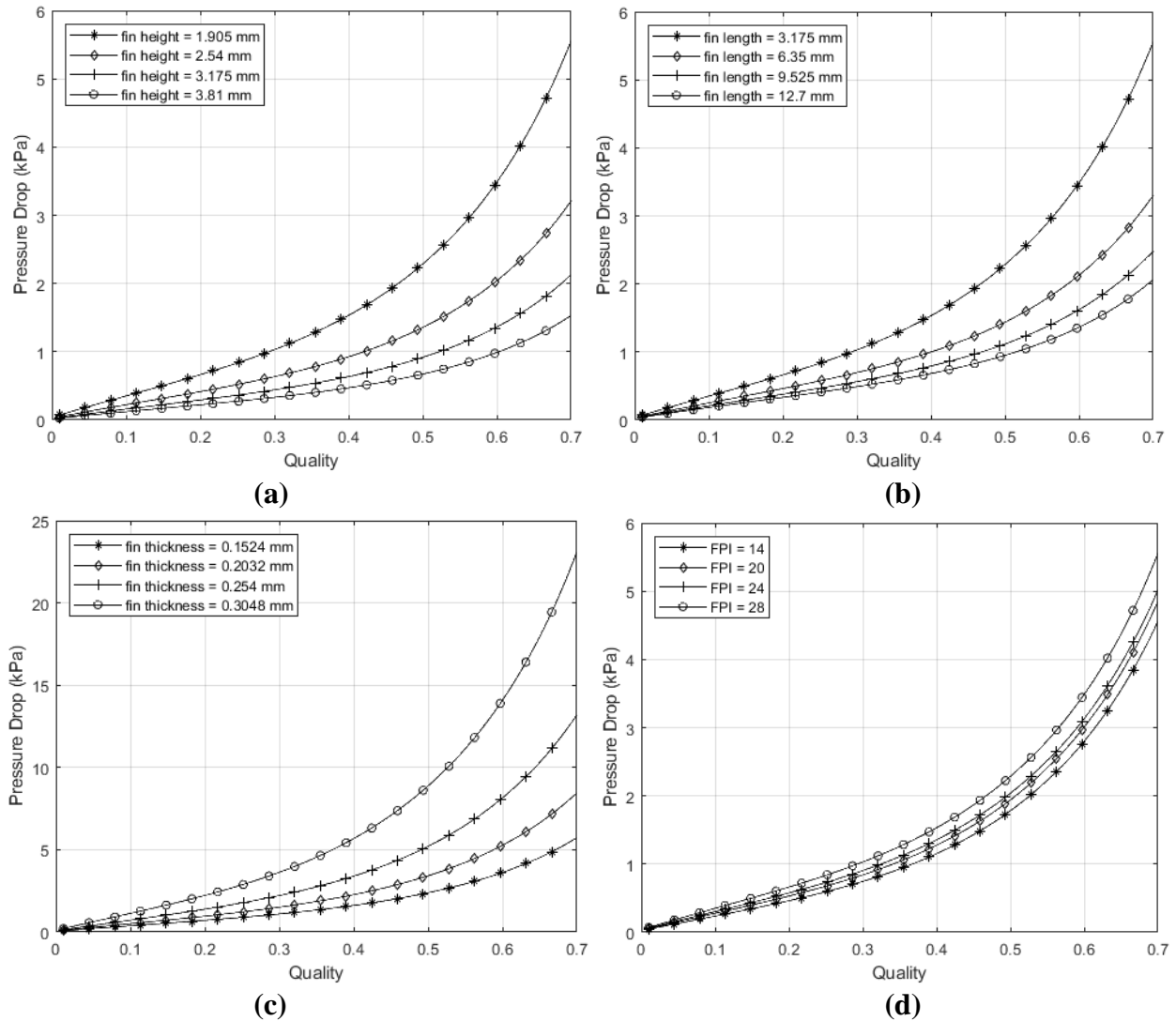


Figure 2.8: Two-phase pressure drop for R236ea flowing through offset strip fins as a function of (a) fin height, (b) fin length, (c) fin thickness, and (d) fin pitch.

Like the single-phase pressure drop analysis, varying fin thickness resulted in the largest changes in two-phase pressure drop. As was expected, pressure drop increased as exit quality

increased. Figure 2.8 only shows exit qualities up to 70% since the flow regime most likely changes to single-phase vapor flow before reaching an exit quality of 100% as Carey [16] discusses in chapter 12 of his book *Liquid-Vapor Phase-Change Phenomena* (pages 583-702). For round horizontal tubes, dryout has been observed for exit quality values around 30%.

Reviewing the single-phase and two-phase pressure drop sensitivity analyses done, it appears that using thinner fins is the most effective way of achieving the lowest pressure drops for fluid flowing through lanced offset strip fins.

2.3 Heat Transfer Analysis

2.3.1 Single-phase Heat Transfer for Lanced Offset Strip Fins

Heat transfer performance for single-phase fluid flow through lanced offset strip fins can be evaluated using the Colburn j factor proposed by Manglik and Bergles [10].

$$j = 0.6522Re^{-0.5403}\bar{\alpha}^{-0.1541}\bar{\delta}^{0.1499}\bar{\gamma}^{-0.0678}\left(1 + 5.269 \times 10^{-5}Re^{1.340}\bar{\alpha}^{0.504}\bar{\delta}^{0.456}\bar{\gamma}^{-1.055}\right)^{0.1} \quad (14)$$

The geometric parameters $\bar{\alpha}$, $\bar{\delta}$, and $\bar{\gamma}$ used by Manglik and Bergles [10] are shown earlier in Figure 2.5. Once the Colburn j factor is calculated, the heat transfer coefficient h_f can be found using the following relationship.

$$j = \frac{h_f}{\dot{G} c_p} Pr^{\frac{2}{3}} \quad (15)$$

The same cooling capacity of 350 W and PAO temperature change of 15 °C used when analyzing the single-phase pressure drop was applied to the single-phase heat transfer fin geometry sensitivity analysis. Fin height, length, thickness, and spacing were all varied for a fixed mass flow rate and heat exchanger geometry.

The overall heat transfer coefficient was calculated for each fin geometry using the Colburn j factor provided by Manglik and Berghes [10]. Figures 2.9 and 2.10 show the results of the single-phase heat transfer sensitivity analysis for lanced offset strip fins. Note that pertinent heat exchanger geometry and operating conditions were provided earlier in Table 2.1.

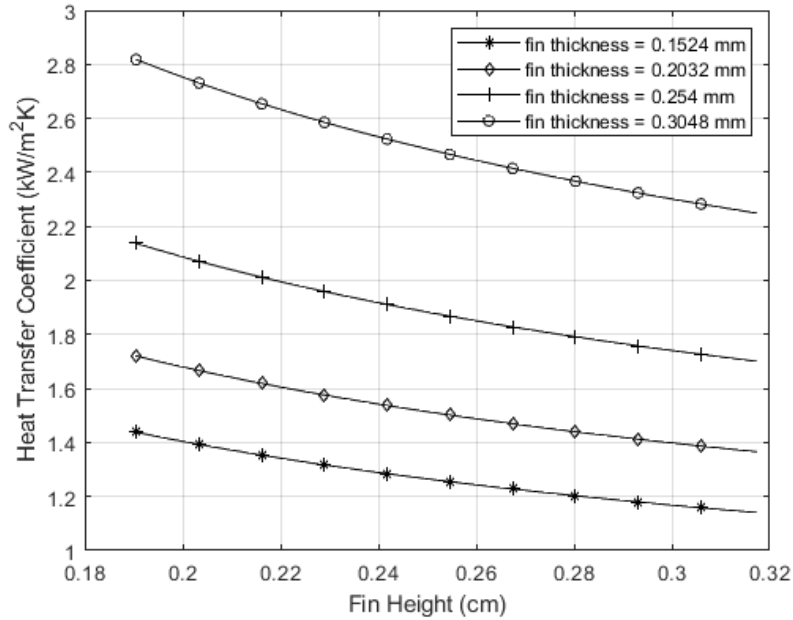


Figure 2.9: Heat transfer coefficient as a function of fin height and thickness for PAO flowing through offset strip fins.

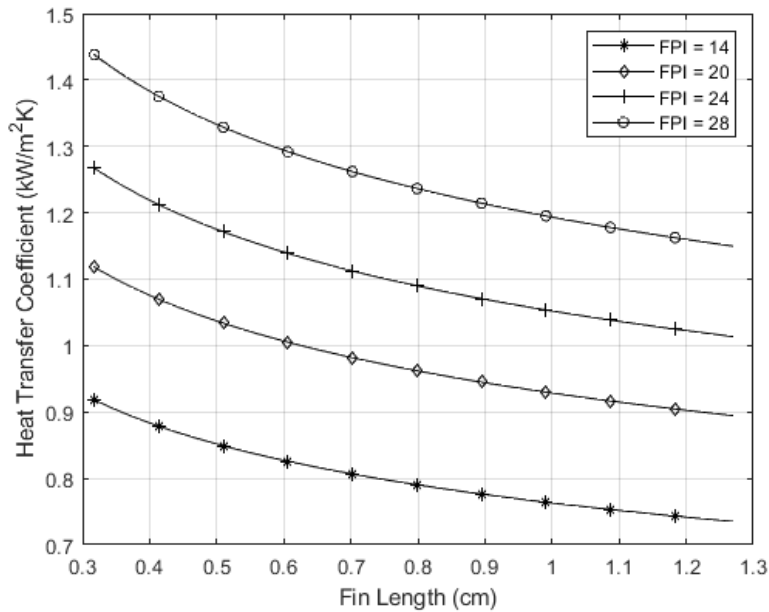


Figure 2.10: Heat transfer coefficient as a function of fin length and fin spacing for PAO flowing through offset strip fins.

As was expected, fins with smaller hydraulic diameters resulted in higher heat transfer coefficients. Fin pitch and fin thickness had the largest impact on the heat transfer coefficient followed by fin length and then fin height. To get the best performance while maintaining a compact volume, short fin lengths, thick fin walls, and closely spaced fins should be used. Fin height, which increases required volume the most, can be reduced while impacting the overall single-phase heat transfer coefficient the least.

2.3.2 Two-phase Heat Transfer for Lanced Offset Strip Fins

In two-phase flow boiling, heat is transferred by both nucleate boiling and forced convection. The overall local two-phase heat transfer coefficient, h_{tp} , is commonly modeled as the sum of the nucleate boiling heat transfer coefficient h_{nb} and the convective boiling heat transfer coefficient h_{cb} as proposed by Chen [17].

$$h_{tp} = h_{nb} + h_{cb} \quad (16)$$

Chen [17] correlated the two-phase forced convective heat transfer coefficient as a function of the single-phase heat transfer coefficient and the Reynolds number factor F .

$$h_{cb} = F h_f \quad (17)$$

Kim and Sohn's [14] study of lanced offset fins suggested that Chen's [17] proposed correlation for the Reynolds number factor F , which was based on round tubes, was not applicable to flow boiling in plate-fin channels. Kim and Sohn [14] presented a new correlation for the Reynolds number factor as a function of the Martinelli parameter which was based upon their experimental data.

$$F = \left[1 + \frac{2.52}{X^{1/2}} + \frac{15.1}{X^2} \right]^{0.5} \quad (18)$$

Nucleate boiling heat transfer, which is strongly dependent on local wall superheat, occurs differently on the exposed wall or base plate (primary surface) than on fins (secondary surfaces) due to the temperature gradient within the fins. Nishikawa *et al.* [18] proposed that the nucleate boiling component of local boiling heat transfer could be found using the suppression factor S and the pool boiling heat transfer coefficient h_{pb} .

$$h_{nb} = S h_{pb} \quad (19)$$

$$h_{pb} = 3.14 \left[\frac{P_c^{0.2} F_p}{M^{0.1} T_c^{0.9}} \right] q''^{0.8} \quad (20)$$

$$F_p = \frac{(P/P_c)^{0.23}}{[1.0 - 0.99(P/P_c)]^{0.9}} \quad (21)$$

In Nishikawa *et al.*'s [18] proposed pool boiling correlation, M is the molecular weight, q'' is the local heat flux, and the subscript c denotes the critical constant. Both Kim and Sohn [14] and Raju *et al.* [12] use the suppression factor for flow boiling in round tubes suggested by Bennett *et al.* [19] due to the lack of accurate experimental correlations for other geometries.

$$S = \frac{24.4}{N_B} [1 - e^{-0.041N_B}] \quad (22)$$

$$N_B = \frac{h_f}{k_f} \left[\frac{\sigma}{g(\rho_f - \rho_g)} \right]^{0.5} \quad (23)$$

Fin geometry sensitivity analyses were also calculated for the two-phase heat transfer coefficient. The results are shown in Figure 2.11 below.

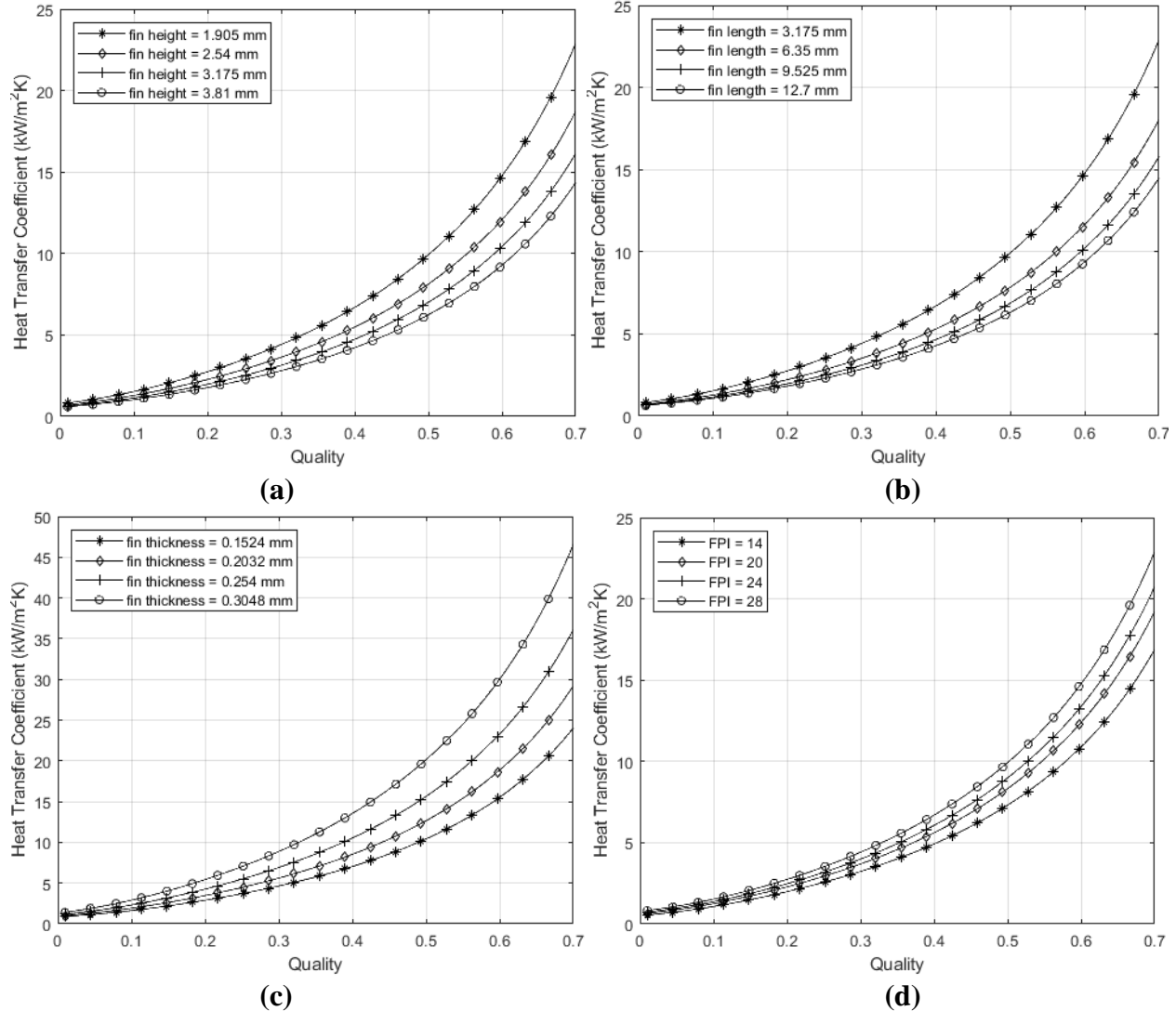


Figure 2.11: Two-phase heat transfer coefficient for R236a flowing through offset strip fins as a function of (a) fin height, (b) fin length, (c) fin thickness, and (d) fin pitch.

Different fin heights, lengths, and pitches all resulted in convection coefficients ranging from approximately $0.7 - 23.0 \frac{kW}{m^2K}$ with similar behavior for each fin parameter as the vapor quality increased. Figure 2.11 shows the convection coefficients for the fin parameters listed above. Fin thickness had a significant difference on the two-phase heat transfer coefficient when compared to fin height, length, and pitch. For the values of fin thickness considered in Figure 2.11, the heat transfer coefficient increased to almost $46 \frac{kW}{m^2K}$ at a quality of 70%. The total range of the heat transfer coefficient for the various fin thicknesses was much larger than the

ranges for fin length, height, and fin pitch. At the final quality of 70% shown in Figure 2.11 heat transfer coefficients reached a maximum of 46 kW/m²K for the thickest fins while the shortest fin height, shortest fin length, and highest fin count only resulted in a maximum heat transfer of approximately 22 kW/m²K for the same quality.

However, for all the fin parameters analyzed, the impact on the two-phase heat transfer coefficient was much more pronounced at high qualities. Since dryout occurs well before a quality of 100%, these extreme variations in two-phase heat transfer at high qualities are not accurate. Values for qualities near 50% are much closer to the maximum possible heat transfer coefficient than h values for higher qualities as discussed by Raju *et al.* [12] who pointed out that a gradual decrease in heat transfer coefficient occurs for qualities higher than 50% due to the transition to single-phase vapor flow. Because of this, the higher values of h for qualities above approximately 50% shown in Figure 2.11 were not used. Instead, a decreasing heat transfer coefficient behavior is assumed and used when determining an overall average heat transfer coefficient and the corresponding required heat exchanger size.

2.4 Final Fin selection for Evaporator

Decreasing fin height, length, and spacing and increasing fin thickness all resulted in higher heat transfer coefficients and higher pressure drops. Since pressure drop was most significantly impacted by fin thickness that parameter was kept small despite the positive increases in heat transfer coefficients when it was increased. Decreasing fin height, length, and spacing all increased the heat transfer coefficient without increasing the pressure drop too significantly so those three parameters were minimized. Since the evaporator must fit within an ATR chassis, a flat, wide design was chosen. For this reason, low fin heights with high fin density and short fin length were chosen as ideal. Commercially available fin stock with the

smallest fin height, length, and spacing was chosen and the final baseline fin geometry is shown in Table 2.2.

Table 2.2: Final fin geometry selection for evaporator.

Fin Geometry	
Fin height	1.905 mm
Fin length	3.175 mm
Fin thickness	0.152 mm
Fin spacing	0.755 mm

2.5 Header Flow Distribution

Achieving uniform heat transfer performance in a heat exchanger often depends on providing a uniform flow. This can be done by analyzing various header geometries and adding baffles to uniformly spread incoming refrigerant prior to it entering the finned channels of the heat exchanger. Maldistributed flow, which occurs when incoming refrigerant is not evenly distributed through each channel, can result in widely varied heat transfer within the core of a heat exchanger. The two most common header designs, an I-type and C-type were considered for this project. Figure 2.12 below shows the differences between the two headers.

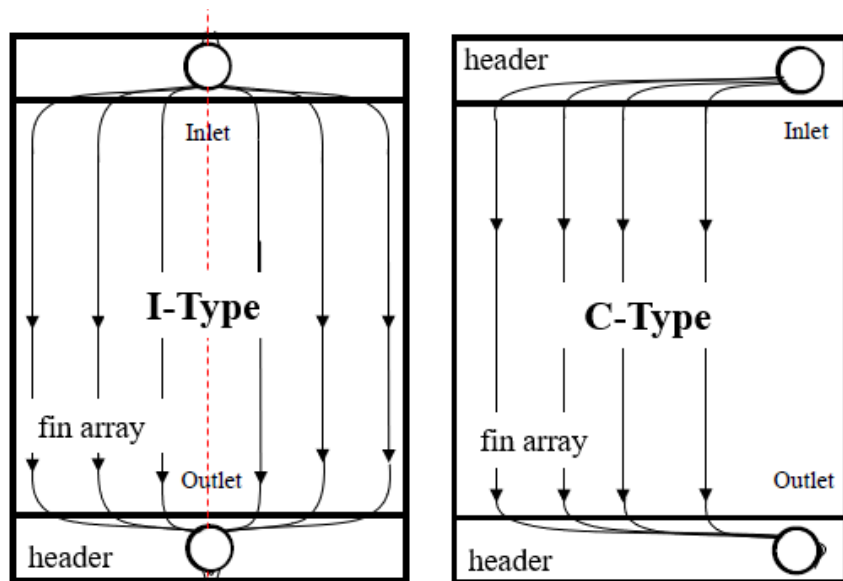


Figure 2.12: I-type header design (left) and C-type header design (right).

Each header design was analyzed for a rectangular, trapezoidal, and trapezoidal with baffle configuration using the software package Flotherm [20]. The trapezoidal configurations were created by decreasing the header depth away from the inlets and outlets so that the flow cross-sectional area within the header decreased as the fluid moved away from the inlet and outlet. Rectangular headers such as the ones shown in Figure 2.12 often result in maldistributed flow since a large amount of fluid flows through the fins close the inlet and less fluid flows through the fins farthest from the inlet. Adding baffles, which are perforated walls located slightly before the fluid reaches the fins, helps filter the flow into more uniform streams. For this project, the PAO flow through each header design was simulated using Flotherm which is a leading product in the field of electronic thermal management and uses CFD to analyze thermal and fluid flow. Each header design was modelled within Flotherm using dimensions from Table 2.1. A rectangular meshing scheme was used during the analysis. Figure 2.13 shows the six header models analyzed.

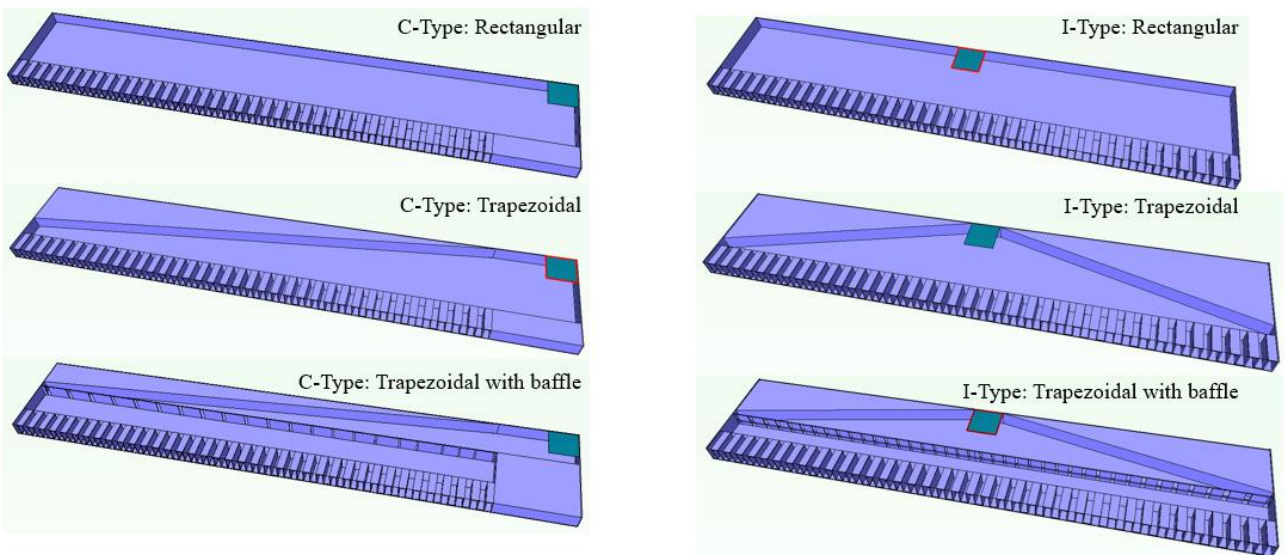


Figure 2.13: Six evaporator header configurations analyzed using Flotherm.

A grid independence study was done which varied element count for the I-type rectangular header. Individual channel velocities were compared for each iteration of element count so that a

mesh could be chosen which would accurately capture the PAO velocity through the fins. Figure 2.14 shows the results of the grid independence study.

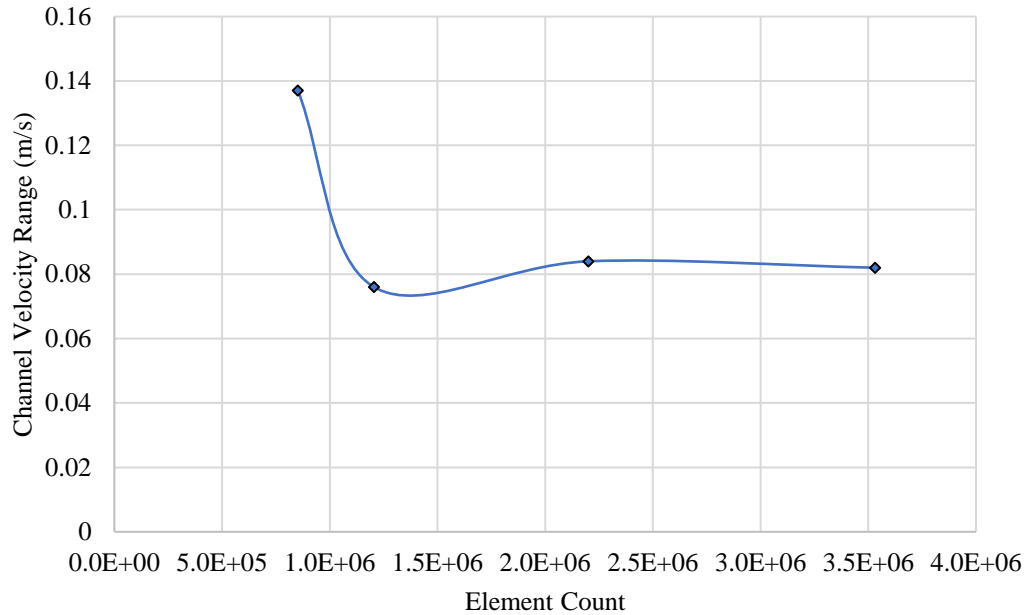


Figure 2.14: Velocity range across fin channels vs. element count for I-type rectangular header.

Final baffle geometry was selected by iterating baffle slot locations and size until a reasonable flow distribution through each channel was achieved. Figure 2.15 below shows this progression with the leftmost plot showing flow distribution for the first baffle design and the rightmost plot showing flow distribution for the final baffle design.

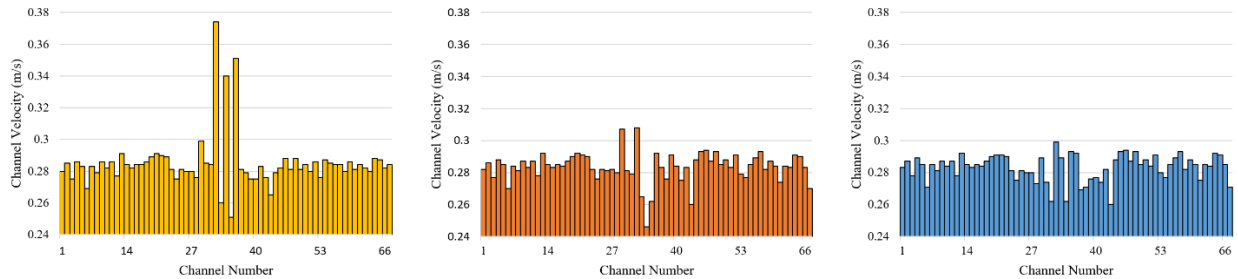


Figure 2.15: Individual channel velocities for I-type header with first baffle design (left), second baffle iteration (middle), and final baffle design (right).

Figure 2.15 clearly shows the severe flow misdistribution which occurred for the I-type header with increased PAO flow occurring in the central channels near the header inlet. Custom baffles were designed separately for both the I-type and C-type headers for the final comparison as seen in Figure 2.16 which illustrates velocity profiles of the PAO for both the I-type and C-type trapezoidal headers with custom baffles designed to evenly distribute the flow.

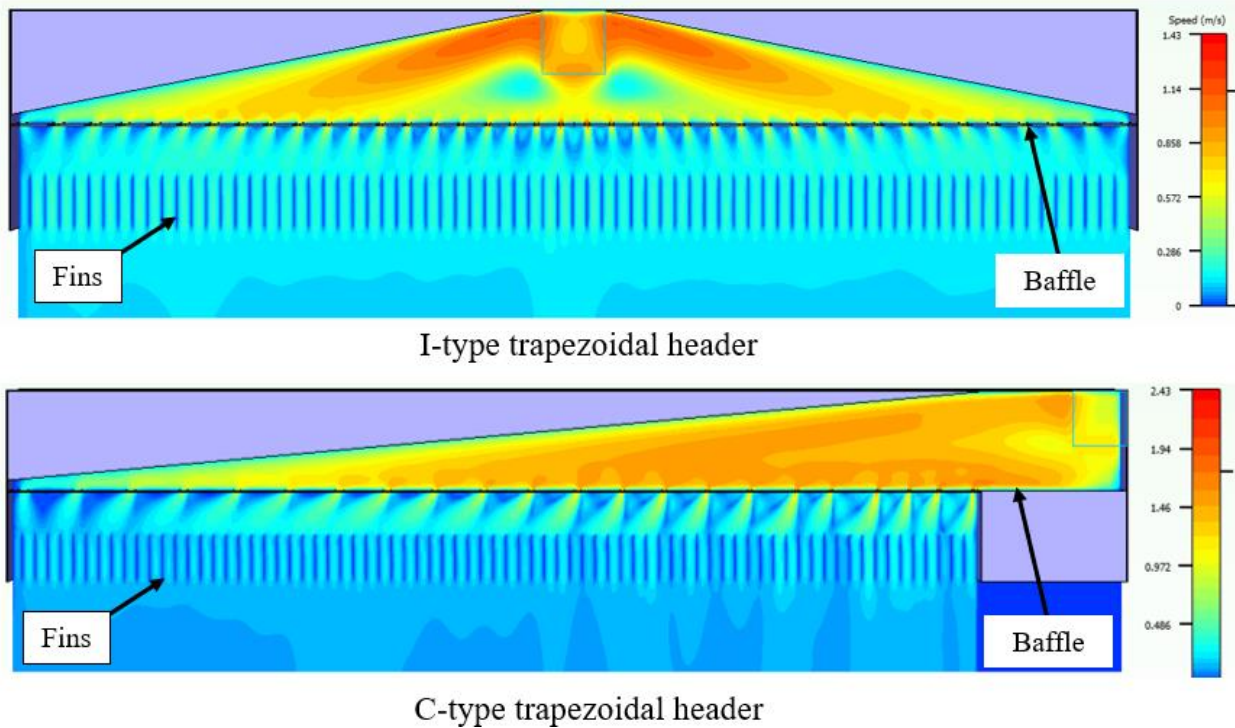


Figure 2.16: Velocity profiles for PAO flowing through an I-type trapezoidal header with baffle (top) and C-type trapezoidal header with baffle (bottom) modelled using Flotherm.

The I-type header resulted in a much more uniform flow when compared to the C-type header geometry. This was quantified using a coefficient of variation defined below

$$\text{Coefficient of Variation} = \frac{\text{velocity standard deviation}}{\text{mean velocity}} \quad (24)$$

Where the velocities are calculated for each channel in the first row of fins.

Simulation results are shown in Table 2.3 below.

Table 2.3: Results from header simulation analysis.

I-type (trapezoidal w/ baffle)		C-type (trapezoidal w/ baffle)	
Range	0.05	Range	0.397
Mean	0.222	Mean	0.218
Variance	0.0001	Variance	0.004
Standard deviation	0.0106	Standard deviation	0.066
Coefficient of variation	0.048	Coefficient of variation	0.303

Comparing the coefficient of variation for the two header designs clearly shows that the I-type header results in more uniformly distributed flow.

Chapter 3: Full Cycle Analysis for the Vapor Compression Refrigeration System

To account for the limited power supply, high ambient temperatures, and aid in refrigerant selection, a full cycle analysis of the compressor, condenser, expansion device, and evaporator was done using MATLAB. Compressor isenthalpic efficiency was taken to be 65% as a lower limit due to mechanical, thermal, leakage, pressure, and electrical-to-mechanical conversion losses. Air-squared, a leading company in highly compact scroll compressors, lists [21] the efficiencies of their products slightly higher than the 65% lower limit chosen for this analysis. The maximum compressor exit temperature was chosen to be 130 °C. At discharge temperatures higher than 130 °C, worn rings, acid formations, and oil breakdown may occur within the compressor resulting in failure. A full cycle analysis was able to account for the maximum compressor temperature design limitation. The two-phase pressure drop within the condenser was approximated to be the same as the evaporator due to the primary focus of this project being on the evaporator with no robust condenser design or the corresponding correlations having been chosen. The degrees of superheat and subcooling within the evaporator and condenser were evaluated at 10 °C and 5 °C for this analysis. The expansion valve was modelled as an isenthalpic process between the condenser and evaporator. Finally, the evaporator was modelled using the geometry listed in Table 2.1 and the corresponding correlations for heat transfer and pressure drop discussed previously. Ambient temperatures were varied from 45 °C to 65 °C with required compressor power and operating temperatures and pressures as outputs. The results of the full cycle analysis for the various ambient conditions are shown below in Figures 3.1 and 3.2.

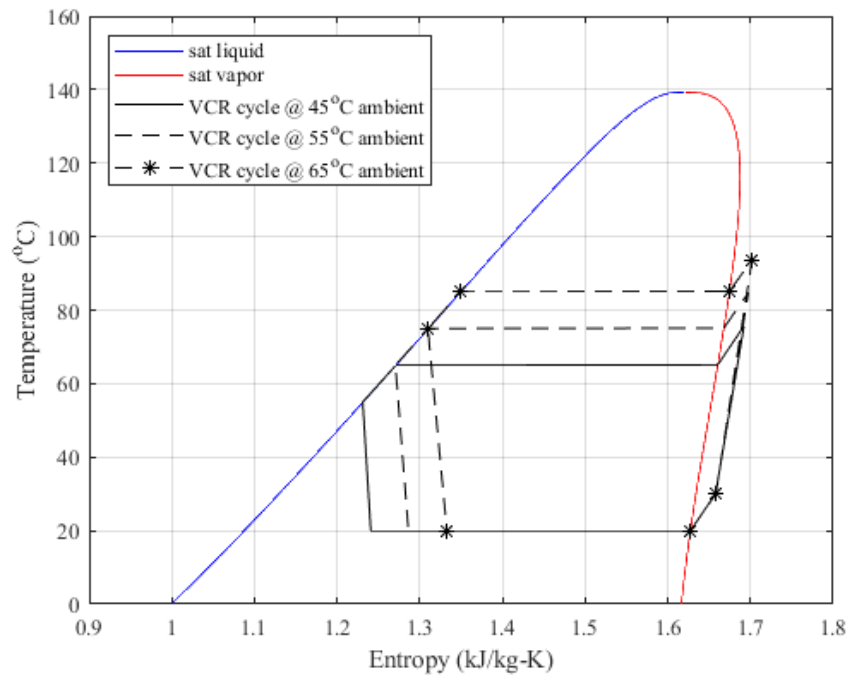


Figure 3.1: Temperature vs. entropy plot for vapor compression refrigeration cycle operating at various ambient temperatures.

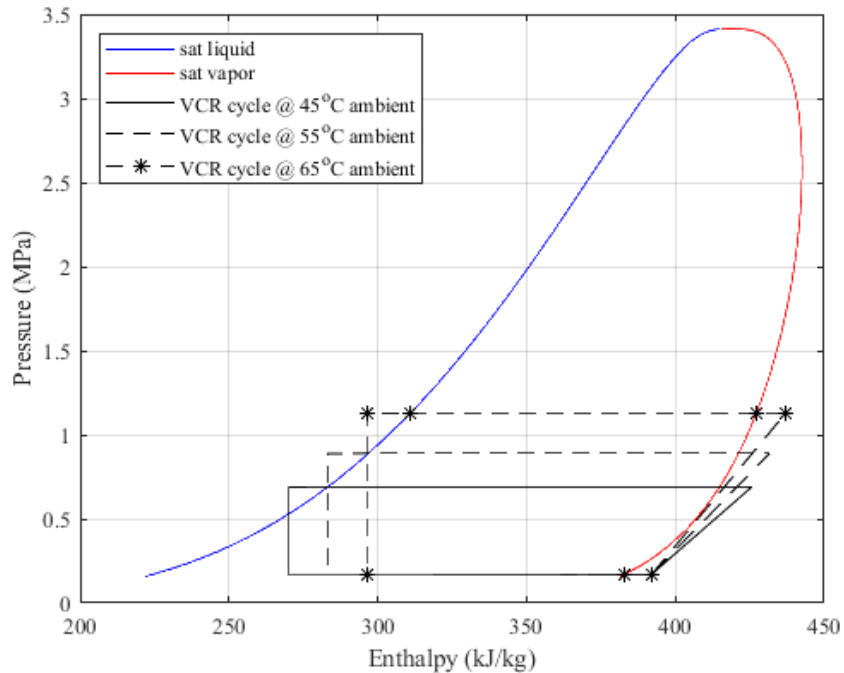


Figure 3.2: Pressure vs. enthalpy plot for vapor compression refrigeration cycle operating at various ambient temperatures.

For both Figures 3.1 and 3.2, the compression process is shown as a steep near-vertical line on the far right of the VCR cycle loop and the isenthalpic expansion valve is shown as a vertical line on the far left of the cycle. The evaporator and condenser heat transfer processes are shown as the top and bottom nearly horizontal lines respectively.

Mass flow rate within the refrigeration system had to vary to maintain a fixed cooling capacity of 350 W under the three different ambient temperatures. This resulted in different compressor power, maximum temperatures within the VCR cycle, and evaporator inlet qualities of the refrigerant. These parameters are listed below in Table 3.1.

Table 3.1: Vapor compression refrigeration cycle parameters for system operating in various ambient temperatures with fixed cooling capacity and 10 °C of subcooling and superheat.

Ambient Temperature	Maximum Temperature	Mass Flow Rate	Compressor Power	Cooling Capacity	Inlet Quality
°C	°C	kg/s	W	W	
45	75.7	0.0029	97	350	0.28
55	84.8	0.0032	128	350	0.37
65	93.7	0.0037	166	350	0.45

Degrees of superheat and of subcooling were lowered from 10 °C to 5 °C and the full cycle analyzed for the same three ambient temperatures. Lowering the required amount of superheating at the evaporator exit and the amount of subcooling at the condenser exit resulted in lower compressor power consumption and compressor exit temperatures as expected. The changes resulting from lower superheat and subcooling are shown below in Table 3.2.

Table 3.2: Vapor compression refrigeration cycle parameters for system operating in various ambient temperatures with fixed cooling capacity and 5 °C of subcooling and superheat.

Ambient Temperature	Maximum Temperature	Mass Flow Rate	Compressor Power	Cooling Capacity	Inlet Quality
°C	°C	kg/s	W	W	
45	66.0	0.0030	89	350	0.28
55	75.2	0.0034	120	350	0.37
65	84.3	0.0039	160	350	0.45

The same operating conditions were used to evaluate the refrigeration system but with constant compressor power instead of constant cooling capacity. Compressor power was fixed at the maximum allowable of 360 W. The temperature-entropy and pressure-enthalpy plots for the constant compressor power cycles were very similar to the previous cycles shown in Figures 3.1 and 3.2. New values for maximum temperature, mass flow rate, inlet quality, and cooling capacity were recorded in Table 3.3 below.

Table 3.3: Vapor compression refrigeration cycle parameters for system operating in various ambient temperatures with fixed compressor power and 10 °C of subcooling and superheat.

Ambient Temperature	Maximum Temperature	Mass Flow Rate	Compressor Power	Cooling Capacity	Inlet Quality	PAO Exit Temperature
°C	°C	kg/s	W	W	N/A	°C
45	79.2	0.0098	360	1226	0.27	-2.6
55	87.2	0.0086	360	977	0.34	8.1
65	95.4	0.0077	360	787	0.41	16.3

Note that for at the designed operating ambient temperature of 55 °C, the cooling capacity increased from the target amount of 350 W to approximately 977 W when the compressor was run continuously at the maximum available power. Running the compressor at max power resulted in a PAO exit temperature of 8 °C instead of 35 °C which is the exit temperature requirement. Comparing constant capacity results to constant compressor power

result at 10 °C of subcooling and superheat resulted in compressor exit temperatures increasing slightly from 84.7 °C to 87.2 °C. All compressor exit temperatures calculated were significantly below the limiting allowable compressor exit temperature of 130 °C.

Chapter 4: Numerical Simulation Setup

A numerical analysis was done of the PAO flow within the evaporator and compared with the correlations for lanced offset strip fins used earlier. The software used for analyzing the flow through lanced offset strip fins was ANSYS® Fluent, Academic Research, Version 19.2. A full guide on how ANSYS Fluent was used to model, mesh, and solve flow through lanced offset strip fins is included in Appendix B.

4.1 Geometry

To generate data from Fluent’s CFD analysis of the PAO flow that can be compared to Manglik and Bergles [10] data on lanced offset strip fins, a center section of the evaporator was considered. This resulted in ignoring the edge effects of the evaporator and allowed for periodic boundary conditions when performing the analysis. A model of the lanced offset strip fin core analyzed within ANSYS Fluent is shown below in Figure 4.1.

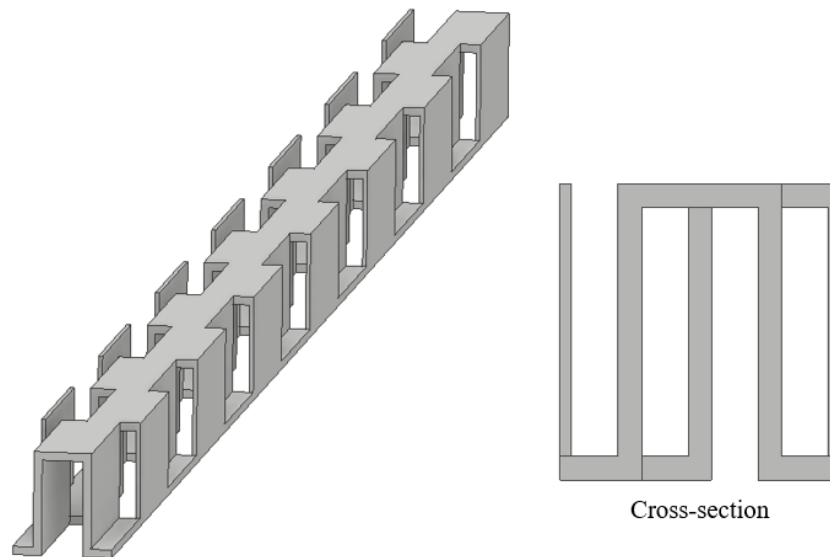


Figure 4.1: 3D model of lanced offset strip fin section analyzed in Fluent.

To model flow through the lanced offset strip fin section shown in Figure 4.1, a 3D model of the fluid within the fins was created and imported into Fluent. Fluid inlet and exit plenum regions were added to the front and back of the finned section. The fluid domain with inlet and outlet regions is shown in Figure 4.2.

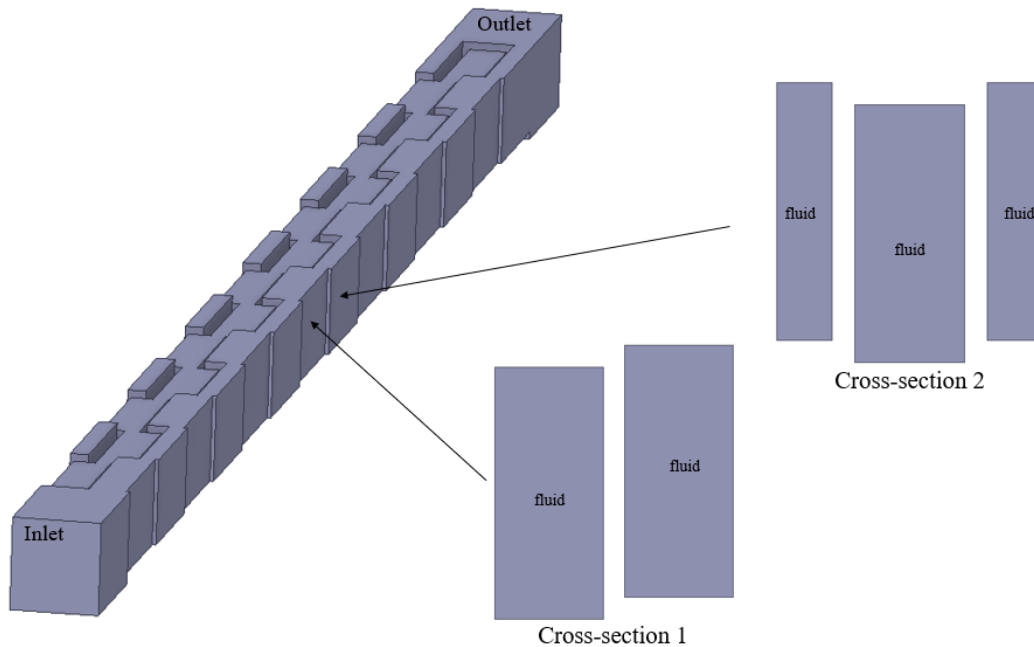


Figure 4.2: 3D model of fluid region within lanced offset strip fin core.

4.2 Mesh

The fins and fluid region were meshed using ANSYS Workbench 19.2. Both the fluid and solid fin regions were meshed using tetrahedral elements with a specified fine element size imposed at the fluid-solid interface. Inflation controls were used within the fluid to refine the mesh at the finned surfaces to resolve boundary layer and allow for larger mesh to be used throughout the remaining fluid volume. Figure 4.3 below shows the final mesh within the lanced offset strip fin core geometry. A detailed description of the mesh geometry and refinements used for this project can be found in Appendix A.2.

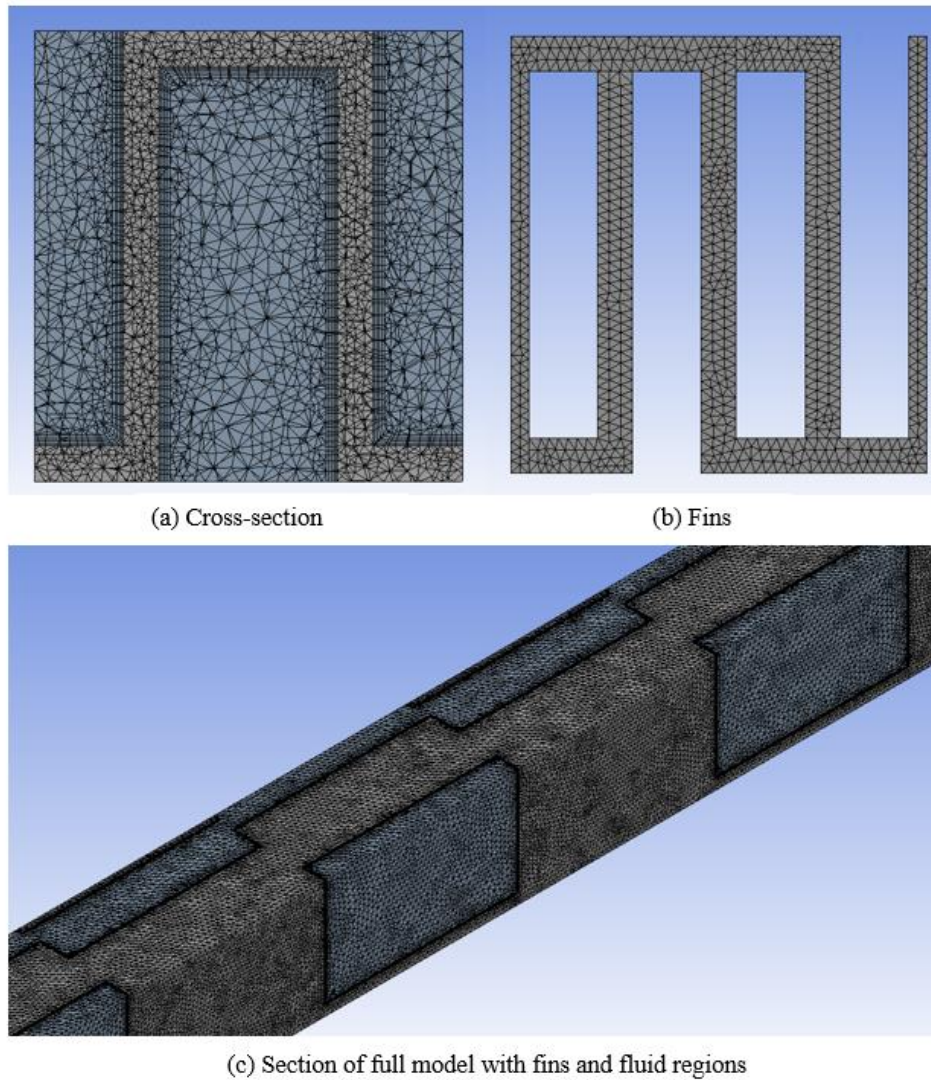


Figure 4.3: Meshed model of the 14-row lanced offset strip fins section.

Figure 4.3a clearly shows the inflation within the fluid at the fluid-solid interface used to capture the boundary layer region. A coarser tetrahedral mesh was used within the fins as shown in Figure 4.3b.

4.3 Fluent

Boundary conditions and model details used during the Fluent analysis are shown below in Figure 4.4.

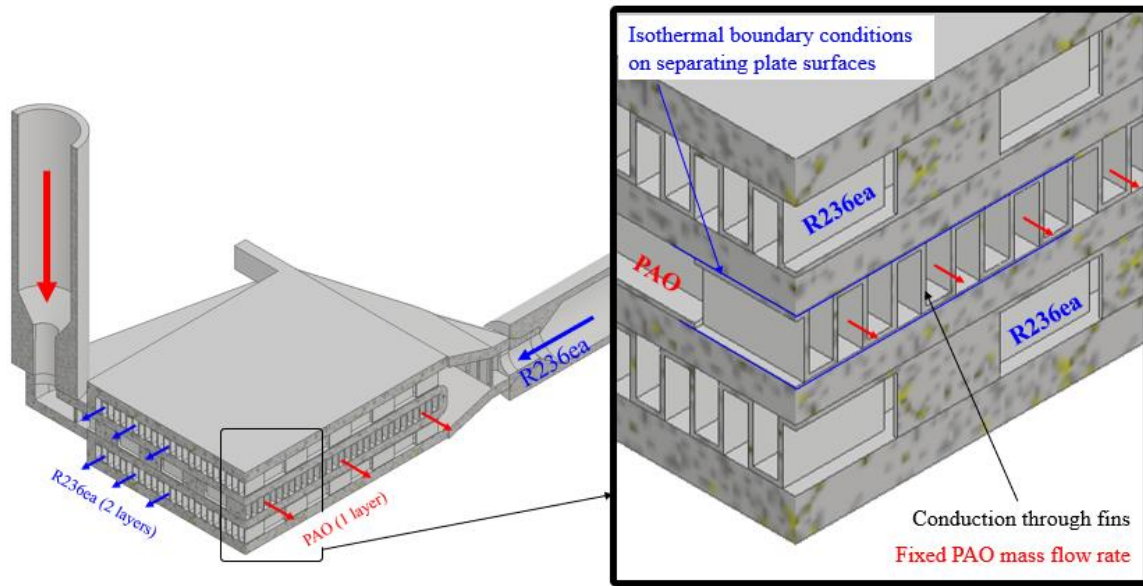


Figure 4.4: Boundary conditions applied to Fluent model for PAO flow through lanced offset strip fins.

Material properties were all manually entered into ANSYS Fluent since Polyalphaolefin properties were not included in Fluent’s database. These values are shown in Table 4.1 Tabulated data for PAO fluid properties as a function of temperature were difficult to attain due to many companies choosing not to publish them publicly. Using temperature dependent PAO fluid properties would be an excellent future adjustment to the Fluent model.

Table 4.1: Polyalphaolefin properties.

Polyalphaolefin (PAO)			
Property	Units	Value	
Density	kg/m ³	770.0	
Specific Heat Capacity	J/kg-K	2150.0	
Fluid Thermal Conductivity	W/m-K	0.137	
Dynamic Viscosity	kg/m-s	0.009	

Due to the offset geometry of the fins a translational periodic boundary condition was imposed on both sides of the geometric model. The top and bottom surfaces of both the fluid and fins

were fixed at a constant temperature to approximate the extremely high heat transfer coefficient of the boiling R236ea. No-slip boundary conditions were applied to the fin walls as well as the top and bottom surfaces which contact the separating plates within the plate-fin heat exchanger. A uniform inlet velocity boundary condition and a pressure outlet boundary condition were applied to the inlet and outlet faces of the model shown in Figure 4.2. Due to the extremely low Reynolds numbers ranging from 10.8 – 19.5, only laminar flow was present, and no turbulence models were needed.

4.4 Grid Independence

A grid study was conducted on a simple two row model of the lanced offset strip fins with the same inlet and outlet plenum regions shown in Figure 4.2. The model was solved for increasingly refined meshes until resulting temperature and pressure fields showed grid independence. Mesh refinements were made by decreasing element size, decreasing element face sizing at the solid-fluid interface, and decreasing the inflation layer thickness as shown below in Table 4.2. The number of inflation layers, inflation growth rate, and grid smoothing was kept constant throughout the mesh study.

Table 4.2: Meshing parameters used for grid independence study.

	Mesh A	Mesh B	Mesh C	Mesh D	Mesh E	Mesh F	Mesh G
Element size	2.50E-04	2.50E-04	1.00E-04	1.00E-04	5.25E-05	5.00E-05	5.00E-05
Face sizing	2.00E-04	1.00E-04	7.50E-05	5.00E-05	5.00E-05	4.00E-05	3.00E-05
Smoothing	High						
Inflation Layer	1.00E-05	7.50E-06	7.50E-06	7.50E-06	7.50E-06	7.50E-06	7.50E-06
Inflation Growth Rate	1.1	1.1	1.1	1.1	1.1	1.1	1.1
Inflation Layers	5	5	5	5	5	5	5
ELEMENTS	4.80E+04	2.17E+05	4.82E+05	9.87E+05	1.67E+06	2.31E+06	4.98E+06

Resulting pressure drops and temperature gradients for the differently meshed two row fin model are shown below in Figure 4.4 with pressure and temperature plotted on the vertical axes and total element count plotted on the horizontal axis.

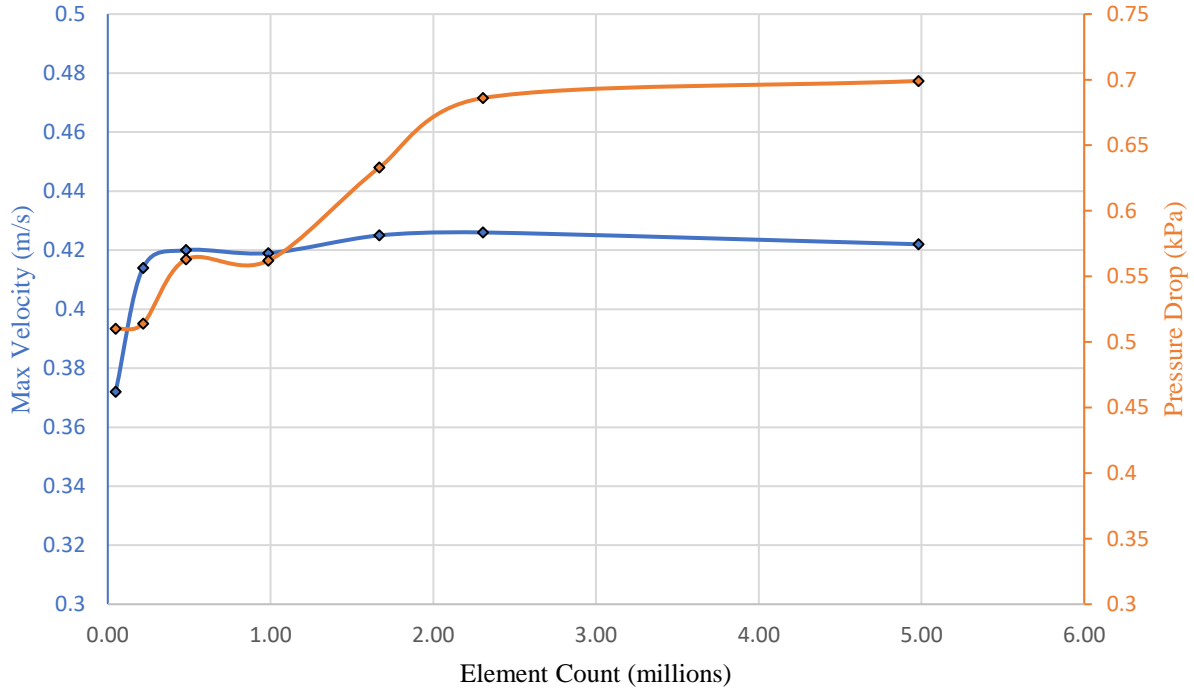


Figure 4.4: Temperature and pressure results for grid independence study on lanced offset strip fins.

Maximum velocity within the two-fin model only exhibited minor changes for meshes with more than 480,000 elements with a slight change occurring at approximately 1.5 million elements as seen in Figure 4.4 above. Total pressure drop across the finned section did show considerable change from the initial mesh with 48,000 elements to a mesh with approximately 2 million elements. However, the pressure drop across the two-fin model showed very little change for meshes with element counts equal to or greater than 2 million as seen in Figure 4.4.

Chapter 5: Results

A series of cases were simulated to better compare with the experimentally based correlations for lanced offset strip fins from Manglik and Bergles [10]. All the cases run used the dielectric fluid PAO and conductive aluminum fins. Fin geometries evaluated are shown below in Table 5.1.

Table 5.1: Fin geometries analyzed with Ansys Fluent.

Fin Height Study					
	height mm	thickness mm	length mm	Fins per cm	Fins per inch
Height A	1.27	0.1524	3.175	11.02	28
Height B	1.905	0.1524	3.175	11.02	28
Height C	2.54	0.1524	3.175	11.02	28

Fin Thickness Study					
	height mm	thickness mm	length mm	Fins per cm	Fins per inch
Thickness A	1.905	0.1016	3.175	11.02	28
Thickness B	1.905	0.1524	3.175	11.02	28
Thickness C	1.905	0.2032	3.175	11.02	28

5.1 Fin Height

Each fin height listed in Table 5.1 was analyzed for a range of PAO inlet velocities using ANSYS Fluent. Figure 5.1 shows a diagram of a lanced offset strip fins with relevant dimensions and non-dimensionalized temperature change and pressure drop parameters for the PAO.

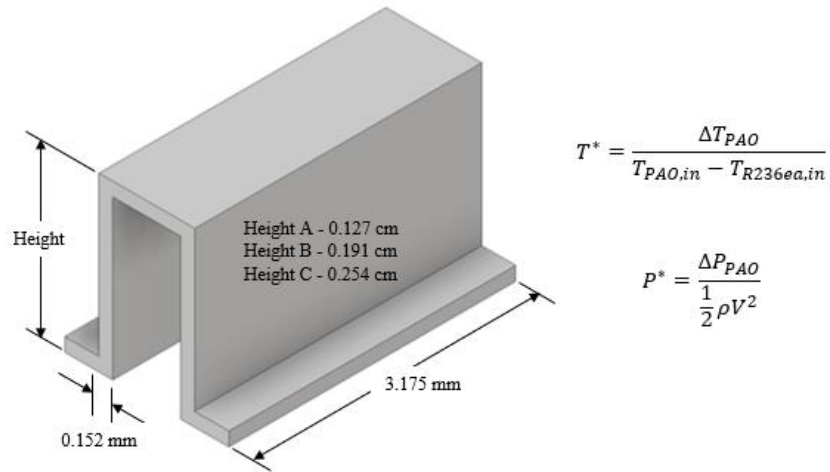


Figure 5.1: Lanced offset strip fin geometry and dimensionless temperature and pressure parameters for the fin height study.

The results can be seen in Figure 5.2 which plots dimensionless temperature change within the PAO as a function of PAO Reynolds number for the three fin heights. Dimensionless temperature and pressure definitions can be found in Figure 5.1 above.

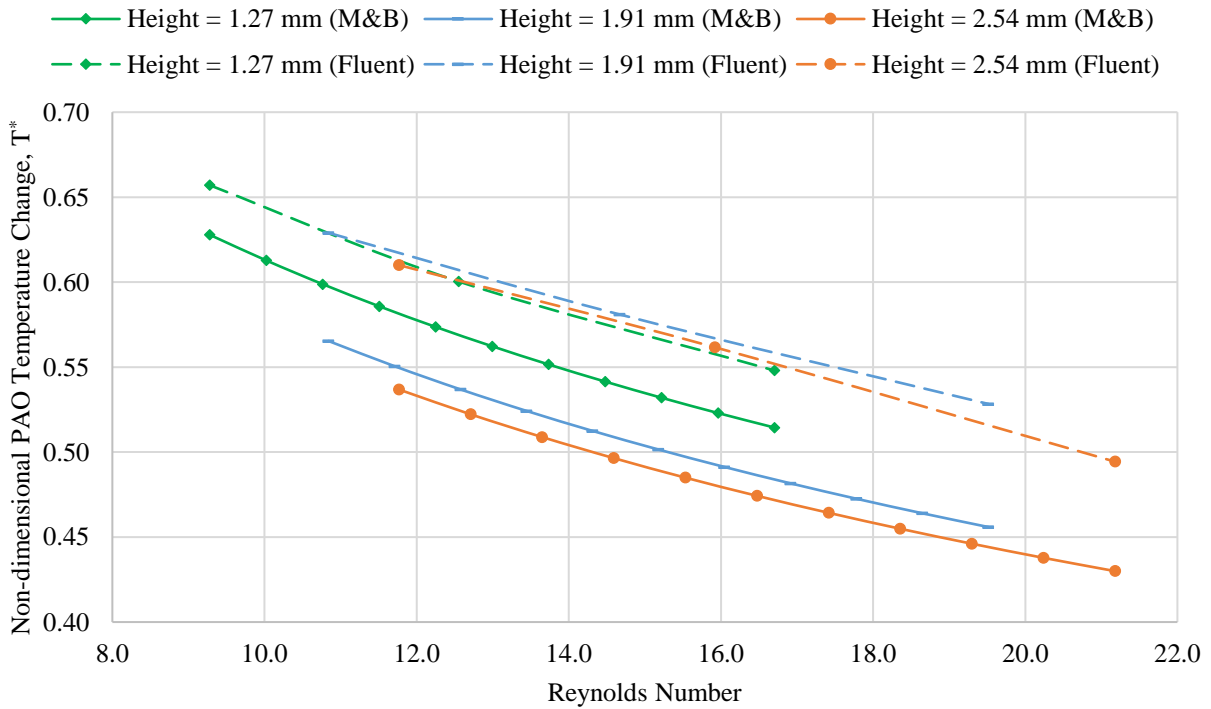


Figure 5.2: PAO temperature drop across evaporator for three fin heights as predicted by experimental correlations from Manglik and Bergles [10] and Ansys Fluent.

In order to more easily compare Fluent to the experimental correlations from Manglik and Bergles [10], the percent difference data calculated using experimental correlations deviated from Fluent data was plotted in Figure 5.3 below.

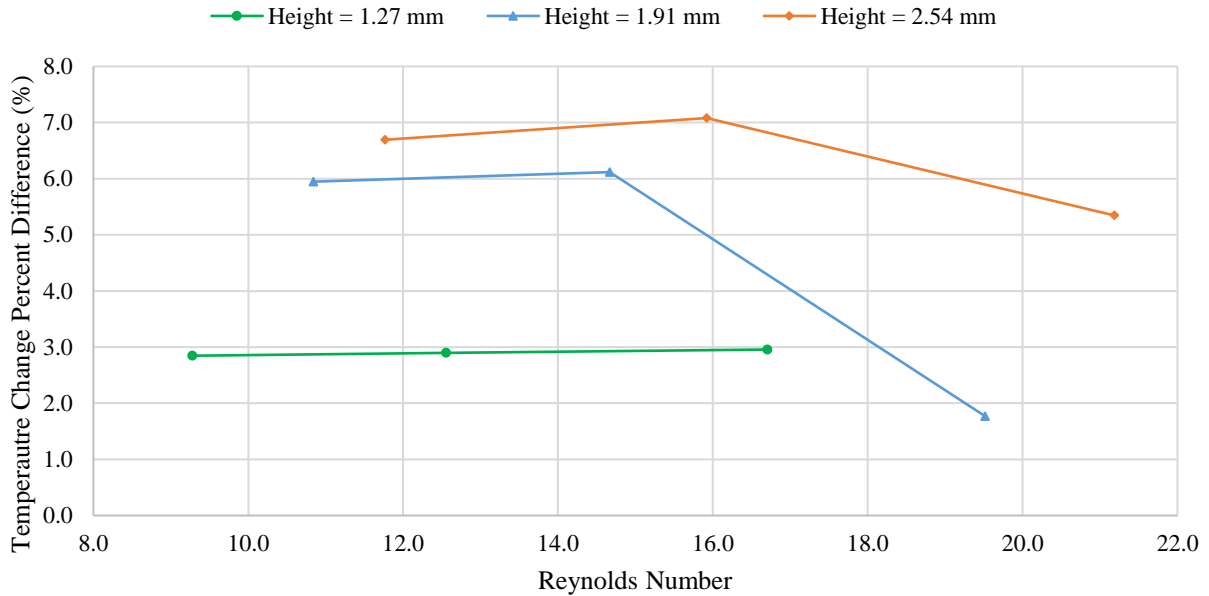


Figure 5.3: Percent difference between Manglik and Bergles [10] and Fluent’s predicted temperature drop within evaporator for various lanced offset strip fin heights.

For the shortest fins which had a height of 1.27 mm, the Fluent temperature results only showed approximately a 2.5 percent difference compared to the Manglik and Bergles [10] correlation. This difference increased for the two taller fin geometries which exhibited the largest differences at lower PAO Reynolds numbers and decreased for higher Reynolds numbers. The tallest fins with a Reynolds number of approximately 16 resulted in the highest percent difference of seven percent between the Fluent analysis and experimental correlation’s predicted PAO temperature change.

Pressure drops across the core of the evaporator were also compared for each fin height listed in Table 5.1. Figure 5.4 compares Fluent pressure results to predicted results from Manglik and Bergles [10].

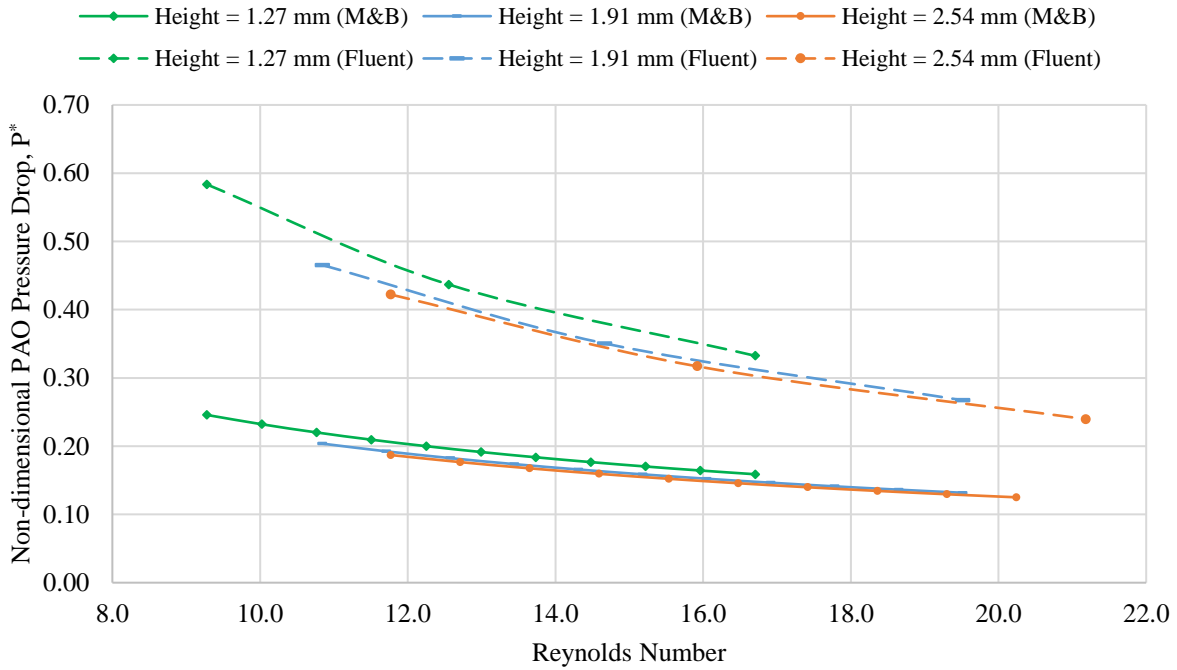


Figure 5.4: PAO pressure drop across evaporator for three fin heights as predicted by experimental correlations from Manglik and Bergles [10] and Ansys Fluent.

The percent difference between results from Fluent and results from Manglik and Bergles [10] for pressure drop across the lanced offset strip fins analyzed is shown in Figure 5.5.

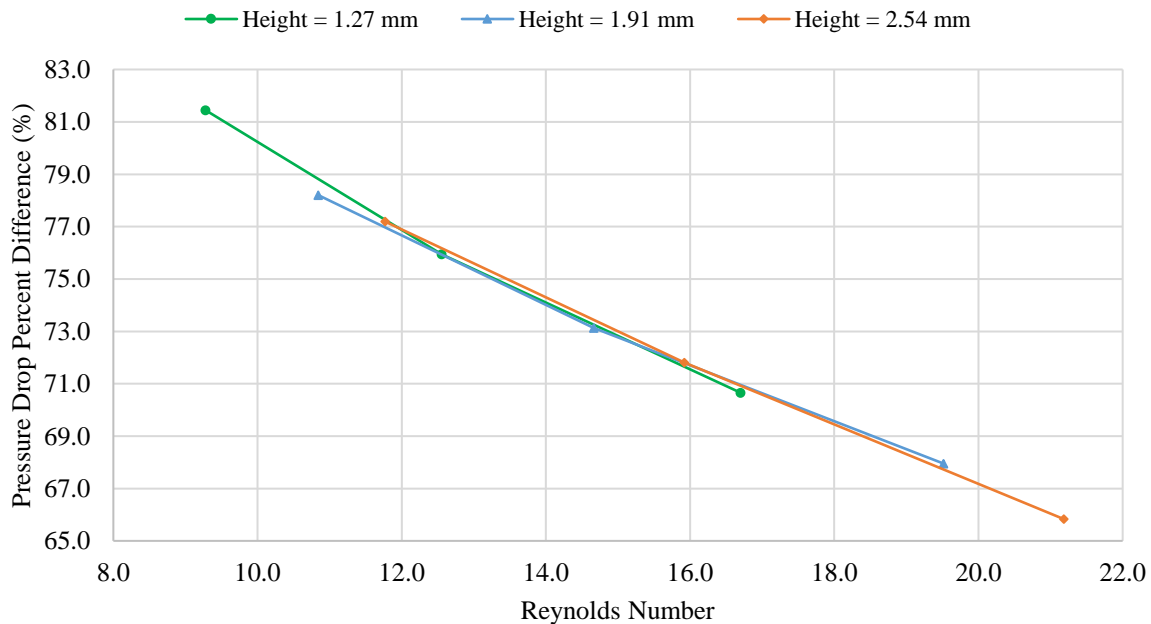


Figure 5.5: Percent difference between Manglik and Bergles [10] and Fluent's predicted pressure drop within evaporator for various lanced offset strip fin heights.

Unlike the temperature change within the PAO which showed agreement within eight percent between Fluent and experimental correlations, the pressure drop varied significantly between numerical simulations done with Fluent and predictions from Manglik and Bergles [10]. As seen in Figure 5.5, Fluent and Manglik and Bergles [10] varied by approximately 80 percent for low Reynolds numbers. This difference decreased to about 70 percent at Reynolds numbers higher than 16 with a trend downwards.

5.2 Fin Thickness

Each fin thickness listed in Table 5.1 was also analyzed for the same range of PAO inlet velocities used for the fin height study. Figure 5.6 shows a diagram of a lanced offset fin section with relevant dimensions and dimensionless temperature and pressure parameters.

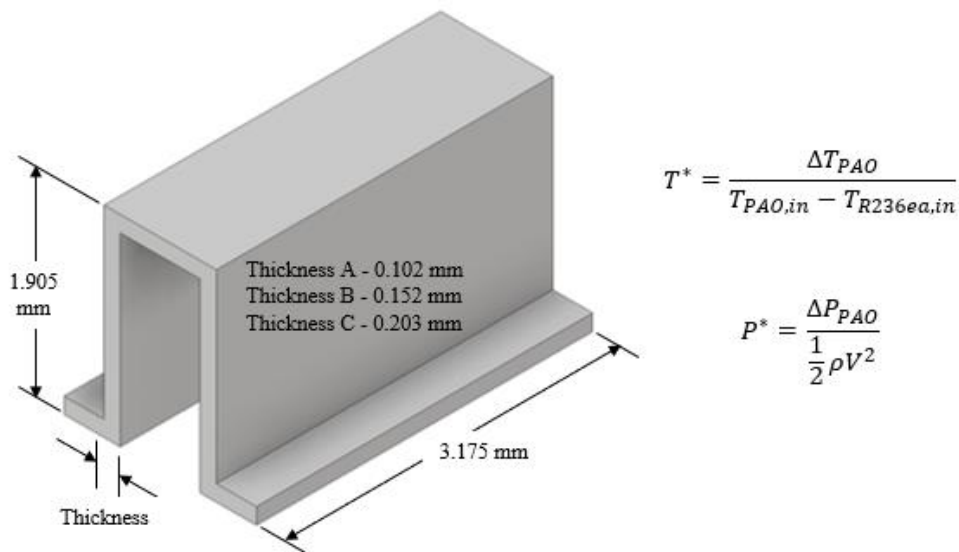


Figure 5.6: Lanced offset strip fin geometry and dimensionless temperature and pressure parameters for the fin thickness study.

PAO temperature change for each fin thickness analyzed is shown in dimensionless form below in Figure 5.7.

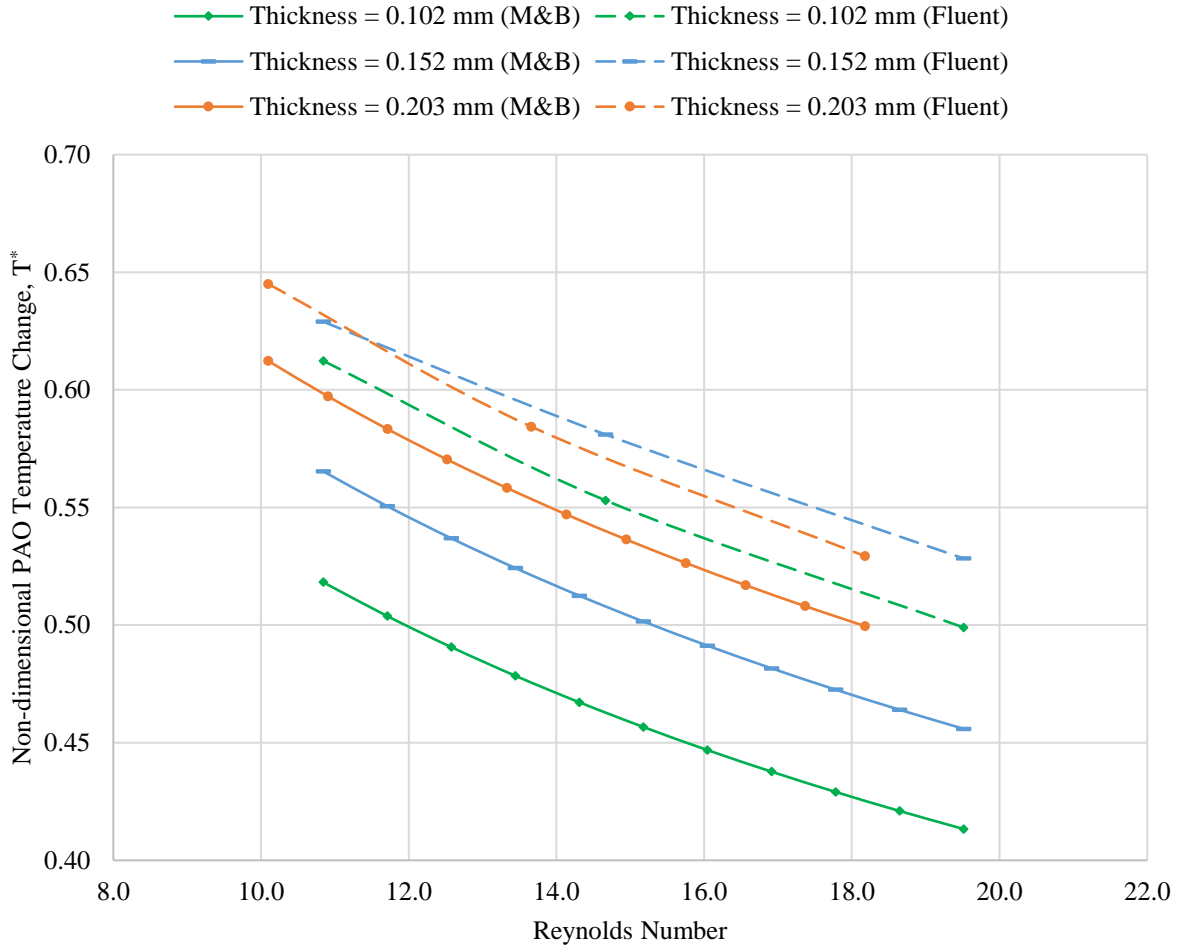


Figure 5.7: PAO temperature drop across evaporator for three fin thicknesses as predicted by experimental correlations from Manglik and Bergles[10] and Ansys Fluent.

As was done previously, the percent difference between the numerical simulation results from Fluent and Manglik and Bergles [10] were compared. The percent difference between PAO temperature drops for the fin thickness listed in Table 5.1 can be seen in Figure 5.8 below.

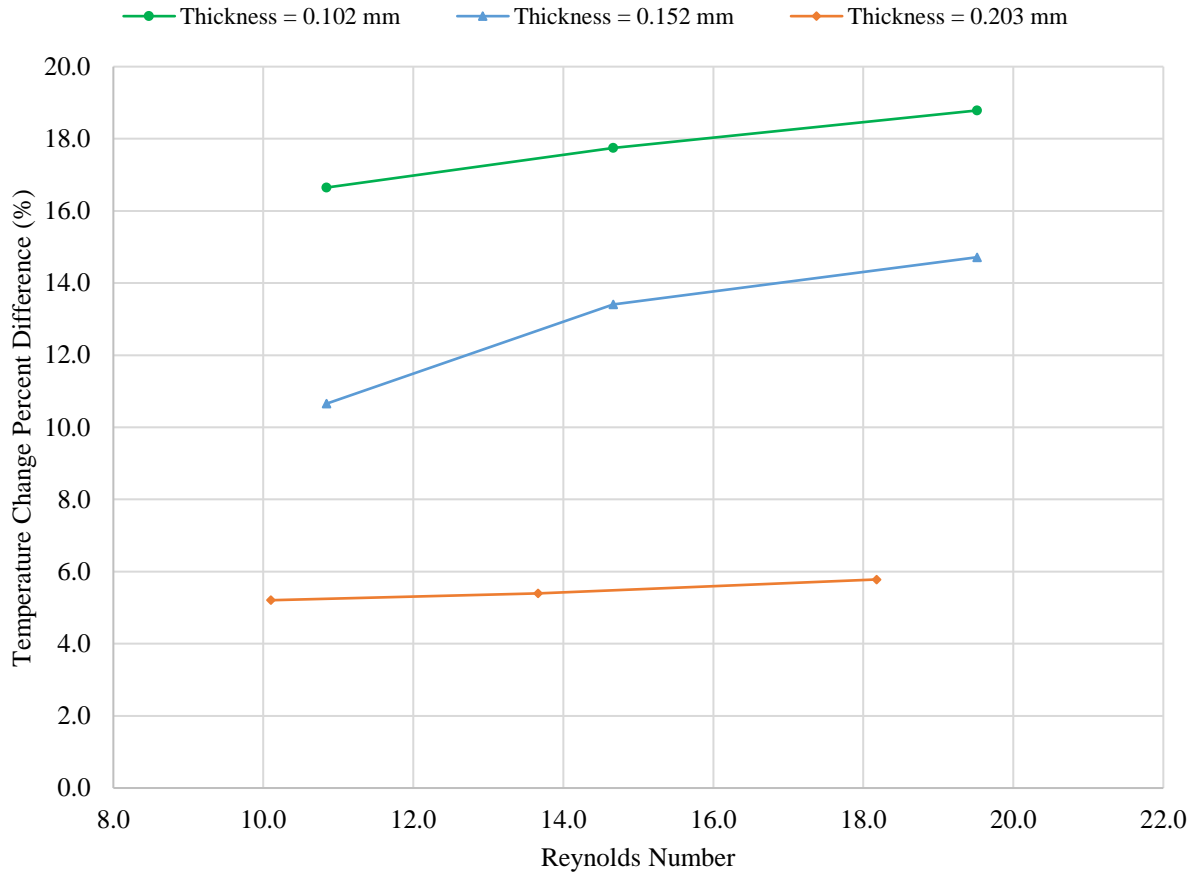


Figure 5.8: Percent difference between Manglik and Bergles [10] and Fluent’s predicted temperature drop within evaporator for various lanced offset strip fin thicknesses.

Varying fin thickness resulted in slightly larger differences between Fluent and Manglik and Bergles [10] compared to the differences which occurred when varying fin height. The thickest fins in Figure 5.6 had approximately a 5 percent difference between the two methods. The two thinner fins had noticeably more difference for lower inlet velocities with the thinnest fins resulting in a difference of 19 percent.

Pressure drops for the various fin thicknesses were also compared with the results shown in Figure 5.9 below.

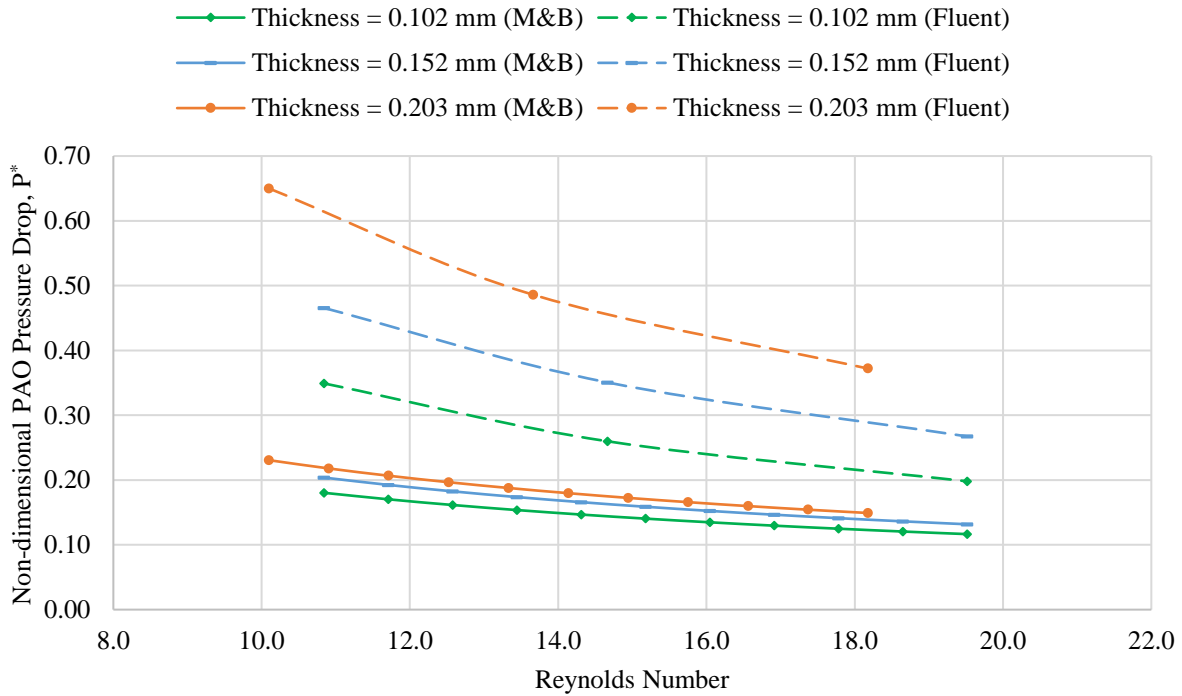


Figure 5.9: PAO pressure drop across evaporator for three fin thicknesses as predicted by experimental correlations from Manglik and Bergles [10] and Ansys Fluent.

Differences between the two methods used to calculate the pressure drop for each fin thickness are shown in Figure 5.10.

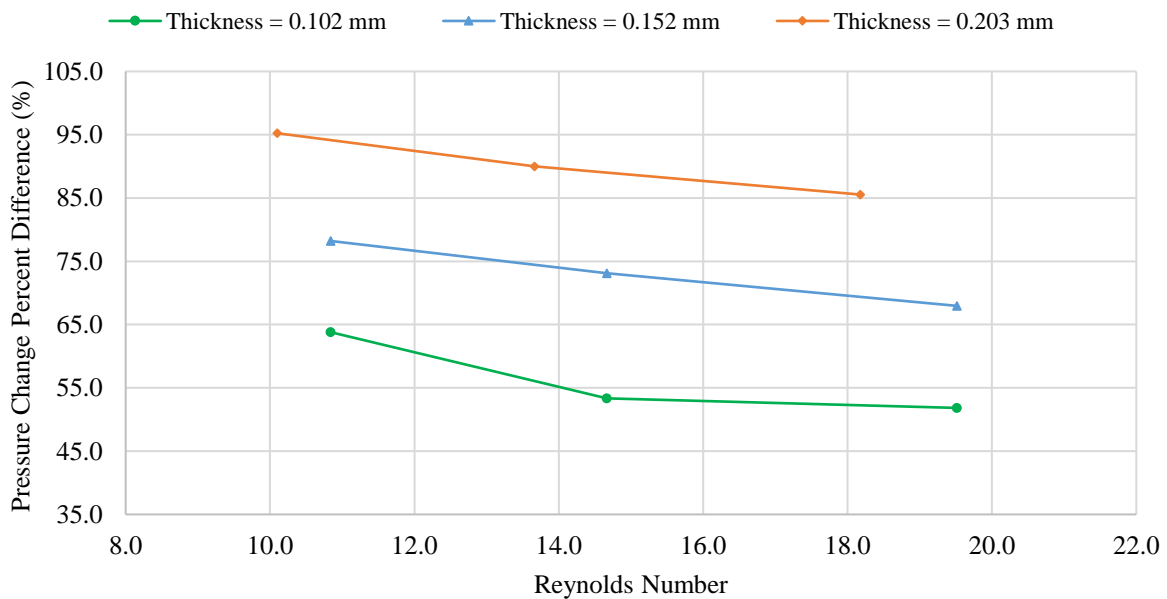


Figure 5.10: Percent difference between Manglik and Bergles [10] and Fluent’s predicted pressure drop within evaporator for various lanced offset strip fin thicknesses.

Differences between the two methods were much larger for pressure drops than for temperature drops as was the case for fin heights discussed previously. The thinnest fins had the best agreement between Fluent and Manglik and Bergles with an average difference of approximately 50 percent for Reynolds numbers ranging from 10 to 20. The thicker fins had more disagreement between the two methods with a maximum difference occurring for the 0.2032 mm thick fins at Reynolds number of 10. All three fin thicknesses showed a decreasing trend in disagreement between the two methods of calculating pressure drop as the PAO Reynolds number increased. The decreasing difference between the two methods as Reynolds number increased could be due to the fact that the low Reynolds number flow modelled in Fluent was well below the lower boundary of $Re = 120$ specified by Manglik and Bergles for their experimental correlations [10]. One additional Fluent model was run with a Reynolds number of 120 to determine if the difference between the two models decrease when in the appropriate Reynolds number range. The results are below in Table 5.2.

Table 5.2: Baseline fin geometry pressure drops for a range of Reynolds numbers.

Reynolds Number	Manglik and Bergles pressure drop	Fluent pressure drop	% difference
	Pa	Pa	
10.84	1.23	2.80	78.20
14.67	1.79	3.86	73.13
19.52	2.57	5.21	67.95
120.00	26.54	43.53	48.49

The decreasing trend of pressure difference between the two models continued to decrease as the PAO Reynolds number entered the Manglik and Bergles' acceptable range of $120 \leq Re \leq 10^4$. The difference was still significant at 49 percent but was noticeably better than the approximately 70 percent difference recorded for the designed flow parameters.

5.3 Local Heat Transfer Coefficients

Local fin heat transfer coefficients were calculated down the length of the finned section by analyzing fin wall temperature, fin wall heat flux, and bulk fluid temperature at the middle of each fin analyzed.

$$h = \frac{q''}{T_{bulk} - T_{wall}} \quad (25)$$

$$T_{bulk} = \int_{Ax} u(x, y) T(x, y) dAc / \dot{m} \quad (26)$$

Where T_{bulk} is the mass-average fluid temperature, T_{wall} is the average vertical fin wall temperature, and q'' is the average heat flux for each vertical fin wall analyzed. Heat transfer coefficients were only found for every other fin row due to the repeating geometry as shown in Figure 5.11. The last fin, number 14, was also analyzed but comparisons to the other fins must account for the change in geometry and fin wall location.

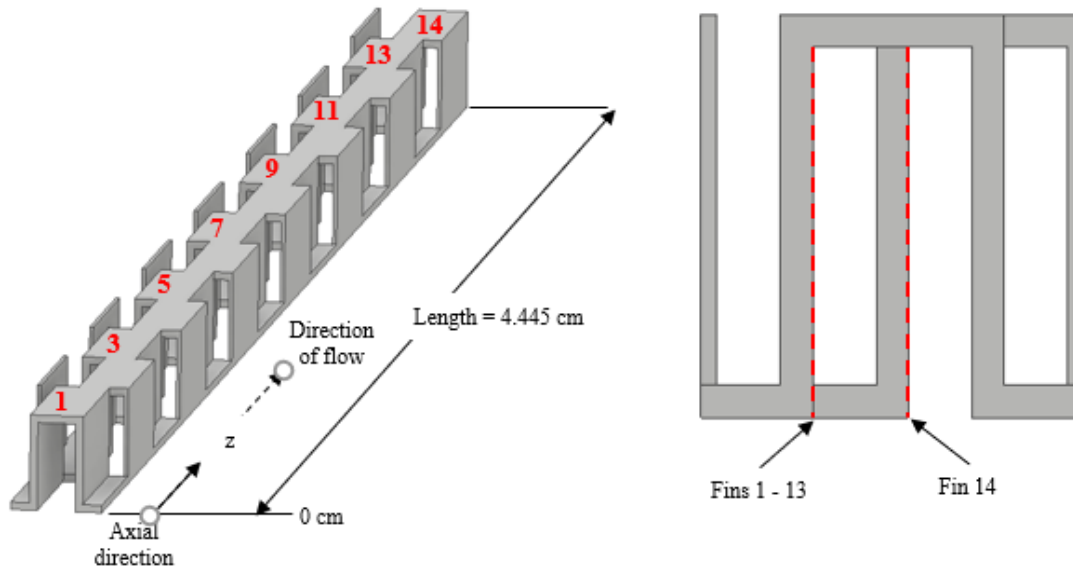


Figure 5.11: Locations where local heat transfer coefficients were calculated.

Note that due to the staggered fin geometry, the two vertical fin walls compared for fins 1 – 13 and fin 14 are not in the exact same position horizontally. The last fin's wall is shifted slightly to the right when looking at a cross-section view of the fins as shown in Figure 5.10.

Local heat transfer coefficients were calculated for the baseline fin geometry and plotted as a function of inverse Graetz number, Gr^{-1} , for three different PAO inlet velocities and plotted in Figure 5.12.

$$Gz^{-1} = \frac{z}{d_h Re Pr} \quad (27)$$

$$d_h = \frac{4c(b-t)l}{2(cl + (b-t)l + t(b-t)) + tc} \quad (25)$$

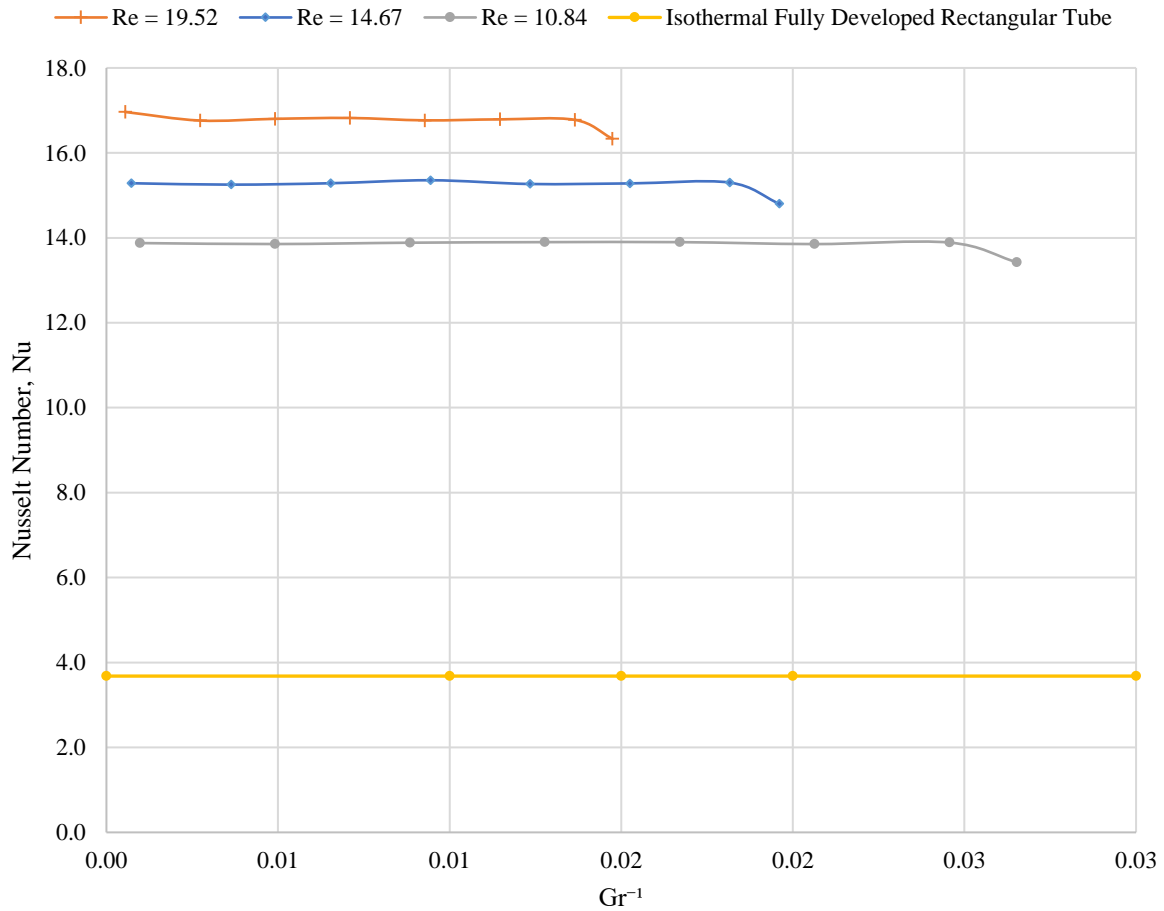


Figure 5.12: Nusselt numbers as a function of inverse Graetz number for three PAO inlet velocities compared to Nusselt number for isothermal rectangular tube with same aspect ratio presented by Incropera [22].

All three inlet conditions resulted in near-constant Nusselt numbers down the length of the heat exchanger. Row 14 at the end of the fin array consistently resulted in lower Nusselt numbers than the previous 13 rows. This could be due to exit effects since row 14 was the last

row of fins and the PAO flowed out of them into the exit plenum. The constant behavior of the Nusselt numbers calculated from Fluent data agrees well with literature which holds that fully developed flow results in constant Nusselt numbers. Incropera et al. [22] discuss this phenomenon in chapter eight of *Fundamentals of Heat and Mass Transfer* (pages 486-532).

Nusselt numbers were also calculated down the length of the fin array for a range of fin thicknesses and fin heights. Figure 5.13 plots Nusselt numbers as a function of fin array length for three different fin heights and Figure 5.14 plots Nusselt numbers as a function of fin array length for three different fin thicknesses.

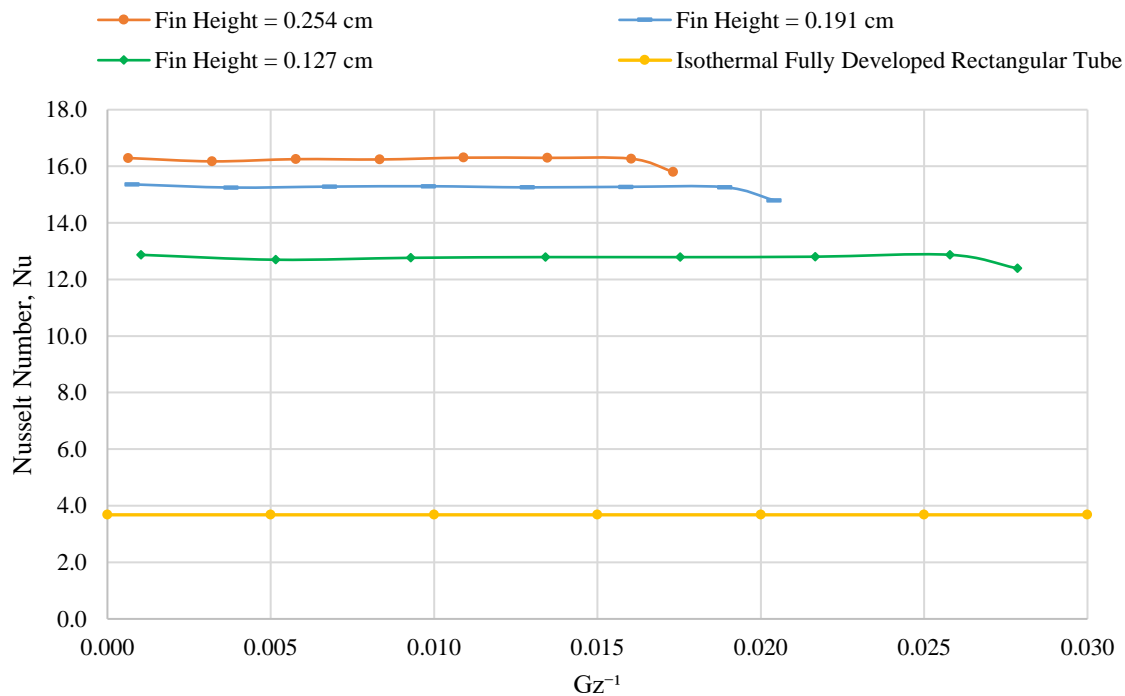


Figure 5.13: Nusselt numbers as a function of inverse Graetz number for three fin heights and a Reynolds number of 14.67 compared to Nusselt number for isothermal rectangular tube with aspect ratio of 2.5 presented by Incropera [22].

Nusselt numbers remained nearly constant down the length of the fin array but decreased in value as the fin height was decreased. The most significant drop in Nusselt number value

occurred between fin heights of 0.191 cm and 0.127 cm with a smaller drop occurring when fin height changed from 0.254 cm to 0.191 cm.

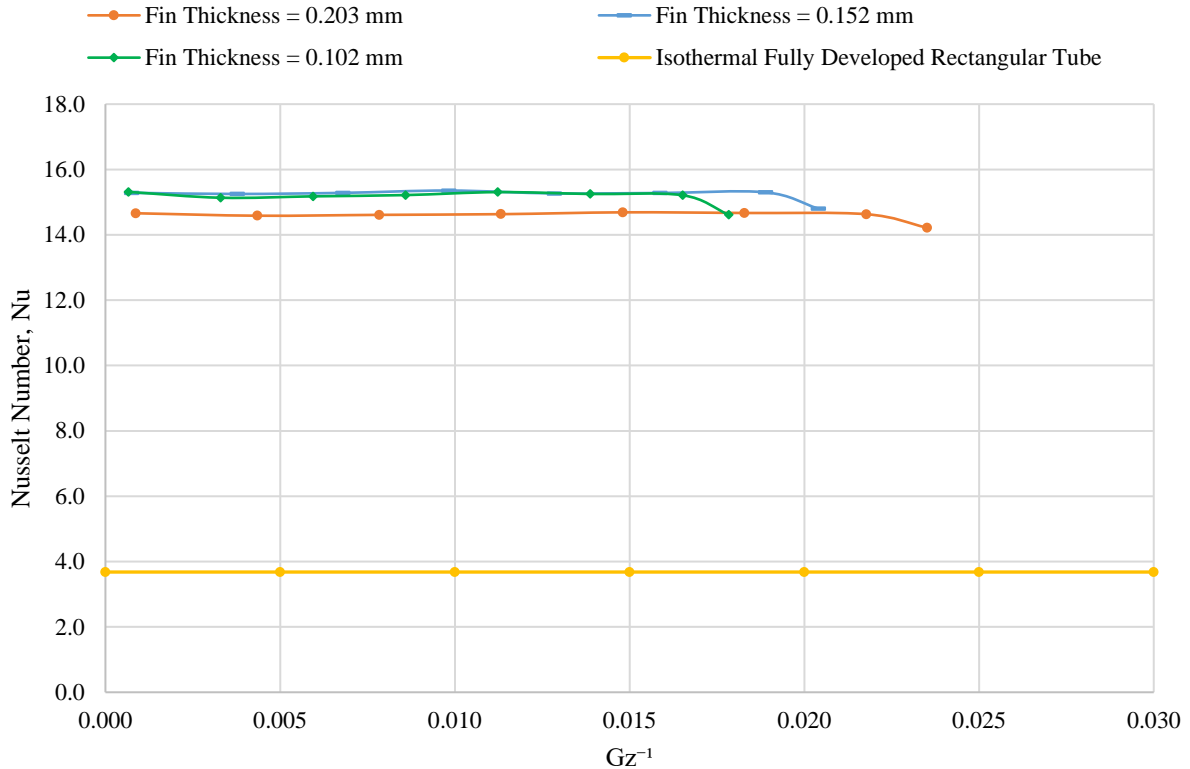


Figure 5.14: Nusselt numbers as a function of inverse Graetz number for three fin thicknesses and an inlet velocity of 0.1691 m/s compared to Nusselt number for isothermal rectangular tube with aspect ratio of 2.5 presented by Incropera [22].

Nusselt numbers showed very little change when decreasing fin thickness from 0.203 mm to 0.102 mm. Both fin thicknesses of 0.152 mm and 0.102 mm resulted in very similar Nusselt numbers. A fin thickness of 0.203 mm resulted in Nusselt numbers slightly less than the two thinner fins analyzed.

A more detailed local heat transfer analysis was also done on the fins by analyzing local heat transfer coefficients down the length of a single fin instead of the entire fin array. Heat flux, wall temperature, and bulk fluid temperature were evaluated at five different locations down the length of the fin. Conduction through the fin walls was included in the Fluent model. An

example is shown in Figure 5.15 which shows these locations on the first fin row of the baseline fin geometry and inlet conditions.

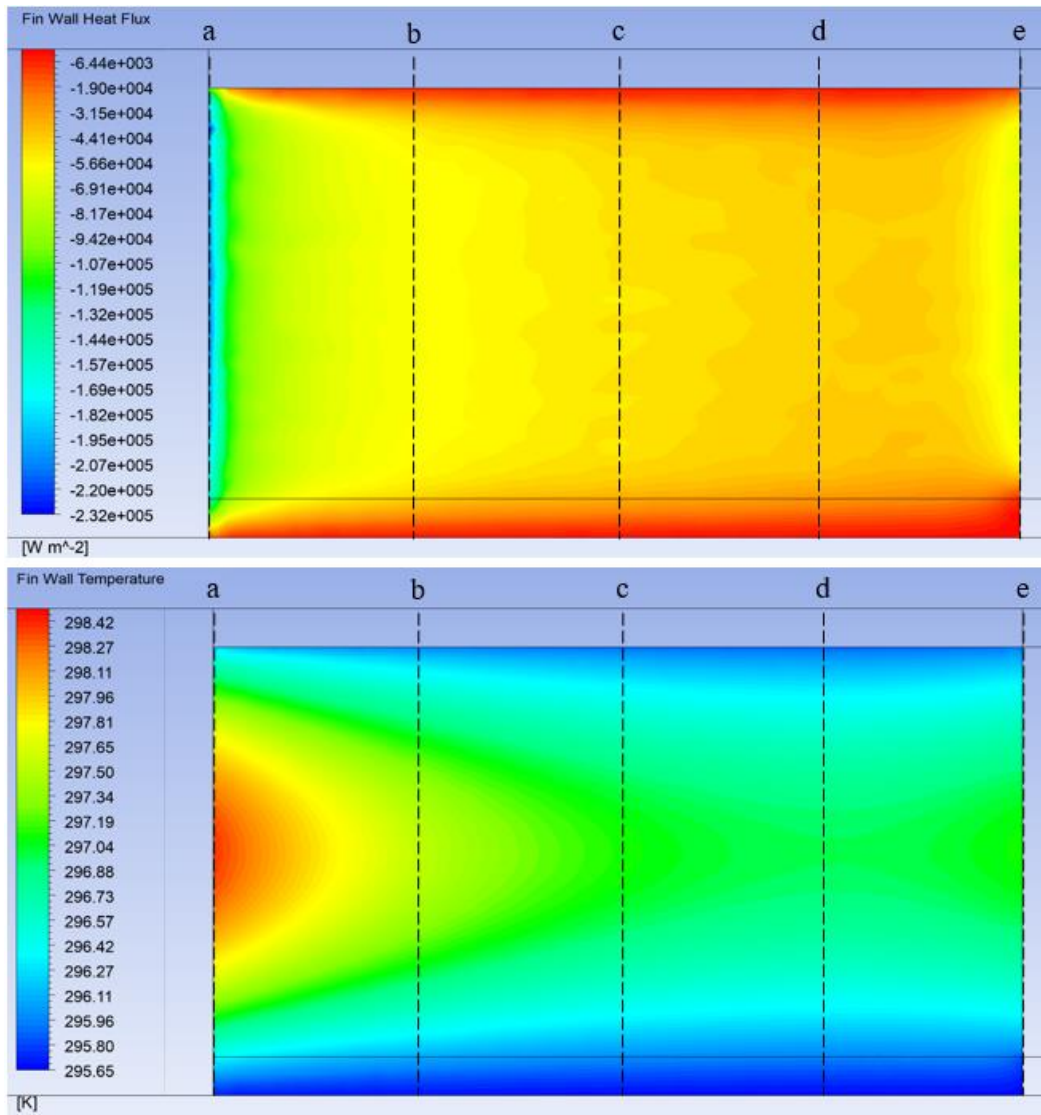


Figure 5.15: Fin wall locations evaluated with position a at the leading edge and position e at the trailing edge for fin 1 wall heat flux (top) and fin 1 wall temperature (bottom).

Analysis was done for the same range of inlet velocities, fin heights, and fin thicknesses considered for local heat transfer down the length of the fin array. Figure 5.16 plots Nusselt numbers as a function of inverse Graetz number for Reynolds numbers ranging from 10.84 to 19.52 for the first fin row.

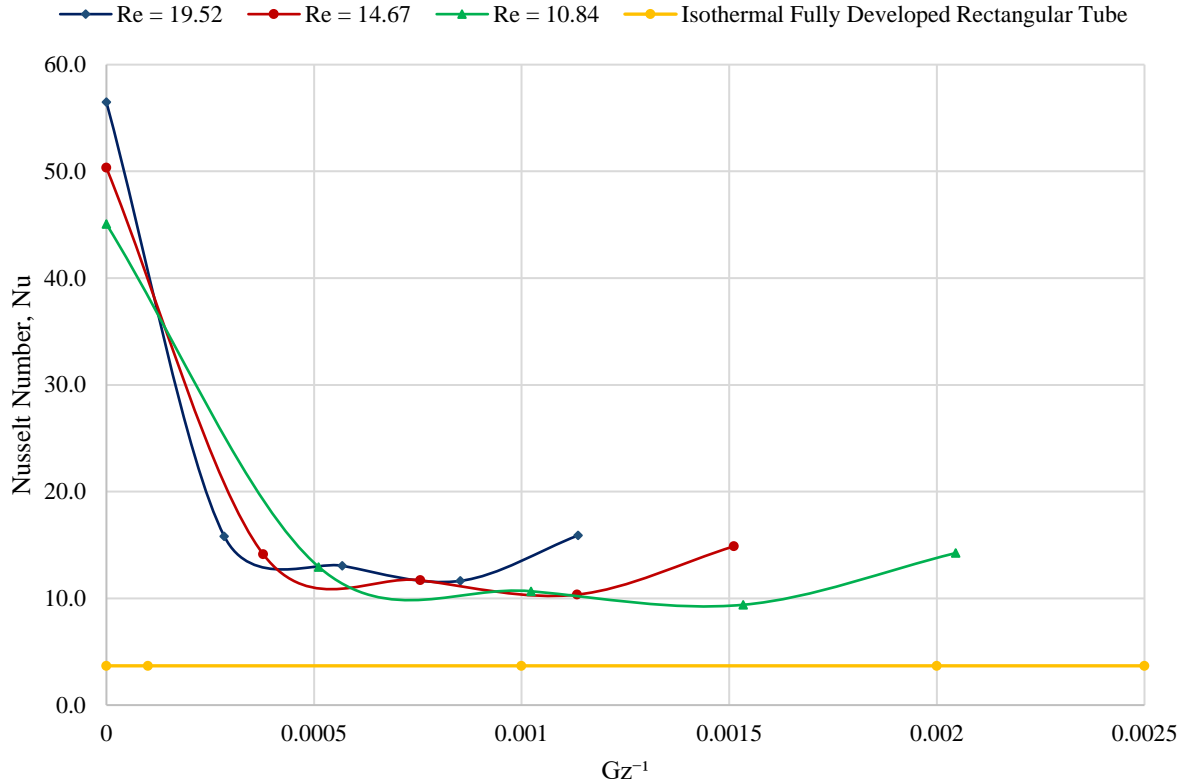


Figure 5.16: Fin 1 Nusselt numbers as a function of inverse Graetz number for three different PAO inlet velocities compared to Nusselt number for isothermal rectangular tube with aspect ratio of 2.5 presented by Incropera [22].

Nusselt numbers were highest at the leading edge of the fin where the thermal boundary layer began developing. As the boundary layer developed the Nusselt numbers decreased, eventually flattening out to a near-constant value at approximately the middle of the fin. This behavior helps explain the constant Nusselt number behavior seen previously in Figures 5.11, 5.12, and 5.13. Results from Figure 5.16 for the baseline Reynolds number of 14.67 were compared to solutions done by Kays and Crawford for circular ducts with fixed wall temperature taken from Incropera’s book *Fundamentals of Heat and Mass Transfer* [22]. This comparison is shown in Figure 5.17.

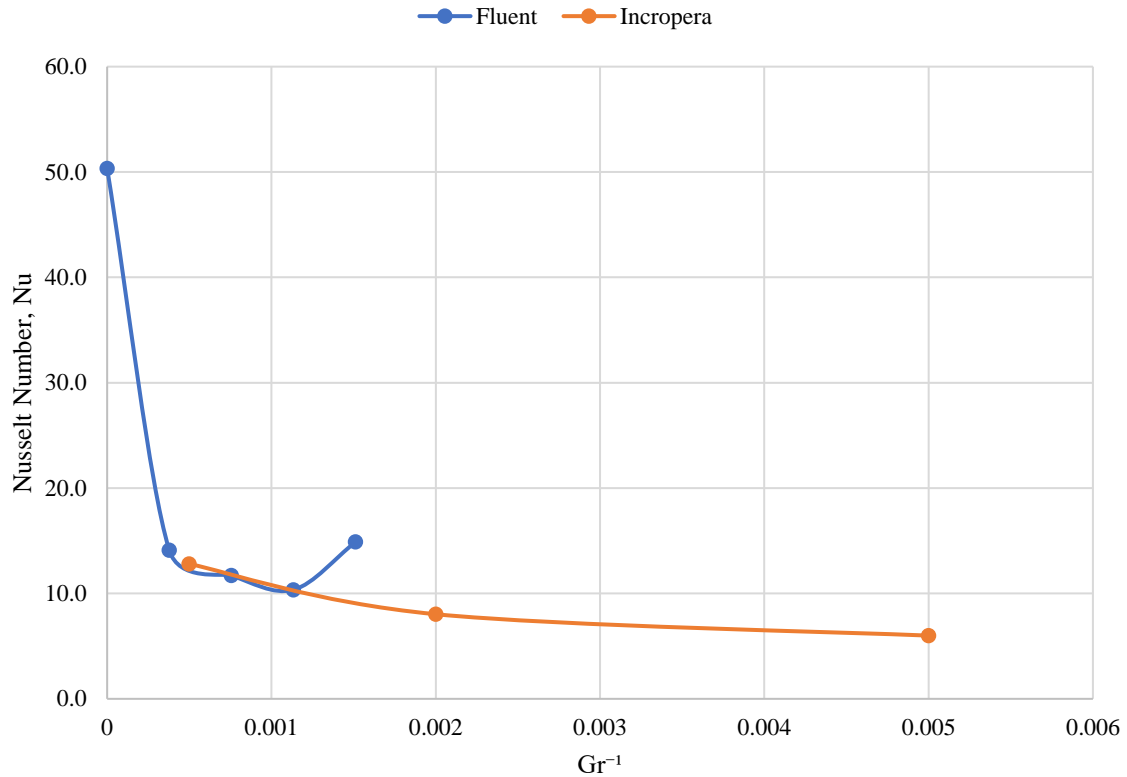


Figure 5.17: Comparison between Nusselt numbers found using Fluent for the lanced offset strip fins and solution for constant wall temperature circular duct discussed by Incropera [21].

Incropera notes that the Nusselt numbers for the constant wall temperature circular duct approach infinity at the leading edge. Nusselt numbers calculated from Fluent data for the lanced offset strip fin exhibit similar values as the circular duct discussed by Incropera with both resulting in Nusselt numbers between 15 and 10 for inverse Graetz numbers between 0.0005 and 0.001.

Nusselt numbers for the first and next-to-last row of fins were also calculated and compared for the baseline geometry and a Reynolds number of 14.67. The results are shown below in Figure 5.18.

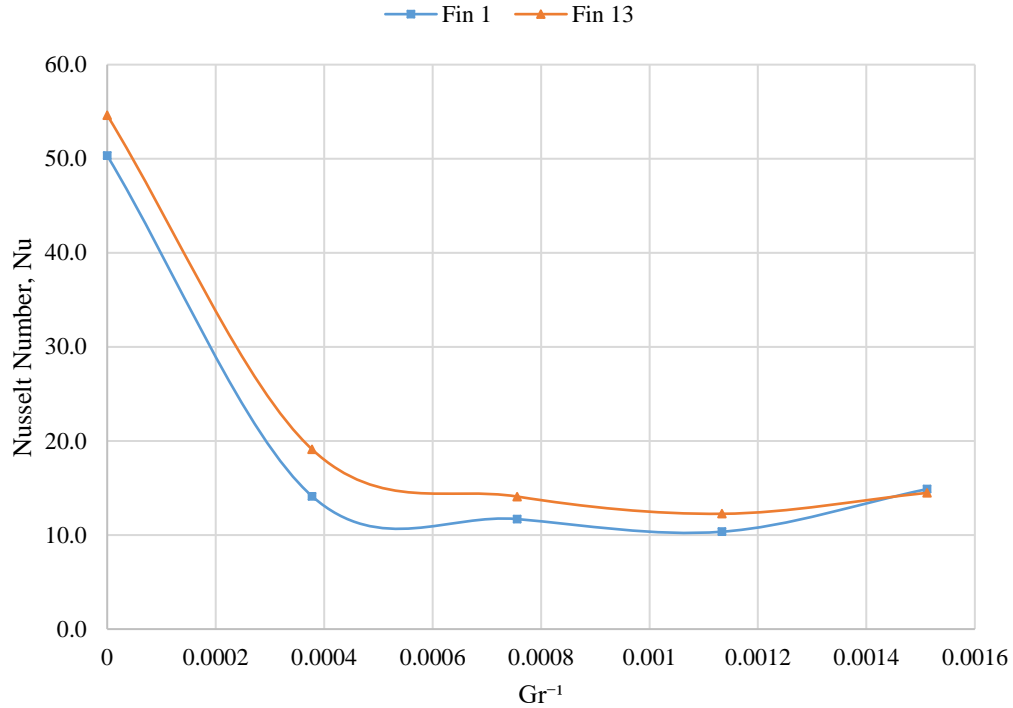


Figure 5.18: Nusselt numbers as a function of inverse Graetz number for the first and thirteenth fin rows for the baseline fin geometry and flow conditions.

The first and thirteenth fin rows had extremely similar Nusselt number behavior down the length of each fin. As previously discussed, this agreement results from the PAO flow being fully developed.

Nusselt numbers as a function of fin length were also calculated for varying fin heights and fin thicknesses. Only the first fin row was analyzed due to the high level of agreement between the individual fin rows resulted from the fully developed PAO flow. Figures 5.19 and 5.20 show Nusselt numbers as a function of fin length for varying fin heights and thicknesses respectively.

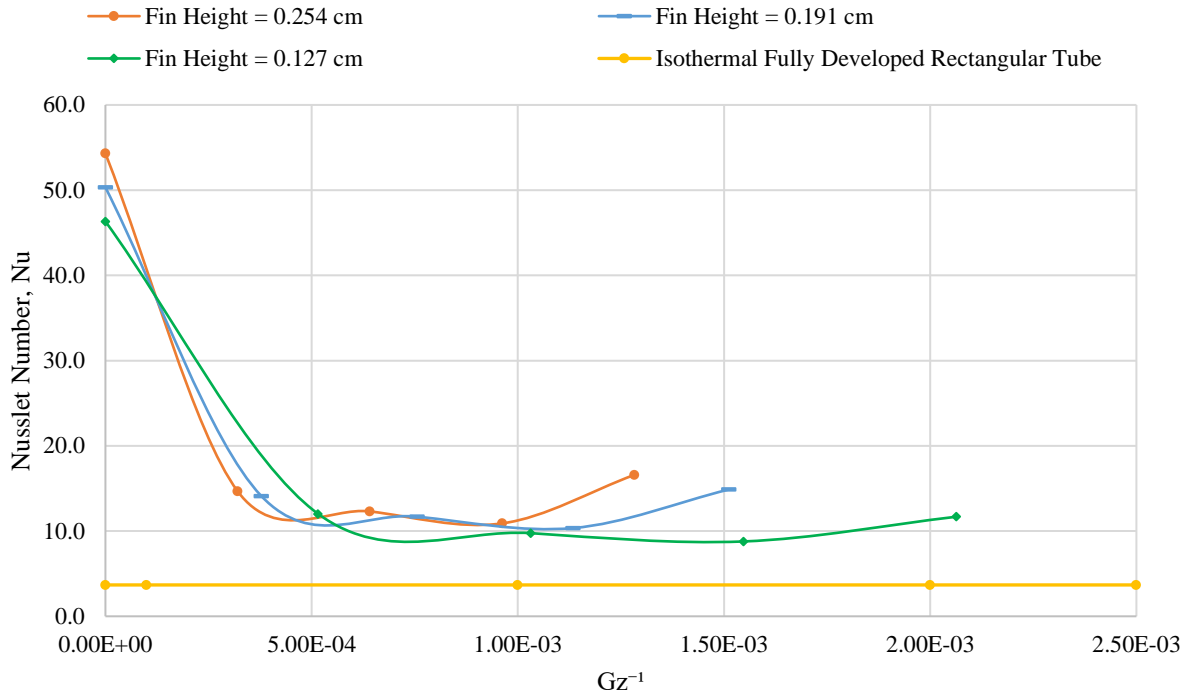


Figure 5.19: Fin 1 Nusselt numbers as a function of inverse Graetz number for three different fin heights and an inlet velocity of 0.1691 m/s compared to Nusselt number for isothermal rectangular tube with aspect ratio of 2.5 presented by Incropera [22].

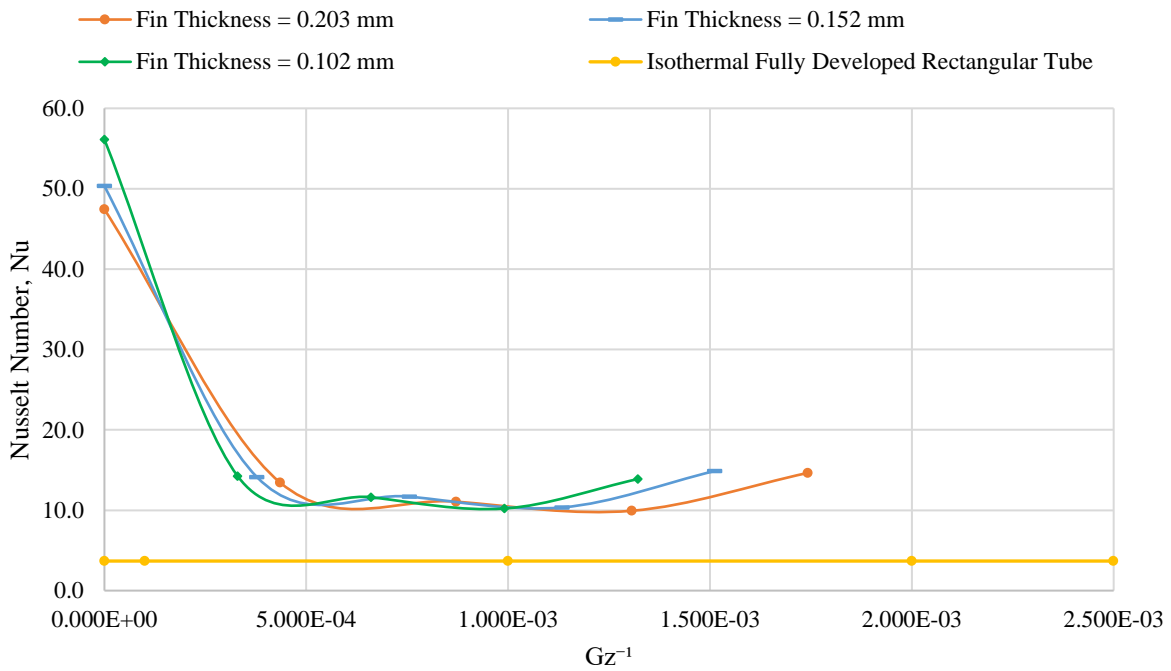


Figure 5.20: Fin 1 Nusselt numbers as a function of inverse Graetz number for three different fin thicknesses and an inlet velocity of 0.1691 m/s compared to Nusselt number for isothermal rectangular tube with aspect ratio of 2.5 presented by Incropera [22].

An overall effective heat transfer coefficient was also calculated for the baseline Fluent model using inlet and outlet bulk fluid temperatures and fluid properties. The average heat transfer coefficient was found using the Log Mean Temperature Difference (LMTD) defined below.

$$\Delta T_{LMTD} = \frac{(T_{bulk\ out,PAO} - T_{R236ea}) - (T_{bulk\ in,PAO} - T_{R236ea})}{\ln\left(\frac{(T_{bulk\ out,PAO} - T_{R236ea})}{(T_{bulk\ in,PAO} - T_{R236ea})}\right)} \quad (26)$$

Combining the equation above with a first law analysis results in an equation for the effective overall heat transfer coefficient in terms of fluid mass flow rate \dot{m}_{PAO} , fluid specific heat $C_{p,PAO}$, heat transfer area A, and fluid temperatures.

$$\bar{h} = \frac{\dot{m}_{PAO} C_{p,PAO} (T_{bulk\ out,PAO} - T_{bulk\ in,PAO})}{A \Delta T_{LMTD}} \quad (27)$$

The resulting average heat transfer coefficient for the Fluent model was $\bar{h}_{Fluent} = 1.03 \frac{kW}{m^2K}$.

This differed by 21 percent from the heat transfer coefficient predicted using the experimental correlations from Manglik and Bergles [10] which resulted in $\bar{h}_{Manglik\ and\ Bergles} = 1.27 \frac{kW}{m^2K}$.

5.4 Velocity Fields and Flow Behavior

Velocity plots of the PAO flow through the lanced offset strip fins were created to better understand flow behavior and to identify any vortices generated at the trailing edge of the fins. Figure 5.21 below shows several velocity plots of the PAO flow taken at the middle of the fin array.

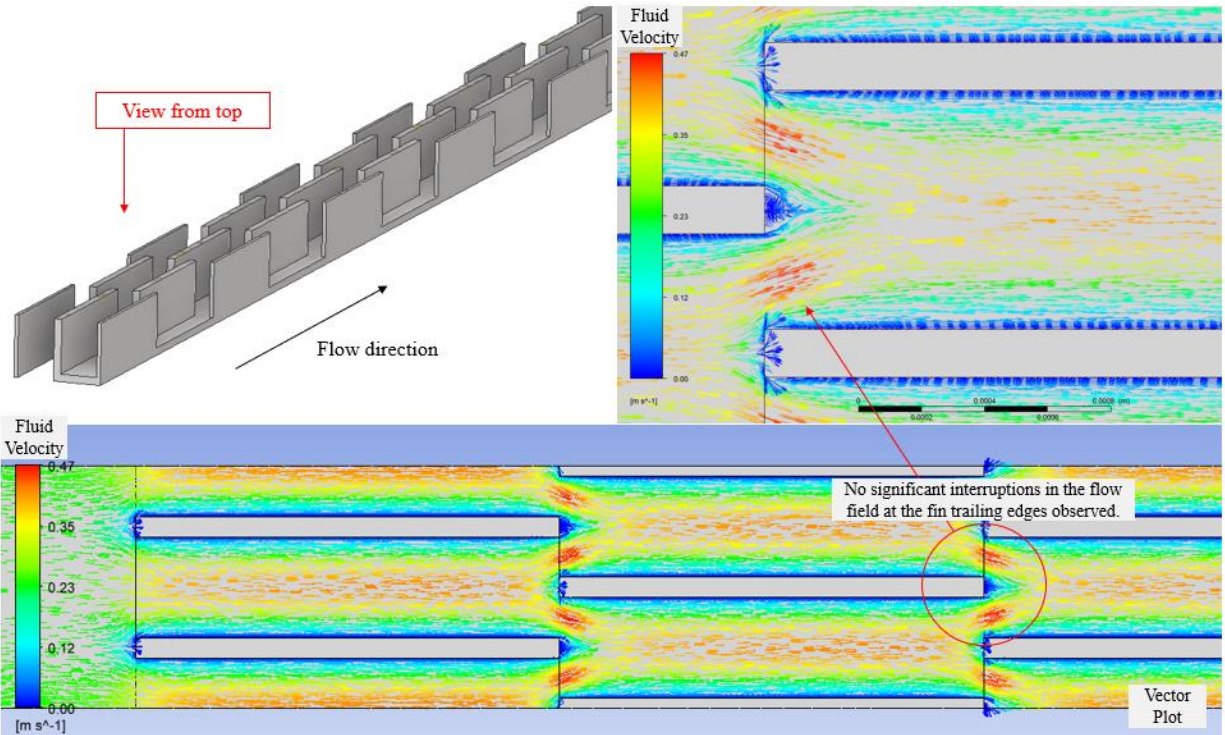


Figure 21 Vector velocity plots of the PAO flowing through baseline geometry lanced offset strip fins at $Re = 14.67$.

Due to the low Reynolds number flow, vortices at the trailing edge of the fins did not interrupt the flow or cause unpredictable and unstable flow behavior often observed for turbulent flow.

Velocity plots for each fin row were very comparable showing increased velocities occurring at row transitions which then resolved into central streams through the fin channels.

Chapter 6: Conclusions

Thermal performance of PAO flow through lanced offset strip fins with various heights and thicknesses as predicted by Manglik and Bergles [10] was reasonably close to numerical simulations done with Ansys Fluent. Sensitivity studies on fin height showed both methods predicting the thermal performance of the fins to within eight percent of each other. Fin thickness, which has a greater impact on the heat transfer coefficient of the PAO, resulted in slightly higher differences between experimental correlations and numerical simulations with a maximum difference of 16 percent. Increased Reynolds numbers resulted in better agreement between the two methods for both the fin height and fin thickness sensitivity studies. This trend seems reasonable since Manglik and Bergles correlations were based on Reynolds numbers at or greater than 120 and the PAO flow analyzed only had Reynolds number of 10 – 20.

Differences in pressure drop across the heat exchanger core were much more significant than temperature drops across the heat exchanger core for both methods. Varying fin height resulted in the two methods disagreeing on predicted pressure drop by approximately 55 percent. This increased to a difference of 40 – 65 percent when fin thickness was varied. For both fin geometries varied, the two methods did show increased agreement for higher Reynolds numbers.

While the thermal performance of the heat exchanger may be reasonably modelled using experimental correlations of Manglik and Bergles, there appears to be substantial disagreement when predicting pressure drops within lanced offset strip fins. This difference could be because the experimental correlations used were intended for much higher Reynolds numbers than the ones evaluated in this project. PAO's high Prandtl number of 144 may also be problematic since

Manglik and Bergles [10] only specified application of their correlations for a moderate range of Prandtl numbers from 0.5 – 15. However, there is no clear connection or easily discernable reason for why agreement would exist between the two methods for thermal performance and not pressure drop. More experimental data for dielectric fluids such as PAO at extremely low Reynolds number flows is needed in order to fully understand and confidently predict flow through lanced offset strip fins.

A study of local fin heat transfer clearly demonstrated that thermally fully developed conditions prevailed resulting in near-constant heat transfer coefficients occurring at each row of fins. Thermally fully developed flow occurred at approximately the middle of each fin with the most significant heat transfer coefficient change happening from the leading edge to the middle of the fin. For the flow conditions analyzed in this project, each fin could be shortened up to 50% to better capitalize on the thermal boundary layer interruption occurring due to the lanced offset fin array design. The corresponding pressure drop increases and manufacturability of such adjustments would have to be considered in future designs.

Future work on this project or related topics associated with PAO and lanced offset strip fins would benefit greatly from experimental data. Data for low Reynolds number flows, particularly dielectric oils, would be particularly beneficial for the field of electronics cooling. Initially the evaporator designed for this project was going to be fabricated and experimental data for it was going to be collected to verify the correlations and design used for this project. However, due to difficulties fabricating the evaporator in a timely manner, the experimental portion of this project was impossible to continue. A more detailed discussion on the proposed experimental setup and equipment can be found in Appendix A.

Chapter 7: References

- [1] S. Trutassanawin, E. A. Groll, S. V. Garimella, and L. Cremaschi, “Experimental investigation of a miniature-scale refrigeration system for electronics cooling,” *IEEE Trans. Components Packag. Technol.*, vol. 29, no. 3, pp. 678–687, 2006.
- [2] P. E. Phelan, V. A. Chiriac, and T. Y. Tom Lee, “Current and future miniature refrigeration cooling technologies for high power microelectronics,” *IEEE Trans. Components Packag. Technol.*, vol. 25, no. 3, pp. 356–365, 2002.
- [3] Z. Wu and R. Du, “Design and experimental study of a miniature vapor compression refrigeration system for electronics cooling,” *Appl. Therm. Eng.*, vol. 31, no. 2–3, pp. 385–390, 2011.
- [4] N. S. Ashraf *et al.*, “Design and Analysis of a Meso-Scale Refrigerator,” no. 407, pp. 1–8.
- [5] J. R. Barbosa, G. B. Ribeiro, and P. A. De Oliveira, “A state-of-the-art review of compact vapor compression refrigeration systems and their applications,” *Heat Transf. Eng.*, vol. 33, no. 4–5, pp. 356–374, 2012.
- [6] J. DEWATWAL, “Design of Compact Plate Fin Heat Exchanger,” *Natl. Inst. Technol. Rourkela*, 2009.
- [7] O. A. Huzayyin, R. M. Manglik, and M. A. Jog, “Extended Results for Fully Developed Laminar Forced Convection Heat Transfer in Trapezoidal Channels of Plate-Fin Exchangers,” *J. Therm. Sci. Eng. Appl.*, vol. 2, no. 4, p. 044501, 2011.
- [8] A. L. Shah, R K; London, “Offset Rectangular Plate-Fin Surfaces — Heat Transfer and Flow Friction Characteristics,” 2019.

- [9] R. Sadasivam, R. M. Manglik, and M. A. Jog, "Fully developed forced convection through trapezoidal and hexagonal ducts," vol. 42, pp. 4321–4331, 1999.
- [10] R. M. Bergles and A. E. Manglik, "Heat transfer and pressure drop correlations for the rectangular offset strip fin compact heat exchanger," *Exp. Therm. Fluid Sci.*, vol. 10, no. 2, pp. 171–180, 1995.
- [11] K. Guo, "Optimisation of Plate/Plate-Fin Heat Exchanger Design," 2015.
- [12] M. Amaranatha Raju, T. P. Ashok Babu, and C. Ranganayakulu, "Flow boiling heat transfer and pressure drop analysis of R134a in a brazed heat exchanger with offset strip fins," *Heat Mass Transf. und Stoffuebertragung*, vol. 53, no. 10, pp. 3167–3180, 2017.
- [13] R. C. Lockhart, R W; Martinelli, "Proposed Correlation of Data for Isothermal Two-Phase, Two-Component Flow in Pipes," *Chem. Eng. Prog.*, vol. 45, no. 1, 1949.
- [14] B. Kim and B. Sohn, "An experimental study of flow boiling in a rectangular channel with offset strip fins," *Int. J. Heat Fluid Flow*, vol. 27, no. 3, pp. 514–521, 2006.
- [15] G. D. Mandrusiak, "Pressure Drop Characteristics of Two-Phase Flow in a Vertical Channel with Offset Strip Fins," pp. 41–50, 1988.
- [16] V. P. Carey, *Liquid-Vapor Phase-Change Phenomena*, 2nd ed. New York: Taylor and Francis Group, LLC, 2008.
- [17] J. C. Chen, "A Correlation for Boiling Heat Transfer to Saturated Fluids in Convective Flow," 1962.
- [18] Y. Fujita, "Nucleate boiling heat transfer and critical heat flux in narrow space between rectangular surfaces," vol. 31, no. 2, 1988.
- [19] D. L. Bennett, M. W. Davis, and B. L. Hertzeler, "Suppression of Saturated Nucleate Boiling by Forced Convective Flow," *AIChE Symp. Ser.*, vol. 76, 1980.

- [20] S. Version, “FloTHERM ® PACK User ’ s Guide,” no. July. 2012.
- [21] “Scroll Compressor and Vacuum Pump Efficiency.” [Online]. Available:
<https://airsquared.com/scroll-technology/articles/scroll-compressor-and-scroll-vacuum-pump-efficiency-explained/>.
- [22] F. P. Incropera, D. P. Dewitt, T. L. Bergman, and A. S. Lavine, *Fundamentals Heat and Mass Transfer*, 6th ed. Hoboken: John Wiley & Sons, 2007.

Appendix A: Experimental setup and instrumentation for testing VCR system with custom evaporator.

To validate the predicted final evaporator performance and to determine the appropriateness of the correlations used during the design process, experimental data for the vapor compression refrigeration cycle was needed. In order to collect data on the evaporator, a fully-functioning, compact refrigeration system was needed. The Liquid Chiller Module (LCM), produced by Aspen Systems, was chosen for this project due to its compact size and commercial availability. Figure A.1 below shows an image of the LCM.



Figure A.1: Liquid Chiller Module produced by Aspen Systems.

Aspen's LCM was designed to provide a cooling capacity of 400 W and has outer dimensions of 19.8 cm. (7.8 in.) x 13.5 cm. (5.3 in.) x 16.0 cm. (6.3 in.) (W x H x L). The LCM has an advertised maximum ambient temperature of 50 °C which is slightly less than the 55 °C ambient desired for this project. For this project, the standard evaporator that comes with the Aspen LCM was going to be cut out and replaced with a prototype of the evaporator design discussed in this

paper. Since the LCM is only able to operate in a 50 °C ambient, only the condenser will be exposed to the 55 °C ambient maintained within a thermal chamber. The remaining components of the VCR system will be kept outside the thermal chamber. This should keep the condenser and condenser panel from overheating while allowing the condenser to reject heat to ambients over 50 °C. A 3D model of the Aspen LCM with the new evaporator integrated is shown below in Figure A.2.

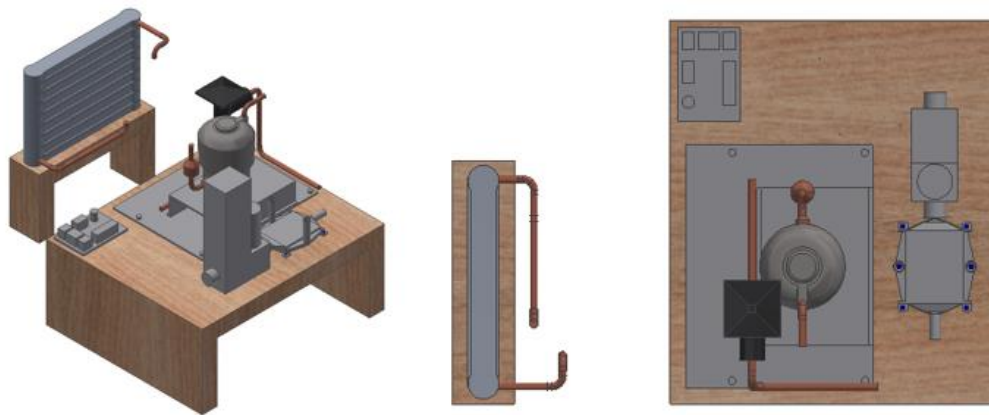


Figure A.2: Aspen LCM with new evaporator, flow meter, and wooden test fixtures.

Once the vapor compression refrigeration system had been set up with the condenser isolated in the thermal chamber, temperature and pressure data could be collected at the four necessary locations. These locations are between each of the four main components as shown in Figure A.3.

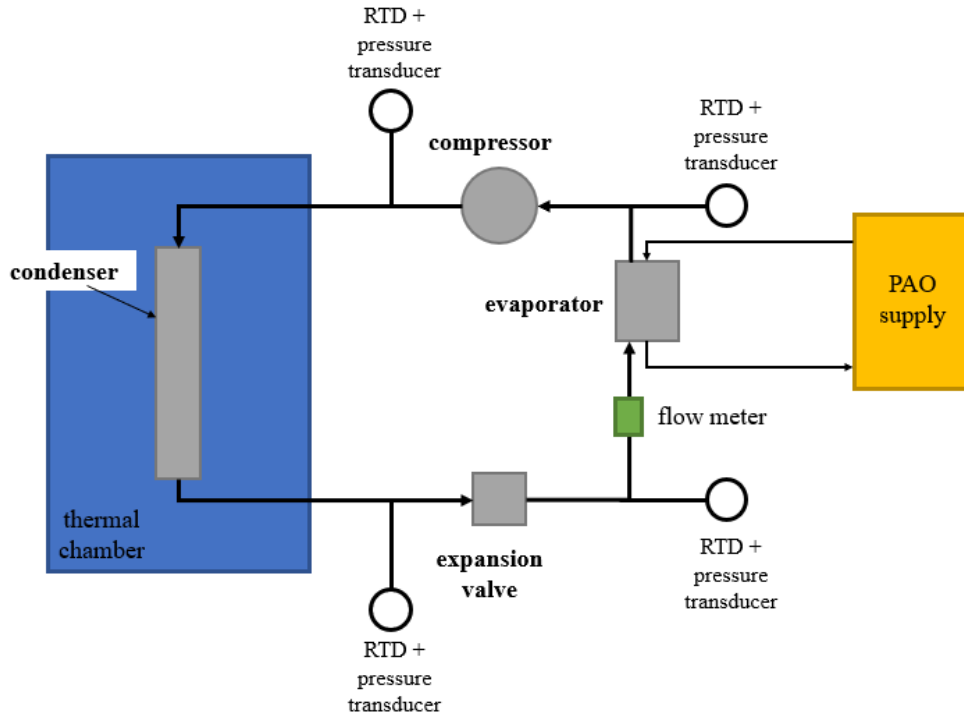


Figure A.3: Experimental schematic for the VCR system including instrumentation.

Figure A.4 shows RTDs and pressure transducers branching off the refrigeration lines. These sensors will collect the necessary data needed to construct the VCR cycle which can then be compared to the T-s and P-s diagrams generated during the design process. Measuring the mass flow rate through the evaporator, combined with the temperature and pressure data, will be used to determine cooling capacity. The RTDs will be inserted into the refrigeration lines using a T-junction with the RTD probe located in the corner, just extended past the junction and into the refrigerant flow as illustrated in Figure A.4.

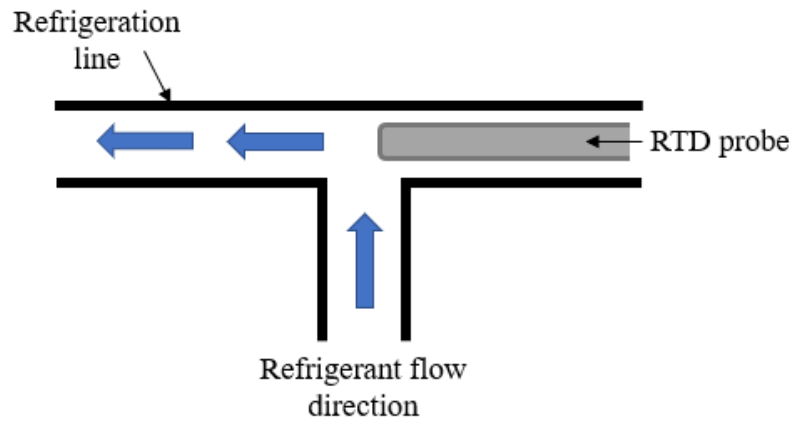


Figure A.4: RTD probe inserted into refrigeration line via T-junction.

Appendix B: Simulation setup procedure using ANSYS Fluent.

In ANSYS Workbench 19.2, a new Fluid Flow Fluent project was opened. To import the lanced offset fin model, which was created using a separate 3D model program, the Design Modeler program was opened and the “Import External Geometry File” located under the File tab used to load in the STEP file of the part. Once the part was loaded into Design Modeler, inlet, outlet, and periodic boundary condition surfaces were named by selecting the faces, right clicking, and selecting “New Named Selection.” The fin model and fluid region components of the STEP file were classified as a single part to ensure matching face meshes. See Figure B.1 below.

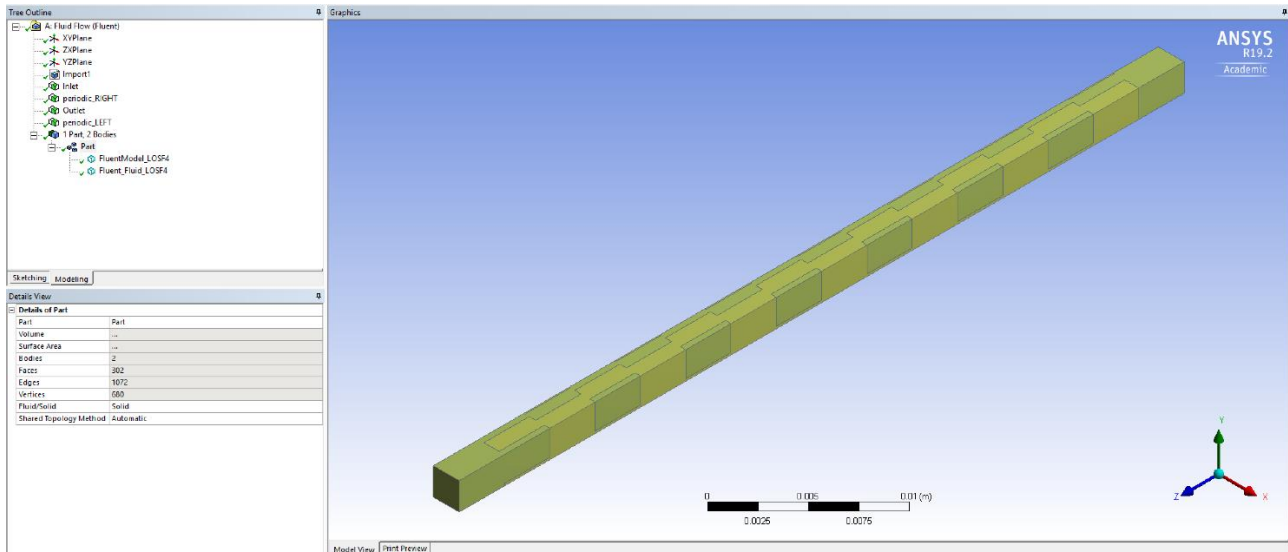


Figure B.1: Lanced offset strip fin model in Design Modeler with named surfaces.

Once the model was properly imported and labeled in Design Modeler, the Mesh interface was launched. A “Face Sizing” constraint was added to the fin-fluid interface to control

the element size at the junction of the two components. An “Inflation” constraint was also added to the fluid component of the model to better capture the boundary layer. Figures B.2, B.3, and B.4 show the “Face Sizing”, “Inflation”, and general mesh details respectively.

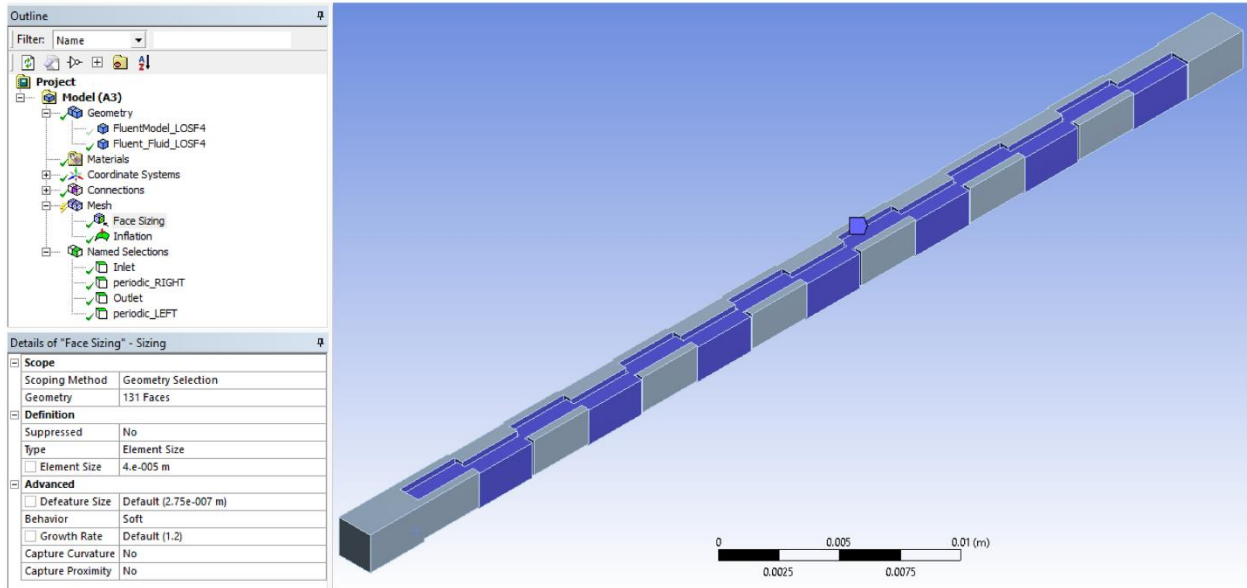


Figure B.2: Face Sizing mesh feature used on lanced offset strip fin model.

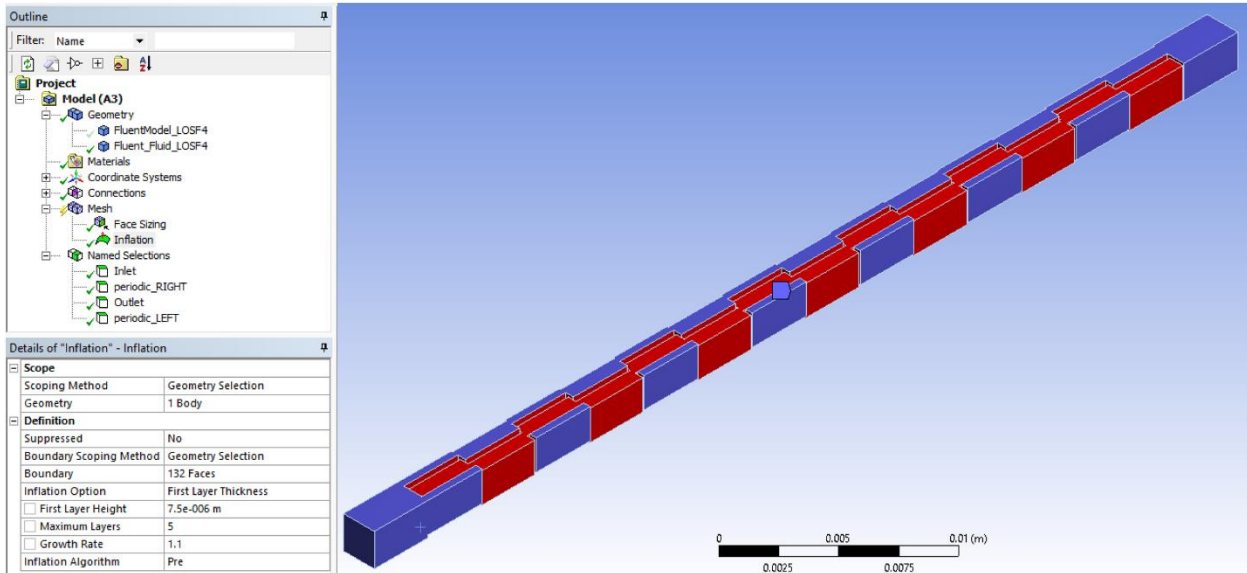


Figure B.3: Inflation mesh feature used on lanced offset strip fin model.

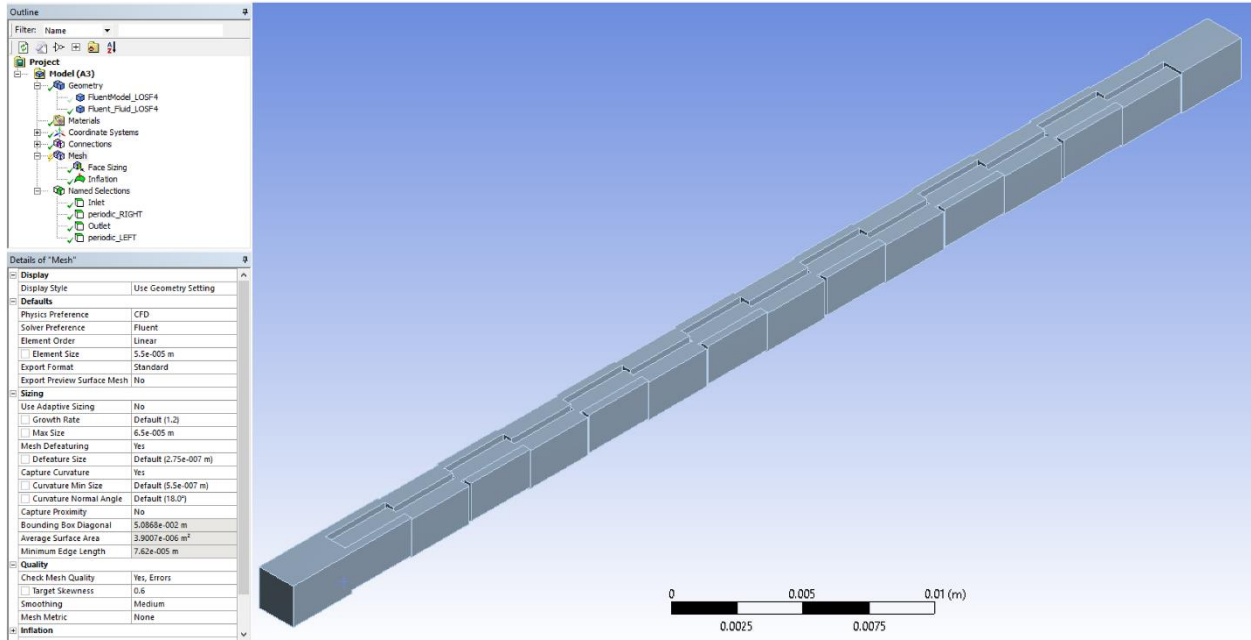


Figure B.4: General mesh details used on lanced offset strip fin model.

Once the mesh refinements had been applied to the model, the mesh was generated and loaded into the Fluent project. The final mesh can be seen in Figure B.5.

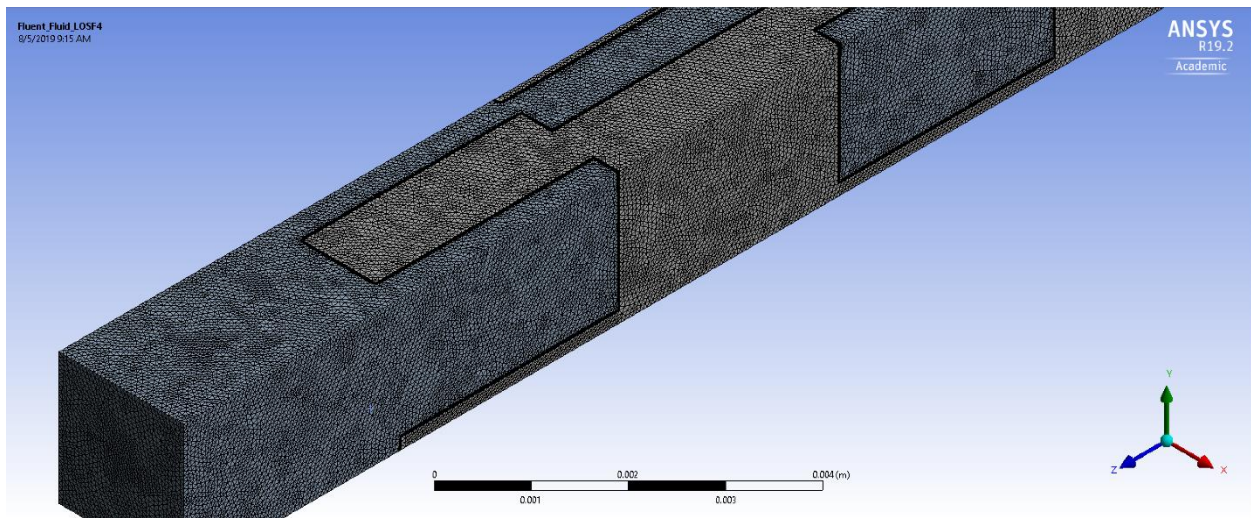


Figure B.5: Final mesh rendering with applied Face Sizing and Inflation mesh refinements.

With the geometry and meshing completed, the “Setup” portion of the Fluent project could be completed. Double precision was chosen when prompted at the initial opening of the

“Setup” interface. Using the Fluent program, properties for the PAO were manually created by opening the “Fluids” tab on the project tree as shown in Figure B.6 below.

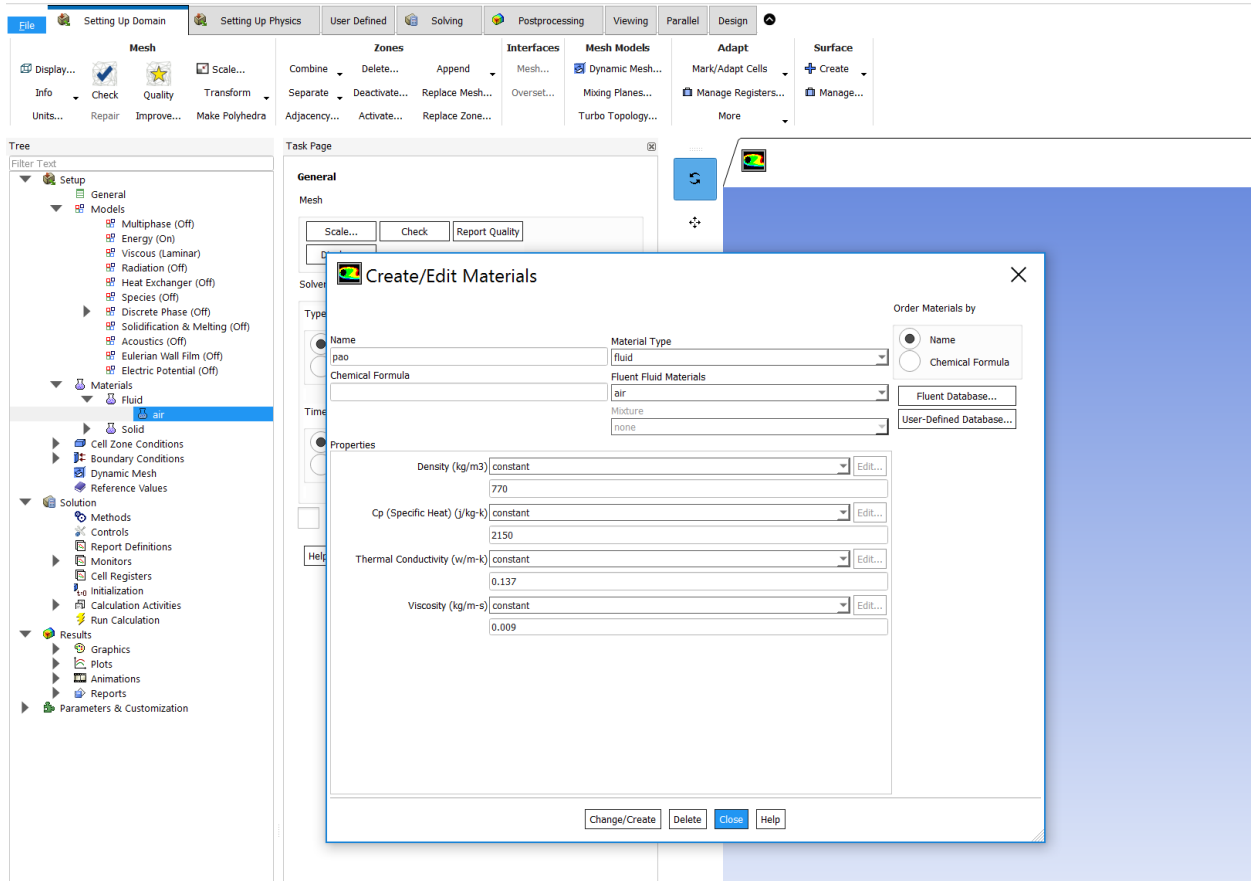


Figure B.6: Manually entering PAO fluid properties into Fluent.

After the fluid and solid materials were properly chosen, the boundary conditions were applied. Because of the geometry of the lanced offset strip fins, a periodic boundary condition had to be manually created. This was done by first changing the outside vertical faces of the model from their default “Wall” to “Interface.” Once these faces were changed to “Interface” they could be manually adjusted to a periodic boundary condition by using the “Interfaces” tab as shown in Figure B.7.

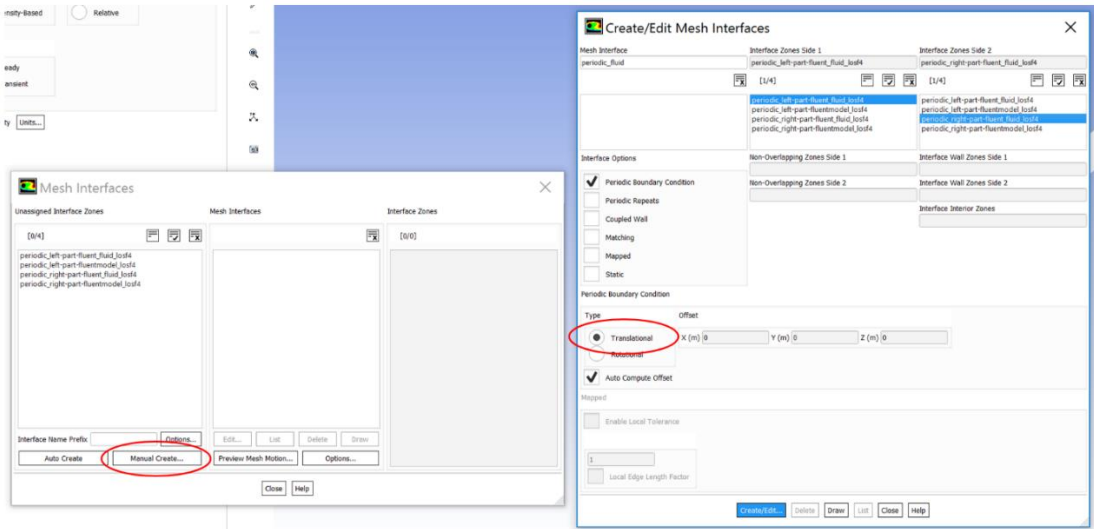


Figure B.7: Manually creating periodic boundary conditions for the lanced offset strip fin model.

After the periodic boundary conditions were enforced, the inlet velocity, inlet temperature, and isothermal boundary conditions on the top and bottom surfaces were applied by selecting the appropriate surface under the “Boundary Condition” tab of the project tree and entering in the appropriate values. An example of this is shown in Figure B.8 which captures the top and bottom temperature boundary condition being applied.

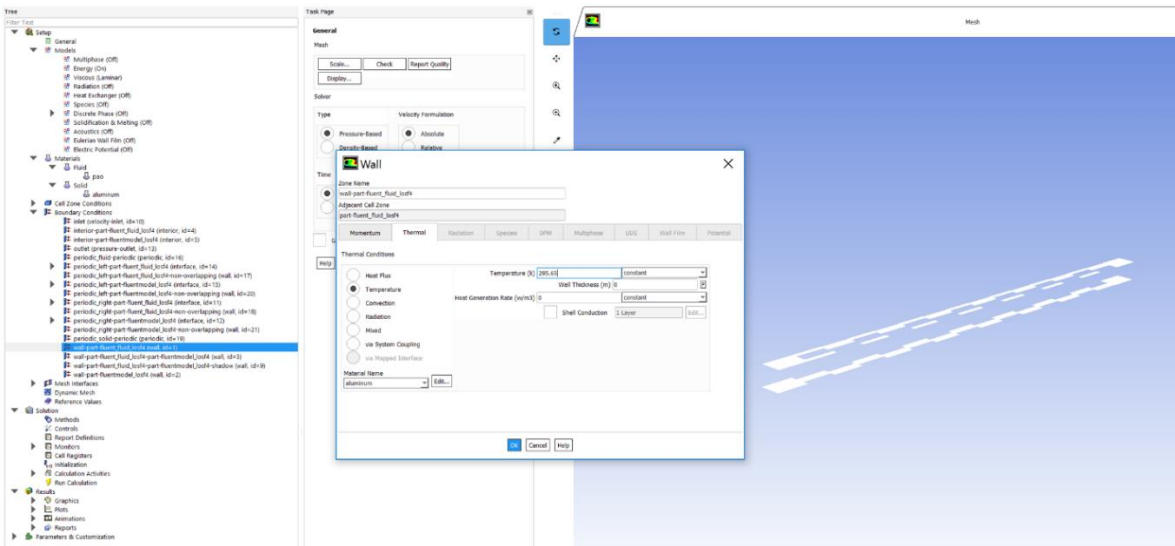


Figure B.8: Applying constant temperature boundary condition to top and bottom surfaces of the lanced offset strip fin model.

Energy transport models were turned on using the “Models” tab and a coupled solution chosen under the “Solution” tab of the project tree. The default hybrid initialization was used when solving the model with residuals monitored every iteration.